Interactions between near-surface turbulence and surface waves in the presence of sea ice

Luc Barast

COLLEGE DOCTORAL BRETAGNE SCIENCES DE LA MER ET DU LITTORAL

Université de Bretagne Occidentale

THÈSE DE DOCTORAT DE

L'UNIVERSITÉ DE BRETAGNE OCCIDENTALE

ÉCOLE DOCTORALE N° 598
Sciences de la Mer et du Littoral
Spécialité : *Océanographie physique et Environnement*

Par
Luc BARAST

Interactions entre turbulence et vagues à l'interface air-mer en présence de glace de mer

Thèse présentée et soutenue à Plouzané, le 06/04/2023
Unité de recherche : UMR 6523 - Laboratoire d'Océanographie Physique et Spatiale - LOPS - UBO

Rapporteurs avant soutenance :

Vincent REY	Professeur des Universités, MIO, Université de Toulon
Marie-Noëlle HOUSSAIS	Directrice de recherche CNRS, LOCEAN, Paris

Composition du Jury :

Président :	Vincent REY	Professeur des Universités, MIO, Université de Toulon
Examinateurs :	Marie-Noëlle HOUSSAIS	Directrice de recherche CNRS, LOCEAN, Paris
	France FLOC'H	Maître de conférence HDR, Géosciences Océan, Brest
	Michel BENOIT	Chercheur senior HDR, EDF, Chatou
Dir. de thèse :	Fabrice ARDHUIN	Directeur de recherche CNRS, LOPS, Brest

Invité(s) :

Co-enc. de thèse :	Peter SUTHERLAND	Chercheur IFREMER, LOPS, Brest
Co-enc. de thèse :	Dany DUMONT	Professeur ISMER, UQAR, Rimouski, Québec, Canada

Remerciements

Je tiens tout d'abord à exprimer ma gratitude envers Fabrice Ardhuin, mon directeur de thèse, pour m'avoir offert l'opportunité de réaliser cette recherche et pour son soutien constant tout au long de ce processus. Sa présence a grandement participé à mes avancées et son expertise m'a permis de progresser dans mes recherches.
Je remercie chaleureusement Peter Sutherland, mon encadrant principal de thèse, pour m'avoir proposé un sujet passionnant et pour son suivi régulier. Il m'a accordé une grande liberté, propice à mon développement personnel, tout en étant exigeant dans la qualité de mes travaux. Sa rigueur scientifique m'a poussé à donner le meilleur de moi-même, mais il a aussi su être compréhensif et me soutenir dans les moments difficiles ; je lui en suis reconnaissant.
Je souhaites aussi remercier Dany Dumont, qui a rejoint l'encadrement de ma thèse en cours de route. Ses précieux conseils et ses explications scientifiques, agrémentées d'anecdotes entre deux poussées de canot à glace pendant les missions BicWin, ont été très bénéfiques pour mon travail. Sa contribution a été un atout important pour l'avancement de ma recherche.

J'exprime ma gratitude envers Marie-Noëlle Houssais et Vincent Rey, pour l'honneur qu'iels m'ont fait de rapporter ma thèse, et pour avoir participé à mon jury de thèse aux côtés de France Floc'h et Michel Benoit, que je remercie aussi.

Je suis reconnaissant à Joël Sommeria et Frédéric Vivier d'avoir honoré leur rôle de comité de suivi individuel, et même au delà, au travers de discussions passionnantes et constructives. Je remercie aussi Cécile Bolley, Adélaïde Missault et Benoite Morin, coordinatrices scientifiques auprès de la DGA, pour leur suivi régulier au sein des réunions du comité de suivi individuel.

Aux LOPSiens, et en particulier aux membres de l'équipe SIAM, je souhaite exprimer ma reconnaissance, pour leur accueil, leur gentillesse et leurs conseils. En particulier, je remercie Fanny, ma marraine de thèse, qui m'a soutenu tout du long, et s'est démenée pour que je puisse avoir la chance de finir mon doctorat. Je pense aussi à Mickaël et Mathias pour leurs conseils en modélisation et leur bonne humeur sans faille, à Jean-Marc, pour ses questions pertinentes en séminaire, et pour ses conseils précieux en matière de poursuite professionnelle, et à Owen pour tous les échanges que nous avons eu sur l'essor de l'intelligence artificielle et son application dans nos travaux de recherche. Je tiens

aussi à remercier les membres de l'équipe administrative, Denise puis Valérie, pour leurs bienveillance et leur aide indispensable dans tous les déplacements que j'ai fait au cours de cette thèse. Enfin merci à tous les autres, que je n'ai pas cités, mais avec qui j'ai pu partager un café ou un repas, avec des discussions plus ou moins scientifiques en contemplant la rade de Brest.

Aux amis qui ont jalonné mon parcours étudiant et mon parcours de vie, un grand merci. Je pense notamment à ceux de Brest, Alex et Sophia, qui m'ont accueilli dès mon entrée au LOPS, Ivane et Léa, avec qui j'ai fait mes premiers pas au sein de l'Ifremer, Marie, qui a réalisé en même temps que moi le sprint final de fin de thèse, Gwendal, dont la bonne humeur est un baume à tous les maux, Emma, ma petite sœur de thèse, Léo et Manuel, pour les débats politiques passionnés et pour les instants musicaux partagés, Marine, pour son soutient indéfectible, Édouard, pour ses conseils cinématographiques, et enfin Hugo, pour l'incroyable mission sur glace que nous avons partagé. Je n'oublie pas non plus les amis de Picardie, Rafi, Léo, Nolan, Pinpon, Mousse, et tous les autres, avec qui j'ai vécu de grandes aventures de vie, et qui n'ont jamais cessé de me soutenir dans ce projet de thèse.

Je remercie infiniment ma mère, mes frères, ainsi que ma belle famille pour leur soutient inconditionnel, et pour tous ces moments où iels sont venu.e.s alléger mon quotidien pour que je puisse respecter mes échéances.

Mes derniers remerciements vont à ma femme, Aline, qui m'a soutenu pendant toutes ces années, qui a cru en moi et m'a poussé en avant même dans les pires moments de doute, et surtout, qui a partagé avec moi les plus belles des expériences, avec la naissance de Lou, puis celle de Eliott. À vous trois, je dédie cet ouvrage.

Cette thèse m'a donné une certitude :
la science réside dans les incertitudes.

Résumé en français

La glace de mer couvre l'océan dans les régions polaires sur des millions de kilomètres carrés. Elle est constituée de plaques de glace pouvant aller de quelques centimètres à quelques centaines de kilomètres de long, et de quelques millimètres à plusieurs mètres d'épaisseur. En raison des activités humaines, la température moyenne à la surface de la Terre augmente quatre fois plus vite dans la zone Arctique que sur le reste de la planète, ce qui entraîne une diminution considérable de l'étendue et de l'épaisseur de la glace de mer Arctique depuis plusieurs décennies.

La diminution de la couverture de glace de mer affecte la dynamique de l'atmosphère et de l'océan, modifiant le contenu en eau douce et en chaleur de l'océan. Elle implique également une augmentation de la surface de l'océan non couverte par la glace, ce qui se traduit par une plus grande zone propice à la croissance des vagues. Des conditions de vagues plus fortes et plus fréquentes dans les régions polaires ajoutent des mécanismes de rétroaction complexes aux interactions atmosphère-glace-océan. Il est donc crucial de comprendre ces interactions pour améliorer notre modélisation du climat terrestre en évolution et se préparer à l'avenir des activités humaines en Arctique.

À la frontière entre la banquise et l'océan libre de glace se trouve la zone marginale de glace (MIZ pour Marginal Ice Zone en anglais). Son étendue est définie selon divers critères tels que la concentration en glace, les contraintes éoliennes et de vagues à l'interface air-mer, ou la distribution de taille des plaques de glace. Les vagues y sont atténuées par la couverture de glace, leur énergie décroissant de manière exponentielle au fur et à mesure qu'elles se propagent sous la glace. Ceci peut être dû à divers phénomènes tels que la réflection des vagues sur la glace (scattering), la dissipation turbulente dans la colonne d'eau, les processus mécaniques internes à la banquise et les interactions entre les plaques de glace. Alors que le premier est un phénomène conservateur, tous les autres processus physiques sont dissipatifs, entraînant un transfert d'énergie entre le champ de vagues et soit l'océan, soit la banquise. Comprendre ces interactions entre les vagues et la glace est au cœur de l'étude de la MIZ.

La réflection des vagues sur la glace a lieu quand les vagues sont plus courtes que la taille des plaques de glace, et est caractérisée par un étalement du spectre directionnel des vagues quand on pénètre plus avant dans la glace de mer. Récemment, probablement dû à des conditions de glace différentes, elle a été peu observée sur le terrain, tandis que la mesure d'un étalement directionnel qui rétréci suggère que les processus dissipatifs jouent un rôle important.

Parmi ces processus, la dissipation d'énergie des vagues dans la glace intervient sous la

forme de compression, flexion et cassure de la glace. La modélisation de ces phénomènes avec WAVEWATCH III donne des résultats très dépendants des conditions de glace, et montre qu'ils sont insuffisant à expliquer toute l'atténuation des vagues.

Les interactions entre plaques de glace regroupe les collisions et frictions entre plaques de glace, et la compaction de multiples plaques de glace. Ces interactions ont été étudiées pour discuter de la dynamique des plaques de glace, mais leur impact sur l'atténuation des vagues n'a pas été quantifié dans des conditions de vagues et de glace réalistes.

La turbulence générée lorsque les vagues rencontre la glace peut prendre la forme de friction sous (skin friction) et autour (form drag) des plaques de glace, de déferlement sur la glace (overwash), ou encore de jet turbulent généré par la convergence et la divergence entre deux plaques de glace. Jusqu'à présent, elle a été essentiellement modélisée en faisant l'hypothèse que toute la turbulence due aux vagues sous la glace pouvait être expliquée par les phénomènes de friction. Ces modèles font aussi souvent l'hypothèse que toute l'atténuation des vagues est due à la friction turbulente des vagues sur la glace, ce que tendent à supporter de récentes mesures, dans des conditions de faible concentration en jeune glace. Cependant, en l'absence de plus de validations expérimentales, l'utilisation de tels modèles quelques soient les conditions de glace et de vagues risque d'occulter d'autres physiques d'atténuation des vagues dans la glace en jeu, que ce soit d'autres sources de turbulence ou d'autres interactions vague-glace.

L'enjeu de cette thèse est d'étudier les interactions vagues-glace à partir de multiples mesures de terrain, afin de quantifier le rôle de la turbulence dans l'atténuation des vagues, d'étudier les sources de turbulence dues à des interactions vague-glace, ainsi que d'évaluer les autres sources d'atténuation.

Les expérimentations, en partie menées pendant cette thèse, font partie du programme d'observation BicWin, et ont lieues dans des laboratoires naturels de l'estuaire du bas Saint Laurent, au Canada. Ces zones d'études, nommées Baie du Ha ! Ha ! et Baie de Rimouski, sont des baies peu profondes, dans lesquelles une couverture de glace peut se former en hiver, soit par advection par les courants de plaques de glace formées en dehors des baies, soit par croissance thermique de banquise côtière. La présence d'une polynie de chaleur sensible à cet endroit du fleuve permet la croissance de vagues, lors de tempêtes, pouvant se propager dans les baies. Cette configuration est propice à la formation de MIZs, et à l'étude des interactions vague-glace.

Les expériences de terrain du programme BicWin sont basées sur des expéditions journalières, durant lesquelles tout le matériel de mesure est déployé puis récupéré après une durée d'acquisition variable. Les déploiements s'effectuent à partir d'un canot à glace, dans lequel est placé tout le matériel, ainsi que l'équipe scientifique, qui fait aussi office de force de propulsion. Les mesures sont faites principalement dans la partie houleuse de la MIZ, à partir de bouées, pour mesurer les vagues et les déplacements des plaques de glace,

de courantomètres acoustiques à effet Doppler (ADCPs) pour mesurer la turbulence et les courants, de drones pour prendre des photos, et d'une règle pour mesurer l'épaisseur des plaques de glace.

Neuf jeux de données sont obtenus entre 2017 et 2020, avec à la fois des mesures de turbulence et de vague, dont 6 dans ou à proximité de la Baie du Ha ! Ha !, et 3 dans la Baie de Rimouski. Dans la plupart des cas, la couverture de glace consiste en de la glace côtière le long de la côte, et, au large, en une MIZ contenant des plaques de glace d'une taille allant de moins d'un mètre à quelque dizaines de mètres. Un mélange de glace pillée (brash ice), de cristaux de glace (frazil/slush) et d'eau est généralement observé à la surface de la mer, dans les interstices entre les plaques de glace. Les conditions de vagues incidente vont de quelques dizaines de centimètres de hauteur à un peu moins de deux mètres.

Les missions de terrain BicWin utilisent des bouées de glace pour mesure de cinématique de surface (SKIBs) et des bouées Sofar Spotter pour mesurer le mouvement des plaques de glace et des vagues, les SKIBs mesurant l'accélération et le moment angulaire à l'aide de capteurs IMU et les bouées Spotter mesurant le déplacement de la surface de la mer à l'aide de capteurs GPS.

Les données de vagues sont découpées en intervalles de 10 minutes, suffisamment longs pour permettre une bonne représentation statistique des vagues, et assez courts pour éviter de prendre en compte des changements significatifs de la dynamique océanique, comme la marée. La densité spectral omnidirectionnelle d'énergie des vagues est calculée par l'intermédiaire de transformées de Fourier fenêtrées (méthode de Welch).

Ensuite, en intégrant ce spectre d'énergie par rapport à la fréquence, l'énergie du champ de vagues est obtenue en fonction de la distance au bord de glace. Cette distance correspond au chemin parcouru par les vagues depuis le bord de glace, qui est la limite nette entre l'océan libre de glace et le début de la MIZ, jusqu'à l'instrument de mesure considéré. La décroissance exponentielle de l'énergie en fonction de la distance au bord de glace est observée, avec des coefficients d'atténuation allant de 10^{-2} à 10^{-1} m^{-1}.

Enfin, la quantité considérée dans ce travail pour comparer l'atténuation de l'énergie des vagues à la dissipation de l'énergie des vagues due aux interactions vague-glace est le taux total d'atténuation/dissipation de l'énergie par unité de surface de mer. A partir des mesures de vagues, ce taux est calculé comme le flux résiduel d'énergie des vagues à travers un volume de contrôle, qui est délimité par deux bouées successives et aligné avec la direction des vagues. Après avoir vérifié que l'impact du frottement des vagues sur le fond de l'océan était négligeable, des valeurs entre 10^{-4} et 10 $\mathrm{W.m}^{-2}$ sont obtenues.

La vitesse de l'écoulement dans la colonne d'eau sous la glace est mesurée à partir d'ADCPs, utilisant l'effet Doppler pour les mesures de courant (horizontalement par

rapport à la surface), et la cohérence d'impulsion pour les mesures de turbulence (verticalement par rapport à la surface). Cette deuxième méthode consiste à mesurer le déphasage entre deux impulsions successives initialement en phase, après qu'elles aient été réfléchies par une particule en suspension dans l'eau ayant une vitesse non nulle dans la direction de propagation des impulsions. Elle a l'avantage de permettre une meilleure résolution des vitesses, utile pour mesurer la turbulence plus finement, au détriment de l'amplitude maximum mesurable, qui est elle limitée à cause du principe de mesure par déphasage, qui génère un bouclage (wrapping) des vitesses au delà de ce maximum.

La qualité des données est contrôlée, en retirant les points pour lesquels l'énergie du signal réfléchi est inférieure à 30 coups sur 150, ou pour lesquels la mesure de corrélation est inférieure à 50 %, et en débouclant les vitesses turbulente mesurées. Puis la méthode des fonction de structure d'ordre 2 est appliquée sur les fluctuations de vitesse turbulentes pour calculer le taux de dissipation d'énergie cinétique turbulente. Deux variantes de cette méthode sont testées, la première retirant l'effet du bruit Doppler de l'instrument (Wiles et al., 2006), et la seconde retirant en plus la contribution des vagues (Scannell et al., 2017). Les profils de turbulence obtenus s'étendent au maximum dans les 2 premiers mètres sous la glace, avec en générale soit une décroissance en loi de paroi, soit une valeur à peu près constante en fonction de la distance en dessous de la glace.

Le taux total de dissipation de l'énergie cinétique turbulente par unité de surface de mer est calculé à partir de ces profils. Une discussion est ensuite menée pour séparer la turbulence due aux interactions vague-glace de la turbulence générée par la friction du courant sur la glace et sur le fond des baies. La friction du courant est modélisée par analogie avec la littérature sur la couche limite du fond marin, en utilisant des coefficients de frottement adaptés, et les vitesses de courant mesurées par les ADCPs ou des mesures de référence antérieures selon les cas. Il est observé que pour certains déploiements, l'ensemble de la turbulence mesurée est possiblement due uniquement à la friction des courants, signifiant que dans ces conditions, les interactions vague-glace ne produisent pas de turbulence. Une fois l'effet des courant pris en compte, le taux total de dissipation de l'énergie cinétique turbulente par unité de surface de mer due aux interactions vague glace couvre des valeurs entre 0 et 10^{-2} W.m^{-2}. Il apparaît que la turbulence due aux interactions vague-glace n'est responsable au mieux que de 10 % de l'atténuation des vagues dans les conditions observées, mettant en question l'utilisation de modèles d'atténuation des vagues ne considérant que la turbulence générée par les interactions vague-glace. Les sources de turbulence due au interactions vague-glace sont discutées, avec en particulier le calcul de coefficients de frottement dans l'hypothèse où la turbulence serait due au frottement des vagues sur la glace. La piste de production de turbulence par jet induits par la convergence entre deux plaques a été étudiée en se basant sur le modèle théorique du jet plan turbulent, mais les niveaux de turbulence modélisés ne coïncident pas avec les mesures.

La question se pose donc de savoir quels sont les mécanismes à l'origine de l'essentiel de l'atténuation des vagues dans les cas rencontrés. Étant donné la forte proximité des plaques de glace dans la zone houleuse des MIZs étudiées, ainsi que leur longueur, généralement bien plus petite que la longueur d'onde des vagues (excluant la réflection des vagues sur la glace et la flexion des plaques), la piste des interactions entre plaques de glace a été étudiée.

En particulier, lors des déploiements, des collisions entre plaques étaient souvent observées. Pour quantifier l'énergie des vagues dissipée par des collisions, la différence d'énergie cinétique de plaques de glace entre avant et après chaque collision a été calculée, à partir des données d'accélération de bouées SKIB placées sur ces plaques. Le taux de dissipation d'énergie par unité de surface de mer dû aux collisions est calculé pour chaque cas présentant des collisions, donnant des valeurs entre 10^{-5} et 1 W.m^{-2}, expliquant entre 1 et 100 % de l'atténuation des vagues.

La théorie des matériaux granulaires de Mohr-Coulomb a été utilisée pour estimer l'énergie dissipée lors de la compaction par les vagues de la couche de glace, quand celle-ci est constituée de multiples plaques de glace se chevauchant. Le taux de dissipation d'énergie totale par unité de surface de mer causée par la compaction des plaques a été calculé en fonction de la contrainte de rupture horizontale de l'amas de plaques de glace, de l'épaisseur de la glace mesurée et des paramètres des vagues obtenus grâce aux mesures des bouée vagues. Des valeurs comprises entre 10^{-2} et 1 W.m^{-2} ont été obtenues et expliquent entre 1 et 100 % de l'atténuation des vagues.

Ces deux résultats ont montré que, dans le cas d'une MIZ très concentrée en plaques de glace, de longueur petites par rapport à la longueur d'onde des vagues, la principale source d'atténuation des vagues provient des interactions entre plaques de glace. Ensemble, les collisions entre plaques et la compaction des plaques ont permis d'expliquer au moins 40 % de l'atténuation de l'énergie des vagues pour 8 déploiement sur 9, et même 100 % de l'atténuation pour 5 de ces déploiements. Cependant, l'atténuation de l'énergie des vagues n'a pas toujours pu entièrement être expliquée à partir des mesures de ce travail, et des pistes sont suggérées pour mesurer et analyser d'autres interactions vague-glace comme le cisaillement entre plaques non attribuable à de la compaction, la dissipation visqueuse dans le mélange d'eau et de cristaux de glace, et l'érosion des plaques de glace due aux collisions.

TABLE OF CONTENT

Acronyms

ADCP Acoustic Doppler Current Profiler.

AWAC Acoustic Wave And Current profiler.

BdHH Baie du Ha! Ha!.

BicWin Bic Winter.

FSD Floe Size Distribution.

HR High Resolution.

ISMER Institut des sciences de la mer à Rimouski.

LOPS Laboratoire d'Océanographie Physique et Spatiale.

LSLE Lower St. Lawrence Estuary.

MC Mohr-Coulomb.

MIZ Marginal Ice Zone.

MIZEX Marginal Ice Zone Experiment.

PCADP Pulse Coherent Acoustic Doppler Profiler.

PIV Particle Image Velocimetry.

PSD Power Spectral Density.

RB Rimouski Bay.

RMS Root Mean Square.

S1000 Signature 1000.

SKIB Surface Kinematic Ice Buoy.

SWIFT Surface Wave Instrument Float with Tracking.

TKE Turbulent Kinetic Energy.

UAV Unmanned Aerial Vehicle.

UTC Coordinated Universal Time.

UTM Universal Transversal Mercator.

WAVEWATCH III WAVE-height, WATer depth and Current Hindcasting III.

WMO World Meteorological Organization.

Chapter 1

Introduction

1.1 Recent changes in the northern cryosphere

Sea ice forms at the ocean surface when seawater reaches a temperature near -2 °C, mostly depending on salinity (Jackett et al., 2006). Due to a lower density than the one of liquid sea water, sea ice floats on the ocean. In polar regions, the total area covered by sea ice reaches millions of square kilometres. This ice layer is not homogeneous: it is made up of numerous ice plates called "ice floes" with sizes varying from a few centimeters up to hundreds of kilometers, and thickness ranging from a few millimeters to several meters. The sea ice extent is the area of the ocean covered by sea ice. In the Arctic, for passive microwave remote sensing data, it is the area of the ocean with ice concentration over 15 %. It varies considerably throughout the year (see Fig. 1.1.b). For instance, in September, the sea ice extent in the Arctic Ocean reaches a minimum after summer has warmed up the northern hemisphere (see Fig. 1.1.a), whereas at the end of winter, in March, the sea ice covers most of the Arctic ocean, constrained by the surrounding continents and the warmer waters of the Atlantic and Pacific oceans.

The presence of an ice cover over the ocean has multiple impacts:

— Air-sea exchanges (heat, momentum, mass) are strongly reduced or even prevented.

— Electromagnetic radiations are reflected (albedo) much more from the ice than from the sea water ($> 70\%$ vs $< 10\%$), affecting the ocean heat content and the proliferation of the biomass under the ice.

— The formation and melting of sea ice affect the stratification of the upper ocean respectively through brine and fresh water injection.

Our planet is now facing an important rise of average surface temperatures, largely due to human activities. This rise in average temperature is four times faster in the Arctic than on the rest of the planet (Rantanen et al., 2022). As a consequence, the extent and thickness of Arctic sea ice has decreased considerably in recent decades (Stroeve and Notz, 2018; Maksym, 2019), with an average extent reduction of about 3 million square kilometers at the summer ice minimum between 1992 and 2021 (see Fig. 1.1), and a shift from multiyear ice to much younger and thinner seasonal ice. The rapid pace of the decline of the Arctic ice cover in summer suggests an Arctic without sea ice at this time of the year by the middle of this century (Overland and Wang, 2013).

This increased melting of the ice cover affects atmosphere and ocean dynamics. The ocean fresh water and heat content are changing: the Atlantic-Arctic front is shifting northwards (Barton et al., 2018), limiting the growth of winter sea ice in some areas, and there are uncertainties about the long-term evolution (weakening or strengthening) of deep water formation and the Atlantic Meridional Overturning Circulation (Sévellec et al., 2017; Lique et al., 2018; Jackson et al., 2022). The change in albedo due to less ice cover results in less thermal reflection, which lead to more solar energy absorbed by the ocean, and then to more ice melting. This positive feedback climate process is called the "ice-albedo feedback". Less ice covering the ocean also lead to an increase in the atmosphere-ocean heat transfer (Stroeve et al., 2012).

Finally, this decrease in sea ice coverage implies an increase in the open water area and, consequently, more fetch (sea surface over which the wind blows) available for wave growth (Thomson et al., 2018). Stronger and more frequent wave conditions in polar regions add complicated feedback mechanisms to the atmosphere-ice-ocean interactions. Increased wave-induced upper-ocean mixing (Stoney et al., 2018) can lead to local and temporal changes in the upper-ocean heat content during storm events (Davis et al., 2016), with as a consequence increased ice melting rates, and/or increased surface cooling (Smith et al., 2018). Wave propagation is modified in presence of ice, and ice cover dynamics are impacted by the waves. Wave-ice interactions in the Arctic Ocean are becoming much more important than they used to be, progressively shifting towards what can be observed in the southern cryosphere. Therefore, it is key to understand them to improve our modeling of the changing Earth climate and to prepare the future of human activities in the Arctic.

1.2 Wave-ice interactions

In the open ocean, gravity waves are generated by the wind stress over the sea surface (Hasselmann et al., 1973), they propagate thanks to gravity which acts as a restoring force opposing surface elevation gradient, and their energy is dissipated mainly due to wave breaking (Komen et al., 1994). In high latitude seas and oceans, wave propagation is impacted by the presence of the ice cover (Robin, 1963a; Wadhams, 1973). Instead of facing gravity alone, waves also encounter the resistance of the ice to flexure (Liu and Mollo-Christensen, 1988), and in turn sea ice flexion due to waves causes the fragmentation into multiple ice floes depending on the waves dynamics (Dumont et al., 2011). Wave mixing can enhance ice production through thickening of the frazil ice (soup of ice crystals) and then formation of pancake ice (Wadhams et al., 1987; Doble et al., 2003; Roach et al., 2018). Under the wave radiation stress, which is the flow of momentum due to surface waves pushing forwards (Longuet-Higgins and Stewart, 1964), the ice pancakes or older floes made from fractured ice are compressed against the ice pack, and form a thicker and rougher ice cover than the one that would be obtained in case of only thermal growth

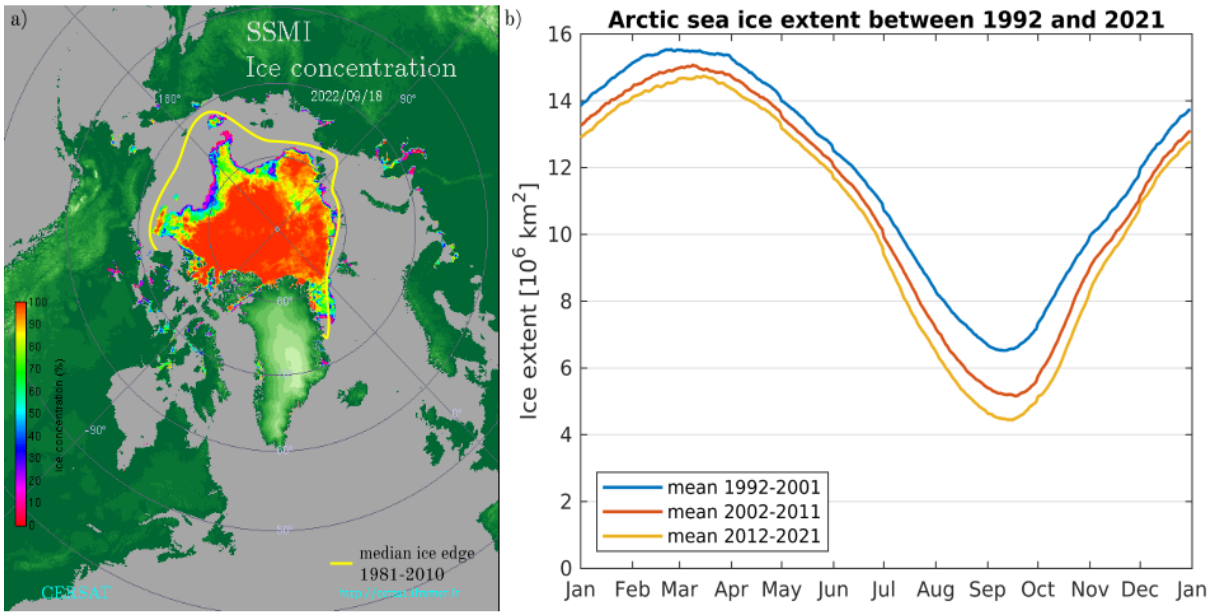

Figure 1.1 – a) Arctic sea ice extent at its annual minimum on 18 September 2022. The colormap represents sea ice concentration, and the thick yellow line the location of the edge of the ice cover (ice concentration just below 15 %) averaged between 1981 and 2010. Data from CERSAT/IFREMER. b) Year-round average Arctic sea ice extent in millions of m^2 for the periods 1992-2001, 2002-2011 and 2012-2021. Data from NSIDC.

(Stopa et al., 2018; Sutherland and Dumont, 2018).

The area at the border between the ice pack and the open sea, where the ice interacts the most with ocean waves, or where the ice has been affected by the waves, is called the Marginal Ice Zone (MIZ). Several definitions attempt to set the limits of the MIZ. Strong (2012) proposes a definition where the MIZ is enclosed between the sparse ice zone (ice concentration from 0 to 15 %) and the pack ice (ice concentration from 80 to 100 %). Sutherland and Dumont (2018) have proposed linking the extent of the MIZ to the relative importance of wind and wave stresses. More recently, Dumont (2022) discussed three large scale definitions: either the area where the mesoscale vortical dynamics of the ice floes are notable, given an undetermined threshold, or the part of the ice cover where waves are still dynamically significant (e.g. measurable from Synthetic Aperture Radar imagery), or the portion of the ice cover where the ice floes have a size below a maximum value (close to 200-500 m). All of these definitions result in MIZs ranging from several kilometres to several hundred kilometers in the Arctic. As more energetic waves develop in many areas due to the increase in open ocean fetch, this extent has increased in recent decades, especially in summer (Strong and Rigor, 2013), making it all the more important to understand the interactions between waves and ice in these areas.

Waves are attenuated by the ice cover with wave energy generally decreasing according

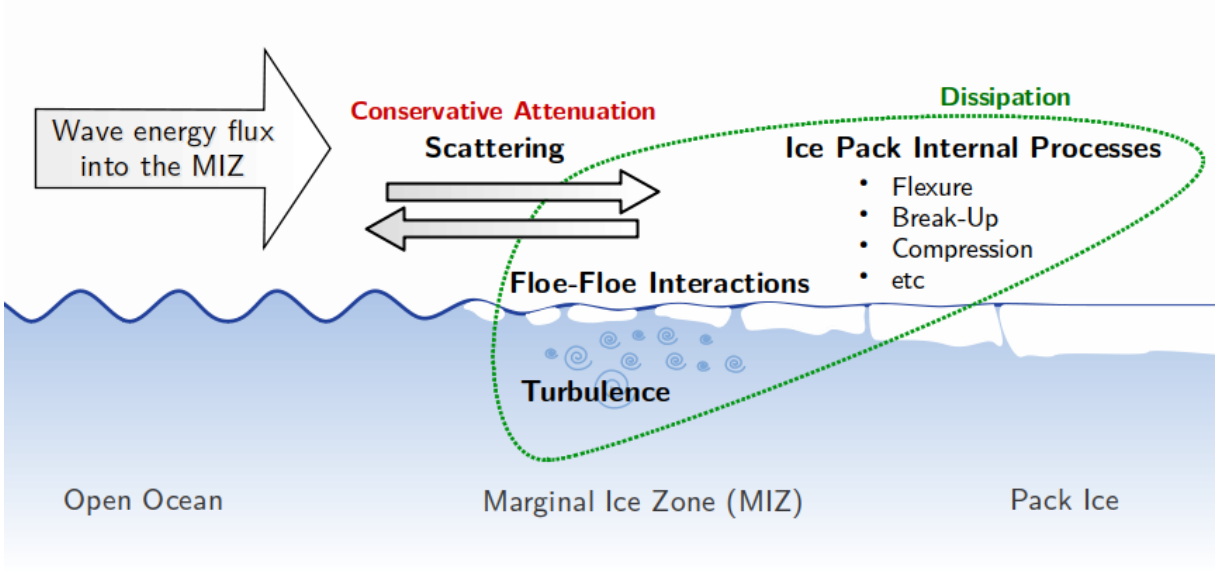

Figure 1.2 – Scheme of the wave-ice interactions in the MIZ.

to an exponential decay law of equation (e.g. Wadhams et al., 1986):

$$E(x_{\text{ice}}) = E_0 \exp(-\alpha x_{\text{ice}}), \tag{1.1}$$

where E_0 is the incoming wave field energy from the open ocean, x_{ice} is called the ice fetch (Sutherland et al., 2018) and is the distance into the ice cover from the ice edge (the boundary between open and covered ocean) to the ice pack following the path of wave propagation, and α is called the attenuation coefficient of the wave energy (in m^{-1}). From field observations, α is known to increase as a function of frequency (Squire et al., 1995). Some measurements in the literature have shown a reduction of α at high frequencies, but those have been largely shown to be the result of measurement errors (Thomson et al., 2021), or short wave generation in leads.

This attenuation can be due to several phenomena, as illustrated in Fig. 1.2:

— scattering, which is wave reflection off ice floes,
— viscous and turbulent dissipation in the water column under the ice,
— ice pack internal processes (e.g. flexure, compression, break-up), and
— interactions between floes (e.g. friction, collisions).

While scattering is a conservative phenomenon, all of the other physical processes are dissipative, meaning that there is an energy transfer between the wave field and either the ocean or the ice field. In the next paragraphs, a description will be given of the different processes as observed from field, as well as of the main modelling efforts.

1.2.1 Wave scattering

Wave scattering is the reflection of the wave field off the ice cover. It has been observed to occur when the floe size is of similar order to, or larger than, the wavelength, and is characterised by an increased directional spreading of the wave field as it propagates farther into the ice cover, towards isotropy (Wadhams et al., 1986), and by a reflection of part of the wave energy. Scattering was first computed during the analysis of the early field missions of Wadhams et al. (1986, 1988), called the Marginal Ice Zone Experiment (MIZEX), as a simple one-dimensional scattering model where the reflection coefficients are derived from the equations for solitary plates. This first model allowed to explain wave energy reflection for most waves, but did not result in an increase in the directional spreading, and was missing part of the energy from side reflections, inducing non-coherent addition of energy. In the following decades, this model evolved, first by being reevaluated in a multiple floe model as described in Squire et al. (1995) to cope with reflection between adjacent floes. Meylan and Squire (1996) added a 2-dimensionality to the model using the continuity of water velocity potential at the interface between the floes, inspired from the reflection of waves on other physical object than ice floes, as for example offshore facilities. Then, based on the previous literature, Kohout and Meylan (2008) proposed a model for thin elastic ice plates, accounting for the increase of the directional spreading of wave energy, and allowing to express wave attenuation as a function of the reflection parameters, such as floe size and ice concentration. An important progress in this model is the computation of dimensionless wave attenuation coefficients, directly usable in wave-in-ice modeling framework as in the work of Dumont et al. (2011), and later in the WAVE-height, WATer depth and Current Hindcasting III (WAVEWATCH III) modeling framework (The WAVEWATCH III® Development Group (WW3DG), 2019). However, since the era of MIZEX, scattering has been scarcely observed in the field, and cases without evidence of scattering have become numerous. For instance, several field experiments in different wave and ice conditions (Sutherland and Rabault, 2016; Sutherland and Dumont, 2018; Sutherland et al., 2018) observed a narrowing of the directional spreading with increasing ice fetch, while some other found a phenomenology (wave number energy attenuation dependence, significant wave height prediction with time) that was equally or better described using dissipation mechanisms (Sutherland and Gascard, 2016; Ardhuin et al., 2016; Voermans et al., 2019). The discrepancy is probably due to differences in the ice conditions. This is most probably related to too few field experiments to have comparable samples, or could be linked to the recent change in wave-ice conditions at the border of the Arctic ice pack, with stronger waves now encountering weaker and smaller ice Squire (2019).

1.2.2 In-ice processes

When ocean waves are reflected off or attenuated by the ice cover, the wave radiation stress (Longuet-Higgins and Stewart, 1964) induces a horizontal compressive force on the ice layer in addition to winds and current stresses (Robin, 1963b). Under compression, small floes tend to stack horizontally, increasing the ice concentration, and vertically (which is called ice rafting), increasing the ice layer thickness (Sutherland and Dumont, 2018). The vertical displacement of the ice induced by the wave orbital motion increases even more the rafting dynamics. Within the ice pack, i.e. outside of the MIZ, this compression can lead to vertical sea ice deformation called ridging.

In addition to compression, the heave motion of large floes induced by the wave orbital motion leads to ice bending, and even break-up when the strain applied is sufficiently high (Squire et al., 1995). These processes occurring within the ice layer affect in turn the amplitude of the waves, since part of wave energy is lost in the ice layer as heat. Few field experiments have addressed this topic in the literature, since measuring the mechanical response of the ice to the waves in the field is particularly complicated. In the recent modelling work of Boutin et al. (2018), they refer to the lab experiments of Cole (1998) based on subjecting sea ice samples to cyclic stresses to measure the viscoelastic properties of sea ice. The experiments allowed to verify the theory of the deformation of the sea ice under the strain applied by the waves, which can be decomposed into elastic, anelastic (both reversible but on different time scales) and inelastic (irreversible) response. From this observation and other modeling work by Wadhams and Cole, Boutin et al. (2018) derived wave attenuation coefficients that depend on ice properties, and tested them in WAVEWATCH III to simulate a realistic ice break-up event. They found that wave attenuation in this case strongly depends on the state of the ice cover (unbroken or broken), and could not be fully described by in ice processes, meaning that other wave ice interactions (scattering and ice bottom friction) had to be accounted for.

1.2.3 Floe-floe interactions

Besides in ice processes, interactions between ice floes have been observed during multiple field missions (see review of Squire et al., 1995), using accelerometers and tiltmeters to measure the motion of the floes. They consist mainly in collisions and friction (shear) between individual ice floes, to which can be added floe compaction (Sutherland and Dumont, 2018). These interactions result in translational or rotational momentum transfer, and therefore to dissipation of kinetic energy. In addition, during collisions and shear, small pieces of ice are often ejected from the floes, forming a heterogeneous layer of fragmented ice between the floes called "brash", or "slush" (when the brash is ground into a soup) that acts as an intermediary in the transfer of momentum between floes. These phenomena have been studied mostly to understand and model the dynamics of the ice

cover, and hardly to understand how they may take part to the attenuation of the wave field. Nevertheless, it is worth mentioning two experimental works. The first one is the laboratory experiment of Herman et al. (2019) involving a field of colliding ice floes in an ice tank coupled to a wave maker. In their experiment, they analyse the wave energy attenuation in terms of scattering, ice-water drag and overwash, and conclude that the wave attenuation has frequency dependence typical of dissipative phenomena. Furthermore, they admit that part of the dissipation can not be explained by their analysis, but could be due to other unmeasured dissipative phenomena, among which floe collisions. The second experiment was made by Løken et al. (2022) in a fjord where a pool and a full size ice floe were cut into landfast ice. In this study, they estimated the energy dissipation induced by the controlled periodic collision of the floe on the walls of the pool. After using accelerometers to compute the kinetic energy transferred to the landfast ice, they estimate that 7.5 % of the input energy could be dissipated by collisions of the floe. This result should be mitigated since part of the input energy is reflected back to the floe, meaning that the obtained dissipation is a lower bound. Furthermore, in a realistic ice field, collisions can occur due to multiple floes around the considered piece of ice, which can in turn multiply the energy dissipation due to collisions.

1.2.4 Under ice turbulence

Wave energy in a sea ice field can also be dissipated in the water column under the ice through viscous and turbulent processes. These processes occur when there is a shear in the flow, caused by a solid or liquid interface having a different velocity than the flow. The main difference between viscous and turbulence comes from the linearity (viscous) versus non-linearity (turbulence) of the phenomenon. They are distinguished from each other by calculating the ratio between the inertial forces and the viscous forces of the flow, called the Reynolds number. In wave-ice interactions, the turbulence can come from the friction of the wave orbital motion on the bottom of the ice, called "skin friction" or "basal friction", or from the friction induced by the obstacle that constitutes the entire shape of the ice floe in the wave field, called "form drag" (Kohout et al., 2011; Herman, 2021). Other phenomena can lead to shear, related to wave-ice interactions such like when a wave submerges an ice floe, called "overwash" (Skene et al., 2015; Herman et al., 2019), or when the convergence of two floes induces a downwards water jet in the gap between the floes (Rabault et al., 2019; Løken et al., 2022).

In the modeling literature, wave attenuation due to under-ice turbulence has been mainly addressed through single (Weber, 1987; Liu and Mollo-Christensen, 1988) or multi-layer (De Carolis and Desiderio, 2002) models. For these kinds of models, the energy dissipation in the ocean layer is modelled in the wave attenuation coefficient using the sea water viscosity for laminar flows (Liu and Mollo-Christensen, 1988), and an eddy viscosity

for turbulent flows (Liu et al., 1991; Stopa et al., 2016). The theoretical framework behind the eddy viscosity is discussed in Chapter 3. Contrary to the sea water viscosity, the eddy viscosity is flow-dependent, and thus needs to be parameterized, typically as a function of the area considered as well as the type of ice, to account for the effect of unmeasured variations in ice roughness on the under-ice turbulence. These kinds of models have been included in state of the art waves-in-ice modelling frameworks (Dumont et al., 2011; Williams et al., 2013; Boutin et al., 2018), with the remark that the models outputs are very dependent on the tuning of the eddy viscosity to fit experimental observations, making any reliable forecast very unlikely. In Herman et al. (2019) lab experiments as well, the comparison between the drag coefficient of the literature in case of pure under-ice friction and the much higher effective drag coefficient they measure under multiple wave energy dissipation sources exhibits the impossibility to rely on a single parameter to predict wave attenuation due to wave-ice turbulent interactions. As for the other wave-ice interactions, there is a lack in experimental observation of wave induced under-ice turbulence due to the difficulties inherent to undertaking precise measurements in such extreme environments.

Recent progress has been made in measuring in-situ turbulence under the ice and estimating its importance as a source of wave energy dissipation in the MIZ. Voermans et al. (2019) studied waves in forming ice conditions and low to medium ice concentration, during the Arctic Sea State Program (Thomson et al., 2018), using Surface Wave Instrument Float with Tracking (SWIFT) wave-following drifting buoys that both measure waves and under-ice turbulence. They estimate the impact of under-ice turbulence on wave energy dissipation by computing a turbulence-induced wave attenuation coefficient α_t, with the assumption that all the measured turbulence is due to wave-ice interactions under the ice (i.e. skin friction and form drag). By plotting α_t as a function of the wave attenuation coefficient α, they observe that their data points fall around the one to one curve, meaning that in this case, wave attenuation could be mainly explained by turbulent processes under the ice. A parametrisation is proposed for the turbulence-induced attenuation rate as a function of wave properties and ice concentration, but they admit that work still needs to be done for a larger applicability in other ice conditions (high concentration MIZ, cases with more continuous ice cover or floes much larger than the wavelength), which can involve other sources of turbulence or even different attenuation/dissipation phenomena.

In the paper of Løken et al. (2022), additionally to the collisions described above, they studied the turbulence generated by the motion of the floe. With their setup, they measured the turbulence induced by under-ice friction as well as the turbulence generated when the floe converged and then collided on the walls of the pool. In this very specific case, they obtain that more than 80 % of the total energy dissipation due turbulence was due to under-ice friction. In addition, they obtained that the turbulence was dissipating

nearly 40 % of the power input to the floe. Though very innovative in the scientific field, this experiment does not deal with realistic wave field and ice cover, where the 3D irregularities in the shape of the floes in the 3 dimensions, and the collisions between multiple floes must have an impact to under-ice turbulence.

The main finding of this review of wave-ice interactions is that no model is currently able to adequately predict wave propagation in sea ice and ice dynamics under wavy events, and despite some recent experimental work, it is still not clear which phenomena account for the dissipation of wave energy in the MIZ depending on wave and ice conditions.

1.3 Outline of the thesis

The goal of this thesis was to take part in the experimental efforts to understand wave-ice interactions in the MIZ, particularly related to surface wave attenuation in sea ice. In the following chapters, results are presented from collocated measurements of wave attenuation in sea ice, turbulence under sea ice, and ice floes dynamics made during Bic Winter (BicWin) campaigns in a natural laboratory of the Lower St. Lawrence Estuary (LSLE), in multiple sea-ice conditions. Most of this thesis is based on the paper *L. Barast, P. Sutherland, D. Dumont, and others. Wave attenuation due to under-ice turbulence in natural laboratories* in the process of being submitted to JGR: Oceans.

The structure is the following. Chapter 2 describes working areas, field deployments and data sets along with ice conditions. Chapter 3 deals with measuring wave attenuation in the MIZ. Wave measurements using several types of buoys are described, as well as the calculation of wave parameters, and wave attenuation is quantified using the wave energy attenuation rate per unit of sea surface. The theoretical framework for studying turbulence (in general and in the MIZ) is set out in Chapter 4, before describing the measurements of turbulence in the water column below the ice. The data processing and analysis are then detailed, leading to the formulation of the energy dissipation rate per unit of sea surface due to wave-induced under-ice turbulence. The impact of turbulence on wave attenuation is discussed, and light is shed on the sources of turbulence due to wave-ice interactions. Floe-floe interactions are investigated throughout Chapter 5 to explain most of wave attenuation in the MIZ, depending on the ice conditions. A summary of the main results of this manuscript is provided in Conclusion, along with discussions about some unsuccessful directions, future work on the topic, and a few personal considerations.

Chapter 2

Studying wave-ice interactions in natural laboratories

2.1 Study areas

Although the working conditions for research in the cryosphere have improved significantly since the beginning of polar expeditions, obtaining in-situ measurements to study wave-ice interactions remains a challenge. The extreme weather of storms, freezing temperatures and extensive ice cover make travel very difficult and unsafe. It requires using icebreakers, which are ships able to withstand the pressure of the ice, yet are also rare and expensive. The very changeable conditions make it difficult to predict the deployments, as well as the recovery of the measuring equipment. In addition, the presence of the icebreaker can disrupt the measurement by breaking the ice, and obstructing the wave field. To overcome these difficulties, some measurements are now made by aircraft (e.g. Sutherland et al., 2018) or by satellite (e.g. Gebhardt et al., 2016), but they do not allow to measure everything, especially regarding the turbulence in the water column under the ice. Another issue of experiments like MIZEX, carried out both from icebreakers and with helicopters, is that wave attenuation is estimated using wave buoy separated by long distances (1-10km), which prevents characterizing wave propagation (and generation) as well as ice conditions with sufficient detail to be able to conclude about which physical processes are at play. One solution is therefore to work on smaller areas, since it not only allows the deployment of more instruments and measurement of more relevant physical quantities, but it also limits the variability of the ice and the number of degrees of freedom of the waves.

It is from this observation, and in order to better prepare future missions in the Arctic, that the Bic Winter (BicWin) observational program was initiated and developed through the years, and to which I participated during my thesis. These missions are designed and organized by Dany Dumont and his team from Institut des sciences de la mer à Rimouski (ISMER), and by Peter Sutherland from the Laboratoire d'Océanographie Physique et Spatiale (LOPS). Their principle is to carry out the same type of measurements as in the polar zone, but in the Lower St. Lawrence Estuary (LSLE), more precisely in and around the Baie du Ha! Ha! (BdHH), Parc National du Bic, Quebec, Canada (Figure 2.1, Left),

and in Rimouski Bay (RB) Rimouski, Quebec, Canada (Figure 2.1, Right). BdHH and RB are shallow embayments located on the south shore of the LSLE. BdHH is shaped as a rectangle of width 1 km and length 2 km, and is open to the west-southwest. RB is enclosed between St. Barnabe Island and the coast along Rimouski city, with a width of 3 km on average, and is open at the north-east and at the south-west.

BicWin experiments took place between 2017 and 2020, in February and early March of each year. This period of winter sees most of the estuary covered with sea ice, except from the area starting to the east of BdHH and RB, up to the head the Laurentian Channel, which is a sensible heat polynya due to the uplifting and mixing of deep warmer Atlantic waters (Saucier et al., 2003). Therefore, during westerly wind events, the uncovered area west of BdHH allows the development of waves towards its entrance with up to 80 km of fetch. For RB, this is during northerly winds that waves can form and propagate towards its northern entrance, with up to 100 km of fetch.

BdHH, due to its orientation parallel to the outflow of the St. Lawrence river, its geometry, and its shallow depth, fills with sea ice either through the advection of floes that were formed outside the bay or through thermal growth of landfast ice. The MIZ formed under such conditions has a length from several hundreds of meters up to the full length of the bay and above. In the case of RB, landfast ice cover remains stable in the most shallowest part of the bay during most of the freezing season, and the MIZ is usually formed to the north-east of the bay, where the bathymetry becomes slightly deeper. The life time of a MIZ during the experiments seldom exceeded one to two days, depending on wind and wave events. Further details about the wave and ice conditions related to each experiment are given in section 2.3. This combination of a wave event and a MIZ in such reasonably-sized and accessible areas make BdHH and RB good natural laboratories for studying wave-ice interactions.

2.2 BicWin field deployments

Field experiments consist in daily deployments, similarly to those described in Sutherland and Dumont (2018). During the deployments, we used an ice canoe specially designed to safely travel on virtually any icescape (see Fig. 2.2) It allows unintrusive navigation in the study area, since it leaves the ice field undisturbed, and does not significantly obstruct the wave field. In addition, the ice canoe is a safe ice-going, and allows to store and carry all the equipment we need. Deployment durations range from approximately 30-minutes to more than three hours, depending on multiple constraints (daylight, weather), and the deployment line was in general hundreds of meters long.

A typical deployment is as follows:

- The day before, preparation of the deployment plan and equipment according to the weather forecast. This point could change the next day depending on the presence

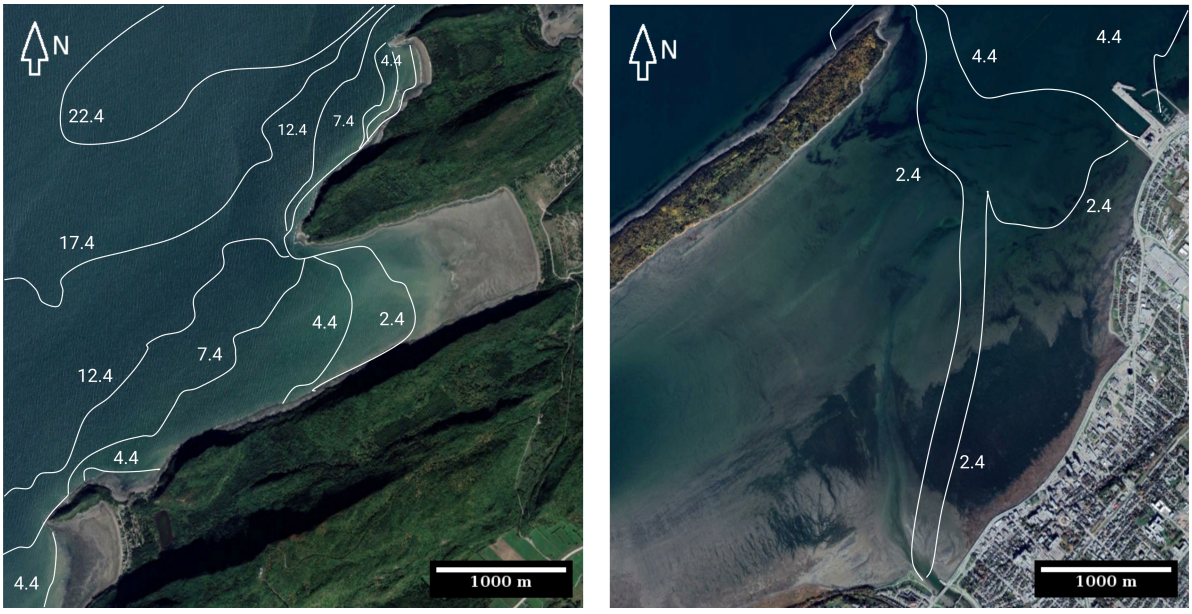

Figure 2.1 – Satellite image of Baie du Ha! Ha! (left) and Rimouski Bay (right) with isobath contours. Satellite data from Landsat / Copernicus. Bathymetry in meters in mean sea level reference, from Canadian Hydrographic Service charts, sounding campaigns from ISMER and soundings during BicWin field deployments.

(or not) of ice in the bays, which could be advected inwards or outwards during the night.

- In the morning, loading the material into sleds to move it to the ice canoe, which was often stationed on the coast near the ice cover.
- Canoe trip to the MIZ. The locomotion is done either by pushing the canoe with one leg, the other being supported inside the canoe, or, when there is not enough sea ice, by rowing. In the team of five canoeists, two at the front are used to steer the canoe in response to the blocks of ice directly in their path, two in the middle are used as a driving force, and the skipper at the back adjusts the trajectory. Measurements (water depth, ice thickness and first wave buoys) are made on the way.
- Once close to the wavy area, measurements begin with the deployment of wave buoys in a line parallel to the direction of the incident wave field, as well as turbulence measuring devices. Where and when possible, Mavic 2 Pro Unmanned Aerial Vehicles (UAVs) are flown to measure the ice properties (the ice concentration, the size of the floes and the location of the ice edge) and the wave field while wave and turbulence measurements are being made.
- Finally, all the equipment is recovered by the canoe and returned to the starting point. The equipment is discharged, rinsed, the batteries changed, the data is downloaded from the instruments, and the deployment is reviewed to consider possible improvements for the next deployment.

Figure 2.2 – Picture taken by a UAV facing North of the ice canoe in operation and its five-member crew during the 2020-02-13 deployment off the BdHH, with Bic Island visible in the back. The pink, red and green objects on the ice floe just to the left of the canoe are respectively the buoy of S497, a SKIB buoy, and the digital cable connecting S497 to a computer to start the data acquisition.

Of course, this is the ideal scenario, and weather conditions (wind speed and direction), the presence/absence of waves and the extent of the ice cover did not always allow to proceed to all of the wanted measurements. For example, during BicWin 2020 that lasted one month, and to which I participated, there were 10 days of deployments among which only 3 allowed to make the turbulence measurements in wavy conditions necessary for my thesis.

2.3 Data sets

Data from nine field deployments that occurred between 2017 and 2020 on nine different days are presented in Table 2.1. 6 of the deployments happened in and off BdHH (Fig. 2.3, Left), and the 3 remaining in RB (Fig. 2.3, Right). More precise maps for each deployment are plotted in Appendix A (Fig. A.2 to A.10). The duration indicated in Table 2.1 is the time span between the very last wave buoy deployment and the very first wave buoy recovery, i.e. the time interval over which all of the wave buoys are recording data.

During each deployment, the under-ice turbulence was measured using at least one Acoustic Doppler Current Profiler (ADCP). Their working principle as well as the different types we used (Aquadopp and s489/s497) are detailed in Chapter 4.

The ice cover conditions displayed in Fig. 2.4 show that the MIZs encountered were generally made of floes with size between less than one meter and a few tens of meters. For most of the days, starting from the coast, the ice cover began as landfast ice, before turning into a more and more wavy MIZ when getting closer to the open ocean. On some of the days (especially on 2017-02-27, 2018-02-26, 2018-03-02, and 2019-03-06), there was a thick layer of slush and brash ice between the floes. For days 2017-02-27, 2018-03-05, 2020-02-13 and 2020-02-27, floes were particularly highly concentrated, packed and rafted.

Therefore, in Table 2.1, four different ice types are specified as encountered on the field deployment area: ice pack/landfast ice (P), large floes (L, e.g. Fig. 2.4.b), small floes (S, e.g. Fig. 2.4.g), and frazil/slush (F, e.g. Fig. 2.4.c). A floe is considered small when its horizontal extent is below 2 m, which corresponds to category 1 of the World Meteorological Organization (WMO), and large when it is over 2 m (mostly category 2 and 3 of the WMO). The ice concentration is estimated from the pictures of the ice cover (see Fig. 2.4) as detailed in Chapter 5. For days when the ice concentration could not be calculated from pictures, the default value $c_{ice} = 1$ was used, in agreement with field observations.

Ice thickness was estimated using a measuring rod with a hook at the end, at the edges of the floes and/or through holes drilled in the ice. The hooked extremity is slid down along the vertical dimension of the floe into the water and then pulled back until the hook meets the bottom of the ice, at which time the thickness of the ice is read from the scale on the rod flush with the top of the ice. Due to the variability in the measured thicknesses, multiple measurements were required for one floe to obtain a reasonable mean. The thickness values presented in Table 2.1 are measured at the location of the ADCP, and are also representative of the mean thickness of the floes in the area around.

The wind speed, wind direction and air temperature are obtained from Environment Canada weather stations 03000 (Ile Bicquette) for BdHH and 02980 (Pointe-au-Père) for RB until 2019. In 2020, they were measured from a self-deployed weather station for BdHH deployments since Ile Bicquette station stopped in 2019. For day 2019-03-06, since we had neither Ile Bicquette weather station nor the self deployed one, data from Pointe-au-Père weather station was used instead. Wave parameters (H_s, f_p and θ_p) are computed from the wave data analysis detailed below.

In addition, the bathymetry data for BdHH was taken from Canadian Hydrographic Service chart 1223, Chenal du Bic, and sounding campaigns from ISMER, and the one for RB was taken from the Electronic Navigational Chart (ENC) Maritime Chart Service of the Canadian Hydrographic Service and from measurements during the deployments at each buoy, with a mean value of 2.4 m. Tidal levels were obtained from the Fisheries and Oceans Canada tide stations 2995 (Bic) and 2985 (Rimouski). Tide phase and amplitude during each deployment are given in Appendix A. Therefore, since all the measurements were localised in space and time, the changes in the depth below every instrument could

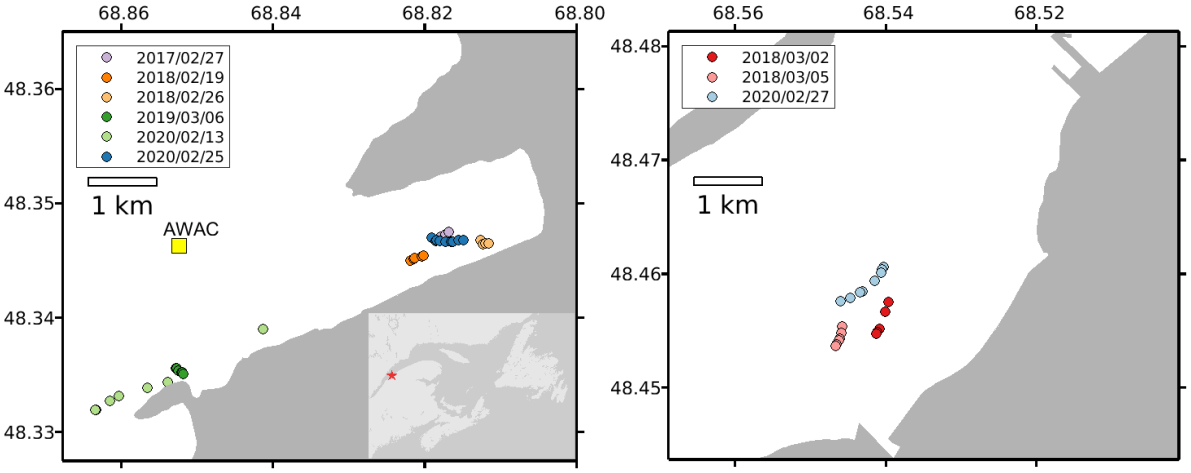

Figure 2.3 – Left - Map of BdHH with the average location of each buoy for each deployments in the bay (coloured dots). The yellow square is the average location of the AWAC between 2017 and 2020. The red star in the thumbnail to the bottom right corner shows the location of BdHH and RB in the LSLE. Right - Map of RB with the average location of each buoy for each deployments in the bay (coloured dots). Coordinates (Longitude West, Latitude North) are in degrees. The code of these maps uses `M_Map` mapping package for Matlab.

be calculated by interpolating the bathymetry and tide level information.

In the following sections, data processing and analysis are illustrated using day 2020-02-25 in BdHH as an example. This specific deployment is a "textbook" case, with an ice cover over the 3/4 of the bay, made up from landfast ice at the back of the bay, and an approximately 300 m MIZ on the bay mouth side. Turbulence measurements were made in two 0.4 m $\times$ 0.4 m holes, one in a large floe still within the packed ice region (see Fig. 2.5), where the wave energy was attenuated by approximately 99 %, and one in a small floe in the wavy area, very close to the ice edge. Two time intervals can be distinguished during this deployment, relative to the two different air-sea state that we encountered. The first one goes from 19:00 UTC to 20:30 UTC, and is characterised by wind-fetched waves entering the BdHH. The second one goes from 20:30 UTC to 21:30 UTC, and is characterised by a drop of the wind velocity in the bay, caused by a change in the wind direction from 250 ° (aligned with BdHH) to 180 ° (BdHH sheltered), along with a progressive decline of the wave state. Hereafter, these two time sections are respectively called T1 and T2.

Table 2.1 – Experimental parameters for the different field experiments

Date	Duration	ADCP	Location	Ice type	c_{ice}	WS	WD	T	H_s	f_p	δ	α
	UTC			P L S F		[km/h]	[deg]	[°C]	[m]	[Hz]	[cm]	[m^{-1}]
2017-02-27	19:31-19:59	Aquadopp	BdHH	□ ■ ■ ■	1	44	250	0.5	1.3	0.2	45	0.029
2018-02-19	17:36-18:35	Aquadopp	BdHH	■ ■ ■ □	1	22	210	2.4	0.4	0.25	65	0.038
2018-02-26	18:08-20:07	Aquadopp	BdHH	□ ■ ■ ■	0.6	30	220	1.2	0.4	0.3	30	0.10
2018-03-02	18:55-19:56	Aquadopp	RB	■ ■ ■ □	1	30	50	-1.1	1.3	0.15	70	0.012
2018-03-05	20:47-21:36	Aquadopp	RB	■ ■ ■ □	1	25	50	0.2	0.5	0.25	50	0.030
2019-03-06	17:15-17:50	Aquadopp	BdHH	□ ■ ■ ■	0.4	15	280	-10.0	0.61	0.25	60	0.021
2020-02-13	17:22-17:57	s489-497	BdHH	□ ■ ■ ■	0.9	28	27	-13	0.23	0.3	100-30	0.012
2020-02-25	19:00-20:30	s489-497	BdHH	■ ■ ■ □	0.9	26	250	1.3	0.37	0.3	33-40	0.033
2020-02-25	20:30-21:30					20	180	1.7	0.30	0.3		0.030
2020-02-27	20:19-20:42	s489	RB	■ ■ ■ ■	1	30	50	-6	1.8	0.1	40	0.008

Ice type: ice pack/landfast ice (P), large floes ≥ 2 m (L), small floes < 2 m (S), and frazil/slush (F)

c_{ice}: ice floe concentration, WS: wind speed, WD: wind dir., T: air temperature, H_s: significant wave height,

f_p: wave peak frequency, δ: ice thickness at ADCP, α: wave attenuation coefficient

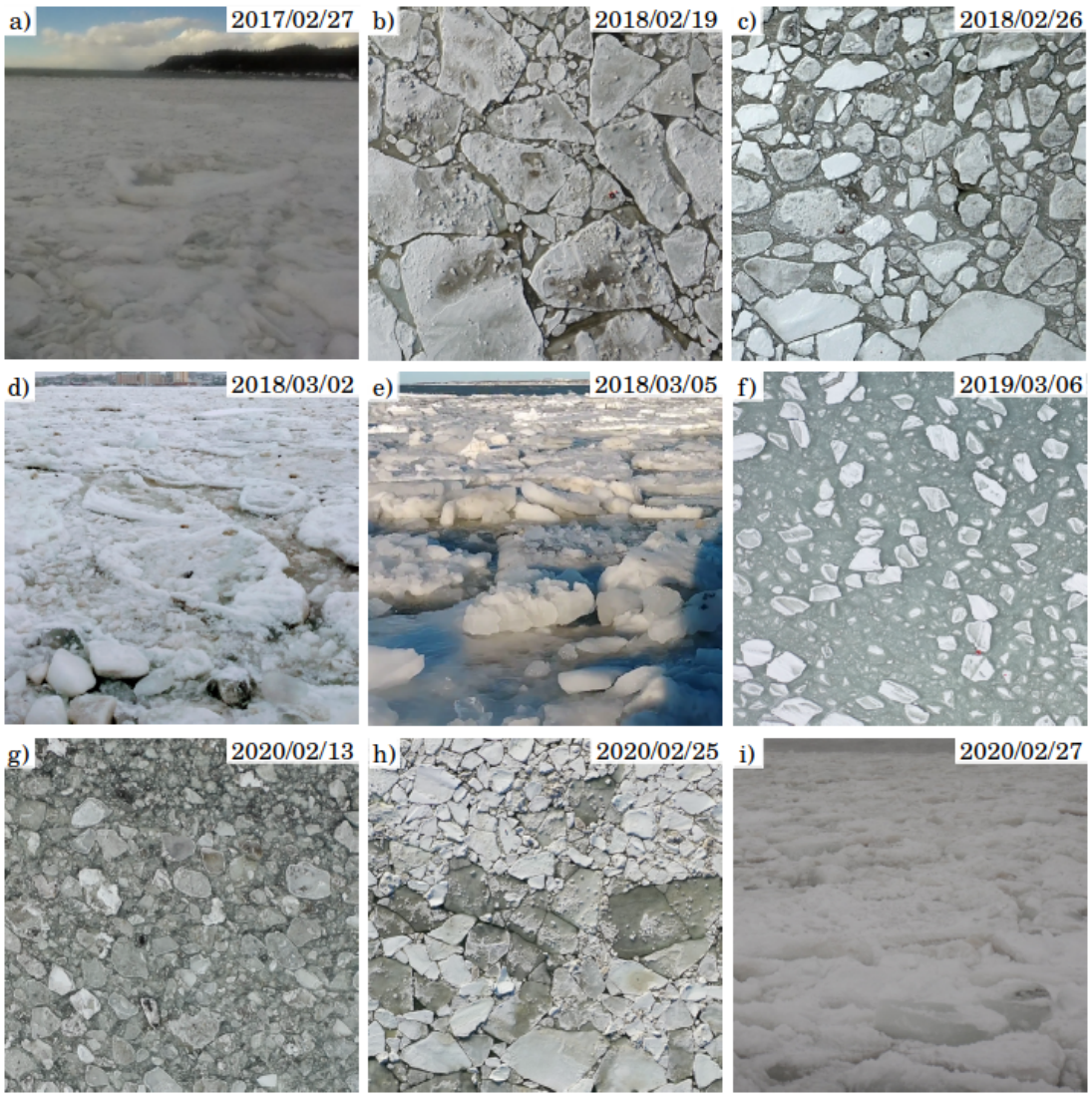

Figure 2.4 – Ice cover conditions near the most outwards ADCP for all of the deployments. Pictures b), c), f), g) and h) represents a square of 40 m × 40 m, with the top orientated towards the ice edge. They were taken from a drone looking vertically downwards. The remaining pictures, a), d), e), and i), were taken by a hand-hold compact camera or Go-Pro looking horizontally, with the floes in the foreground having a scale of approximately 1 to 2 m.

Figure 2.5 – Example of one wave buoy (bottom) and one ADCP (center) deployed on the same floe in the pack ice region on day 2020-02-25, while I am programming the ADCP.

Chapter 3

Wave propagation and attenuation in sea ice

3.1 About ocean waves ...

3.1.1 ... in the open ocean

Most of the knowledge about ocean waves presented here is based on the book *Ocean waves in geosciences* by Ardhuin and Filipot (2019).

Ocean waves are characterised by amplitudes a, frequencies f, wavelengths λ, directions θ and a dispersion relation linking time and space domains. In the case of small slope waves over a flat ocean bottom, which is consistent with the framework of this thesis, the Navier-Stokes equations describing the fluid motion can be linearized, allowing to find an analytic expression for the dispersion relation:

$$\omega^2 = gk \tanh(kD_h), \tag{3.1}$$

where $\omega = 2\pi f$ is the wave angular frequency, $k = 2\pi/\lambda$ is the wave number, g is the gravity constant and D_h is the mean water depth. The phase velocity $C = \frac{\omega}{k}$ and the group velocity $C_g = \frac{\partial \omega}{\partial k}$ are directly derived from Eq. 3.1:

$$C = \left(\frac{g}{k}\tanh(kD_h)\right)^{1/2} \tag{3.2}$$

$$C_g = \tfrac{1}{2}\left(\tfrac{g}{k}\tanh(kD_h)\right)^{1/2} - \tfrac{1}{2}(gk\tanh^3(kD_h))^{1/2}\left(D_h[1-\coth^2(kD_h)]\right). \tag{3.3}$$

Moreover, supposing that the waves are monochromatic and following Airy (1841), analytical solutions can be found for the velocity components of the flow:

$$\mathbf{u} = a\frac{\mathbf{k}}{k}\omega\frac{\cosh(kz+kh)}{\sinh(kD_h)}\cos\theta \tag{3.4}$$

$$w = a\omega\frac{\sinh(kz+kh)}{\sinh(kD_h)}\sin\theta \tag{3.5}$$

where $\mathbf{u} = (u, v)$ is the vector of the horizontal velocities along the directions x and y, and w is the vertical velocity along direction z, $\mathbf{k}$ is the wave number vector, and h is the

total water depth, accounting for the tide and the bathymetry. Last, the total energy for a wave train is:

$$E_{\text{tot}} = \frac{1}{2}\rho_w g a^2 \tag{3.6}$$

for which ρ_w is the density of sea water.

Realistic sea states are composed of random waves, and are often described using spectral analysis. In that case, the superposition of waves of different frequencies and directions that form the sea state is described using Fourier transform (Longuet-Higgins et al., 1963), and their energy spectrum is given by

$$E(f,\theta) = \lim_{\Delta f \to 0} \lim_{\Delta \theta \to 0} \frac{1}{\Delta f \Delta \theta} \frac{a_{i,j}^2}{2}, \tag{3.7}$$

where $a_{i,j}$ is the amplitude of the Fourier mode i in the direction θ_j. Compared to E_{tot}, there is a missing $\rho_w g$ that is often omitted, meaning that $E(f,\theta)$ is, strictly speaking, the spectrum of the wave elevation variance. From this quantity, most of the information of the wave field can be retrieved, except the phases of the waves. A parameter of the wave field that is often used to describe wave height is the significant wave height, H_s, that correspond to the visual height of the waves, and can be computed from the wave energy spectrum:

$$H_s = 4\sqrt{E} = 4\sqrt{\int_0^\infty \int_0^{2\pi} E(f,\theta) df d\theta}. \tag{3.8}$$

A representative value of the wave amplitude a can be computed likewise as half of the Root Mean Square (RMS) wave height, H_{RMS}:

$$a = H_{\text{RMS}}/2 = \sqrt{2E}. \tag{3.9}$$

The RMS wave orbital velocity can also be computed from the wave omnidirectional spectrum $E(f)$ at sea surface,

$$U_{surf} = 2\pi \sqrt{\int_0^\infty \frac{f^2 E(f)}{\tanh(kD_h)^2} df}, \tag{3.10}$$

and at sea bottom,

$$U_{bot} = 2\pi \sqrt{\int_0^\infty \frac{f^2 E(f)}{\sinh(kD_h)^2} df}. \tag{3.11}$$

The mean wave period T_{m01} is

$$T_{m01} = \frac{\int_0^\infty E(f) df}{\int_0^\infty f E(f) df}. \tag{3.12}$$

Other parameters like the peak period T_p, the peak frequency $f_p = 1/T_p$ or the peak

wavelength λ_p are derived from the location of the maximum of the omnidirectional spectrum $E(f)$.

Last, the mean wave direction $\theta_m(f)$ is deduced from the integral parameters $a_1(f)$ and $b_1(f)$ using wave spectra and co-spectra (Longuet-Higgins et al., 1963) such that:

$$\theta_m(f) = \arctan(b_1(f)/a_1(f)), \tag{3.13}$$

The peak direction of the most energetic waves is then $\theta_p = \theta_m(f_p)$.

3.1.2 ... in presence of sea ice

Wave propagation is modified due to the mechanical response of the ice. Liu and Mollo-Christensen (1988) account for the flexure and compression of ice floes to obtain the wave dispersion relation in a field of ice floes:

$$\omega^2(k) = \left[gk + \underbrace{\frac{Y\delta^3 k^5}{12(1-s^2)\rho_w}}_{\text{Flexure}} - \underbrace{\frac{P\delta k^3}{\rho_w}}_{\text{Compression}} \right] \left(\coth(kD_h) + \underbrace{\frac{\rho_I \delta k}{\rho_w}}_{\text{Mass loading}} \right)^{-1} \tag{3.14}$$

where ρ_w is the sea water density, ρ_I is the sea ice density, δ is the ice thickness, Y is Young's modulus of the ice, P is the compressive stress in the ice, and s is the Poisson ratio for the ice. In this equation, the mass loading term represents the effect of the sea water volume displacement under the presence of ice due to the buoyancy.

In the active area of the MIZ where most of the measurements were made, the floes were generally smaller than the wavelength, and thus did not flex nor break. Therefore, the dispersion relation that will be used in the analysis below is:

$$\omega^2(k) = gk \left(\coth(kD_h) + \frac{\rho_I \delta k}{\rho_w} \right)^{-1} \tag{3.15}$$

The phase speed is then

$$C = \left(\frac{g}{k}\right)^{1/2} \left(\coth(kD_h) + \frac{\rho_I \delta k}{\rho_w} \right)^{-1/2}, \tag{3.16}$$

and the group speed

$$\begin{aligned} C_g = \; & \tfrac{1}{2}\left(\tfrac{g}{k}\right)^{1/2} \left(\coth(kD_h) + \tfrac{\rho_I \delta k}{\rho_w} \right)^{-1/2} \; - \\ & \tfrac{1}{2}(gk)^{1/2} \left(\coth(kD_h) + \tfrac{\rho_I \delta k}{\rho_w} \right)^{-3/2} \; \times \; \left(D_h[1 - \coth^2(kD_h)] + \tfrac{\rho_I \delta}{\rho_w} \right). \end{aligned} \tag{3.17}$$

All of the other wave characteristics and parameters (e.g. $E(f,\theta)$, H_s and θ_m) can be

computed in the same way as for open ocean waves.

3.2 Measuring waves in sea ice

Wave measurements during the BicWin field missions were made using Surface Kinematic Ice Buoys (SKIBs), specially designed to be placed on the ice, and Sofar Spotter buoys, deployed in the slush or open water between ice floes close to the ice edge. SKIBs are developed by IFREMER and consist of a data logger, a GPS, an Iridium satellite modem, and a wave sensor (Guimarães et al., 2018). All of the electronics and batteries are enclosed within a cylindrical box with a cap, as in Fig. 2.5, for easy manipulation during the deployments. Two different wave sensors are used: 1) SBG Systems Ellipse-N GPS inertial navigation system (hereafter referred to as SBG) and 2) Vectornav VN-100 inertial motion unit (hereafter referred to as VNAV) both with a 50 Hz sampling frequency (Guimarães et al., 2018). They measure the acceleration (see Fig. 3.1.b and c) and the angular momentum of the SKIBs. Spotter buoys directly measure the displacement of the sea surface using their onboard GPS sensor, with a 2.5 Hz sampling frequency (see Fig. 3.1.a). One important difference between each of these buoys is their sensitivity to wave motion; the noise floor of the SBG buoy is slightly lower than that of VNAV buoys, which is lower than that of the Spotter buoys. Therefore, Spotter buoys were placed close to the ice edge, where wave heights are larger. VNAV and then SBG buoys were placed farther into the MIZ. The noisier acceleration signal in Fig. 3.1.c, compared to Fig. 3.1.b, is in part due to the higher noise level of VNAV wave sensor, and in part due to the fact that the VNAV SKIB was placed at a larger ice fetch than the SBG SKIB. All of the buoys were deployed in a line parallel to the ice fetch as explained in Chapter 2, and an example of their average position for each deployment, measured from internal GPS, is shown on Fig. 2.3.

In BdHH, in addition to the buoys deployed from the canoe, a Nortek Acoustic Wave And Current profiler set-up in wave-mode was moored on the sea bed at a depth of 16 m (chart datum) for the whole winter season to make measurements of the incoming wave field (see Figure 2.3). It was programmed to measure waves during 4.26 min bursts at 4 Hz every hour. For the present work, the raw AWAC data were processed by colleagues at ISMER-UQAR, who provided me with wave 2D spectrum in frequency and direction $E(f, \theta)$.

3.3 Wave data processing

Wave data were analysed using 10-minute time segments. This duration was a good compromise to capture wave dynamics, since the limited fetch did not allow to have wave period much longer than 10 s, while maintaining stationarity at the location of the buoys.

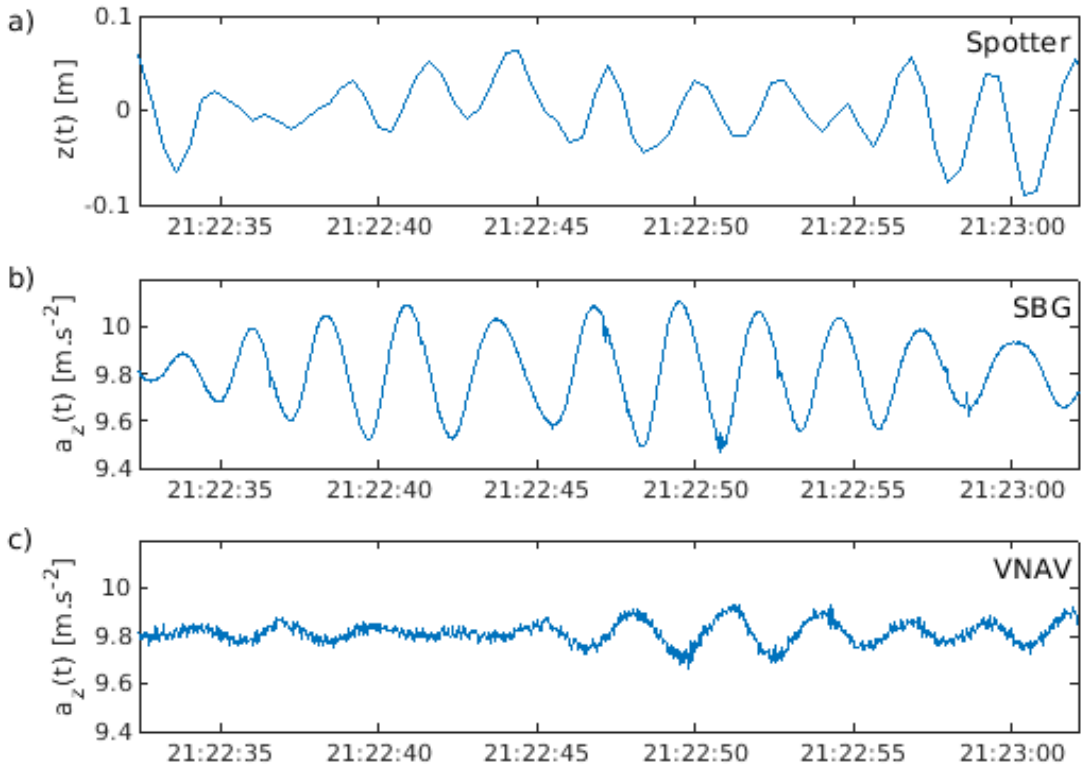

Figure 3.1 – Samples of the raw vertical GPS position data of a) Spotter 112 and the raw vertical acceleration data of b) SKIB 11 (SBG) and c) SKIB 3 (VNAV) with time, on day 2020-02-25, at a) 5, b) 40 and c) 75 m from the ice edge along wave direction. The time indicated is UTC.

During the deployments, the buoys could drift due to the tidal currents and to the wave radiation stress. Within 10 minutes, this drift was short enough to avoid any significant changes in the ice cover and wave dynamics in the vicinity of the buoys.

Following Longuet-Higgins et al. (1963) and Herbers et al. (2012), wave auto-spectra and co-spectra are computed from the acceleration data for SKIBs, and from the elevation data for spotter buoys, using windowed Fast Fourier Transform (Welch, 1967) to compute Power Spectral Densitys (PSDs). The number of overlapping windows for each 10-minute interval was set to 21, with a 50 % window overlap and a Hann window type which both are typical and well suited for that kind of data analysis. Thus, the duration of a window was 54 s, which allows to have several representations of even the longest wave (10 s) I observed in the data, and short enough to have a satisfying frequency resolution (0.02 Hz).

Fig. 3.2 shows wave omnidirectional energy density spectra $E(f)$ for day 2020-02-25 (spectra for the other days are plotted in Fig. A.11). Centered close to 0.3 Hz is the wave peak energy, that is used to compute the parameters of the dominant propagating waves. The abrupt slope for spotter buoys data (cf. on Fig. 3.2, between 1 and 1.23 Hz for buoy 112) is due to the internal filtering of the buoy, and nearly correspond to the Nyquist frequency (half of the sampling frequency, 1.25 Hz here) of the spectrum. This drop happens before reaching the noise level of the buoy. For SKIBs, the noise floor is computed using a linear least square fit of $\log(E(f))$ with respect to $\log(f)$ between 5 and 25 Hz, where a -4-slope is expected. Indeed, the acceleration spectra is multiplied by f^{-4} to derive wave elevation spectra in m^2.s, and the acceleration noise is white, so that the noise of the wave elevation spectrum is the product of constant noise by f^{-4}. This procedure is repeated for each spectrum of each SKIB, at each 10-minute time interval. Then, the computed noise floors are subtracted from the wave spectra to avoid accounting for spurious energy at high frequency (Thomson et al., 2021).

The confidence interval $[dE^-(f), dE^+(f)]$ of the PSD is computed using the chi-squared method following Bendat and Piersol (1987, p. 430):

$$[dE^-(f), dE^+(f)] = \left[\frac{n_{\mathrm{df}} E(f)}{\chi^2_{n_{\mathrm{df}}}(1-\frac{\mathrm{conf}}{2})}, \frac{n_{\mathrm{df}} E(f)}{\chi^2_{n_{\mathrm{df}}}(\frac{\mathrm{conf}}{2})}\right] = [e^-, e^+]E(f), \tag{3.18}$$

In Eq. 3.18, n_{df} is the number of degrees of freedom of the PSD, equal here to the number of windows, 21, conf is the confidence coefficient, set to $1 - 0.95 = 0.05$, and $\chi^2_{n_{\mathrm{df}}}$ is the inverse chi-squared distribution for n_{df} degrees of freedom. The + and − signs in exponent of e are due to the fact that the chi-square distribution is skewed, meaning that $e^+ \neq e^-$. The additive relative errors on $E(f)$ are then

$$\frac{dE^{\pm}(f)}{E(f)} = \pm(\pm e^{\pm} \mp 1). \tag{3.19}$$

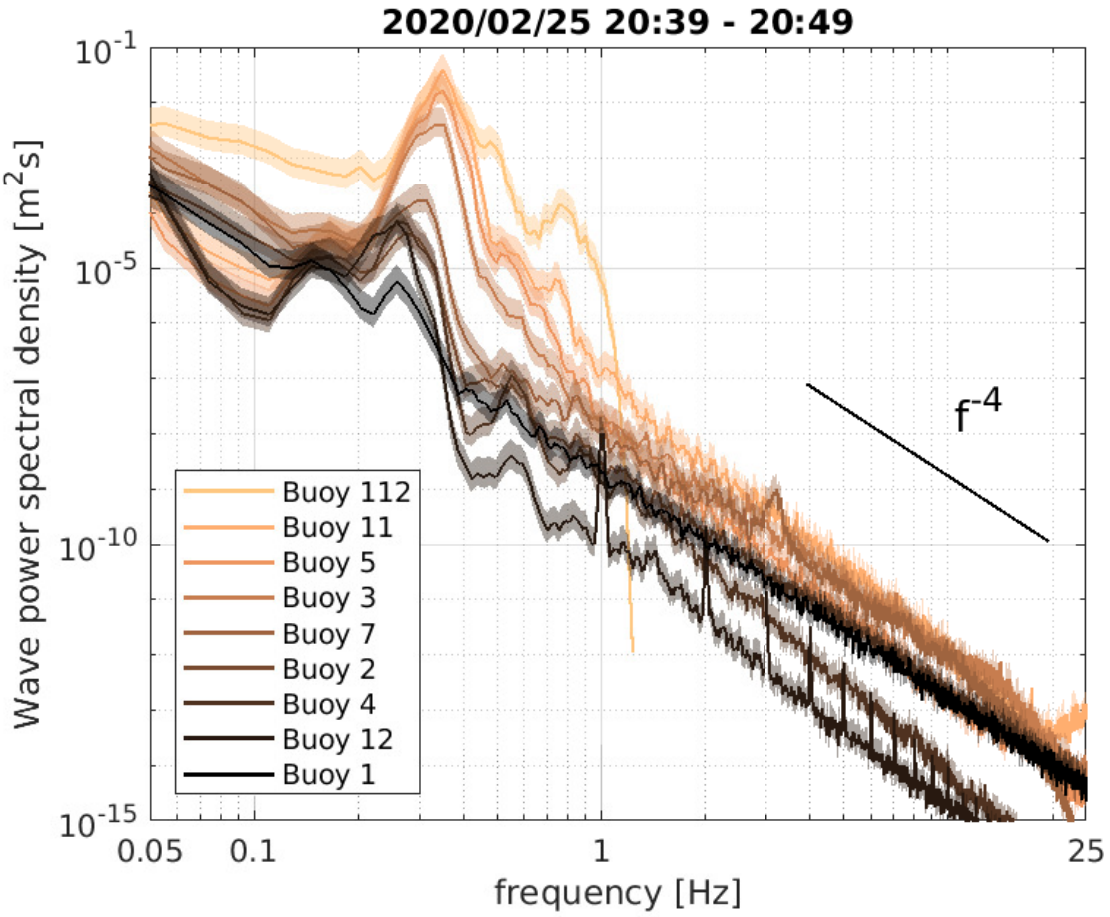

Figure 3.2 – Wave energy spectra in the MIZ as a function of frequency during a 10-min interval of T2, 2020-02-25. Each color corresponds to one buoy number, the lighter the color the closer the buoy is to the ice edge. The confidence intervals are computed from the chi-squared method.

3.4 Wave attenuation

Wave energy $E(x_{\text{ice}})$ as a function of the ice fetch x_{ice} is computed by integrating wave energy density over a valid range of frequencies for all of the wave buoys located at different x_{ice}:

$$E(x_{\text{ice}}) = \int_{f_{\min}}^{f_{\max}} E(f)df. \tag{3.20}$$

This range was first chosen to avoid accounting for the effect of the currents ($f_{\min}$ = 0.02 Hz) up to the Nyquist frequency ($f_{\max}$ = 25 Hz). In practice, the contribution of $E(f)$ to E over 2 Hz is insignificant due to the very low values, and is mostly noise. Below 0.1 Hz, this contribution is most often below 1 to 10 %, except for buoys that are on the ice pack, far away from the ice edge, and can be attributed to noise as well. Hence, the frequency interval chosen hereafter is $f_{\min} = 0.1$ Hz and $f_{\max} = 2$ Hz.

The ice fetch x_{ice} is computed for a wave buoy using the location in UTM of the buoy (x_b, y_b), the location in UTM of the ice edge (x_e, y_e), and the peak wave direction θ_p. The buoy location was derived from the buoy GPS, and the wave direction from the wave spectrum. The ice edge location is in some cases derived as a line from UAV pictures since they are geolocalised. In that case, the ice fetch is just the Euclidean distance between the ice edge and the buoy along the direction θ_p. When there are no UAV pictures, the ice edge location is estimated by using the buoy the closest to the ice edge, counting the number of wavelengths (0-5) from the buoy to the ice edge. The counting is done visually in the field or through a low-resolution video captured using a handheld compact camera when available. In this second situation, the wave direction was nearly perpendicular to the ice edge, so that the ice fetch is the Euclidean distance between the buoy and the line passing through point (x_e, y_e) and of direction $\theta_p + 90$ °. In any case, the error on the value of the ice fetch, dx, is computed as the standard deviation of each wave buoy location, over each 10-minutes sample.

The integrated wave energy E is derived for each 10-minutes interval using all of the wave buoys. The relative error on wave energy for each 10-minutes interval, $\frac{dE}{E}$, is equal to the relative error on $E(f)$ since $e^{\pm}$ does not depend on the frequency. As shown in Fig. 3.3, $E(x_{\text{ice}})$ decreases with distance to the ice edge. The data points for this graph are obtained after averaging wave energy over $T1$ and $T2$, i.e. over several of the 10-minutes intervals. Therefore, the error on E have been recomputed, accounting for the change in number of degrees of freedom (21× number of 10-min intervals in $T1$ or $T2$). The standard deviation of E has also been added to the error since it became significant.

A linear least square fit of the logarithm of the wave energy is computed at each 10-minutes interval,

$$E(x_{\text{ice}}) = E_0 e^{-\alpha x_{\text{ice}}}, \tag{3.21}$$

where E_0 is the energy of the incoming wave field, and the wave energy attenuation

coefficient α is reported in Table 2.1. For cases in BdHH, the value of $E_{0,\text{fit}}$ derived from the fit was comparable to the estimation of $E_{0,\text{AWAC}}$ using the measurements of the AWAC. Indeed, on Fig. 3.3, for time interval T1, the square representing $E_{0,\text{AWAC}}$ is very close to the point where the line representing the fit crosses the ordinates. This is less true for time interval T2 (~ 40 % of error), yet the reason is unclear. In that situation, the value of H_s that is considered for the analysis and shown in Table 2.1 is $H_s = 4\sqrt{E_{0,\text{AWAC}}}$. When AWAC data was unavailable, the value $H_s = 4\sqrt{E_{0,\text{fit}}}$ was used instead. In most of the cases of this second situation, one of the Spotter buoys was not far from the ice edge, and allowed to check that the value of $E_{0,\text{fit}}$ was physically realistic. The values of α, between 0.01 and 0.1, are several orders of magnitude higher than the historical literature (Wadhams et al., 1986; Squire et al., 1995; Meylan et al., 2018), but close to more recent works (Rabault et al., 2017; Voermans et al., 2019) in similar ice conditions.

3.5 Total wave energy attenuation rate

To compare wave energy attenuation to wave energy dissipation due to wave-ice interactions, the quantity that has been considered for this work is the total energy attenuation/dissipation rate per unit of sea surface area Γ, expressed in W.m^{-2}. This quantity is often calculated for the turbulence in the oceanic boundary layers, in order to determine the amount of energy that is dissipated due to turbulent processes in the water column (Thomson, 2012; Stevens et al., 2009; Voermans et al., 2019).

For the waves, it is calculated as the residual wave energy flux through a control volume, delimited by two subsequent buoys here, and aligned with the wave direction. To do so, I computed wave energy flux Φ at each buoy n, located in $x_{\text{ice},n}$, defined as

$$\Phi(x_{\text{ice},n}) = \rho_w g \int_{f_{\min}}^{f_{\max}} E(f, x_{\text{ice},n}) C_g(f) df, \tag{3.22}$$

where $C_g(f)$ is the group velocity of the waves computed from the dispersion relation in sea ice Eq. 3.15, $\rho_w = 1020$ kg.m^{-3} is the sea water density (for sea water at temperature -2 °C and salinity 28 psu), and $g = 9.81$ m.s^{-2} is the gravity constant.

Then, the total wave energy attenuation rate per unit of surface area, Γ_{w}, is calculated using two consecutive buoys (n and $n+1$), as an approximation of the spatial gradient of the wave energy flux

$$\Gamma_{\text{w}}(x_{\text{ice,r}}) = -\frac{\Delta\Phi}{\Delta x} = -\frac{\Phi_n - \Phi_{n+1}}{x_{\text{ice},n} - x_{\text{ice},n+1}}. \tag{3.23}$$

The location $x_{\text{ice,r}}$ of this attenuation rate is set at the mid distance between the buoys n and $n+1$, i.e. $x_{\text{ice,r}} = 0.5(x_{\text{ice},n} + x_{\text{ice},n+1})$, with an error Δx extending between the two buoys (see Fig. 3.4).

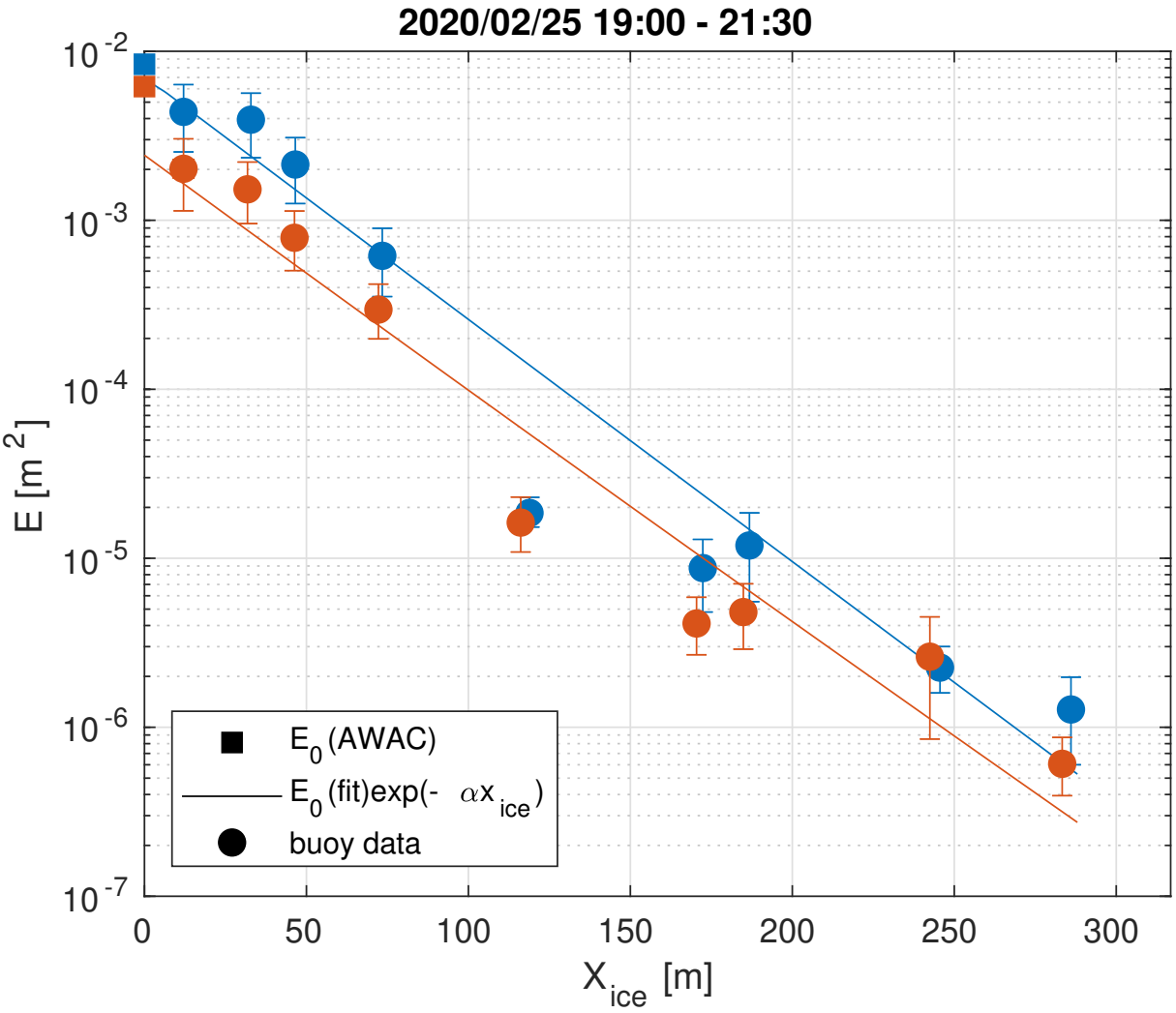

Figure 3.3 – Wave energy as a function of distance from the ice edge x_{ice}, 2020-02-25. Blue dots are time averages of the wave energy during T1, and orange dots are time averages of the wave energy during T2. The straight lines are exponential fit to the data in the MIZ. The square dots represent the incoming wave energy measured by the AWAC when the sea water above is free of ice. The horizontal error bars are smaller than the dots representing the data points.

The errors on Γ_{w} are divided in two categories. On the one hand, there are statistical errors, $d\Gamma_w^{\pm}$ here, that come from the spatial and temporal variations in measured quantities. And on the other hand, there are physical errors that result from other physics at stake leading to wave attenuation, yet measured in Γ_{w}. Here, the physical error, $d\Gamma_{\mathrm{wbt}}$, is due to wave friction on sea bottom, which is accounted for because the study areas are shallow. Since this physical phenomenon is increasing wave attenuation, it is considered as a negative error. The total errors on Γ_{w} are the sum of the statistical and physical errors:

$$\begin{aligned} d\Gamma^{+}_{\mathrm{w,tot}} &= d\Gamma^{+}_{\mathrm{w}} \\ d\Gamma^{-}_{\mathrm{w,tot}} &= d\Gamma^{-}_{\mathrm{w}} \quad + \quad d\Gamma_{\mathrm{wbt}} \end{aligned} . \tag{3.24}$$

The statistical errors on Γ_{w} are computed using error propagation on Eq.3.23:

$$\frac{d\Gamma^{\pm}_{\mathrm{w}}}{\Gamma_{\mathrm{w}}} = \left[\left(\frac{d\phi^{\pm}(x_{\mathrm{ice},n})}{\Phi(x_{\mathrm{ice},n})} \right)^2 + \left(\frac{d\Phi^{\pm}(x_{\mathrm{ice},n+1})}{\phi(x_{\mathrm{ice},n+1})} \right)^2 + \left(\frac{dx_{\mathrm{ice},n}}{x_{\mathrm{ice},n}} \right)^2 + \left(\frac{dx_{\mathrm{ice},n+1}}{x_{\mathrm{ice},n+1}} \right)^2 \right]^{1/2}, \tag{3.25}$$

where $d\Phi^{\pm}(x_{\mathrm{ice},n})$ and $d\Phi^{\pm}(x_{\mathrm{ice},n+1})$ are the statistical error on Φ at buoy n and $n+1$, and $dx_{\mathrm{ice},n}$ and $dx_{\mathrm{ice},n+1}$ are the statistical errors on the ice fetch $x_{\mathrm{ice},n}$ and $x_{\mathrm{ice},n+1}$ of the buoys n and $n+1$.

The statistical errors on the ice fetch of each buoy are computed as the standard deviation of the ice fetch of the buoys over the 10-minutes intervals. They are most of the time pretty low compared to the ice fetch (a couple of percents), even for day 2020-02-13 where the ice drifted significantly with the current, since this drift remained parallel to the ice edge. The statistical errors $d\Phi^{\pm}$ on Φ are computed using error propagation, for a product of variables, on Eq. 3.22:

$$\frac{d\Phi^{\pm}}{\Phi} = \left[\left(\frac{\int dE^{\pm}(f) df}{\int E(f) df} \right)^2 + \left(\frac{\int dC_g(f) df}{\int C_g(f) df} \right)^2 \right]^{1/2}, \tag{3.26}$$

where $dE^{\pm}(f)$ is the statistical error on $E(f)$ and dC_g is the statistical error on C_g. The error on C_g is also computed using error propagation, on Eq. 3.15:

$$dC_g = \left[\left(\frac{\partial C_g dD_h}{\partial D_h} \right)^2 + \left(\frac{\partial C_g d\delta}{\partial \delta} \right)^2 \right]^{1/2}. \tag{3.27}$$

In Eq. 3.27, dD_h is the statistical error on the water depth, roughly estimated to 0.5 m from the tide variation over the 10-minutes intervals and from the interpolation of the location of the buoys over the bathymetry grid. $d\delta$ is the statistical error on the ice thickness, which represents 30 % of δ in standard deviation, according to Sutherland and Dumont (2018). On average, these errors lead to less than 5 % of error on C_g. Moreover,

the group velocity is computed at each buoy, and appears to remain independent of the ice fetch for frequencies within the wave energy spectrum peak, with less than 2 % deviation, and little dependant of the ice fetch for frequencies away from the wave energy spectrum peak, with less than 25 % deviation. These deviations are estimated between the buoy the closest to the ice edge and the farthest away from the ice edge, and are much lower when computed between two subsequent buoys.

The relative error on Φ due to the error on E is 40 % for the lower band and 100 % for the upper band, which is much larger than the average error on C_g, meaning that the statistical errors on Φ are mostly due to the statistical errors on wave energy, E. The statistical errors on Γ_{w}, due to the errors on Φ and x_{ice}, are thus generally dominated by the errors on E.

To compute the physical error $d\Gamma_{\mathrm{wbt}}$, I followed Holthuijsen (2007, p. 276),

$$d\Gamma_{\mathrm{wbt}}(x_{\mathrm{ice}}) = \overline{\tau_{\mathrm{bot}} U_{\mathrm{bot}}}, \tag{3.28}$$

where $\overline{\tau_{\mathrm{bot}}}$ is the mean sea bottom wave shear stress, and U_{bot} is the RMS sea bottom wave orbital velocity (see Eq. 3.11).

The flow generated by waves over sea bottom can be either turbulent or laminar. The phenomenon of turbulence in the oceanic boundary layer is discussed in Chapter 4, so it is not detailed here. In the different cases discussed throughout this work, the Reynolds number for waves flow at sea bottom, $\mathrm{Re}_{\mathrm{wb}}$, is between 1 and 10^4, which is much below the critical value of 1.5×10^5 that it must reach for the flow to be considered turbulent, which would mean that the flow due to the waves is laminar. However, another threshold for the wave Reynolds number, Re_{T}, seems to be of importance according to the discussion in Chapter 4, which led me not to directly dismiss the possibility of a turbulent wave flow. Under these circumstances, I decided to compute the sea bottom wave shear stress for both laminar and turbulent flow, and then to use the largest of the two in Eq. 3.28.

The sea bottom wave shear stress for laminar flow is (Soulsby, 1997)

$$\tau_{\mathrm{bot,l}} = \rho_w \mathrm{Re}_{\mathrm{wb}}{}^{-0.5} U_{\mathrm{bot}}^2, \tag{3.29}$$

where $\mathrm{Re}_{\mathrm{wb}}$ is computed using Eq. 4.10.

The sea bottom wave shear stress for turbulent flow is (Soulsby, 1997)

$$\tau_{\mathrm{bot,t}} = \rho_w C_{\mathrm{Dwb}} U_{\mathrm{bot}}^2, \tag{3.30}$$

with a sea bottom wave drag coefficient C_{Dwb}. The sea bottom wave drag coefficient is computed following Soulsby (1997) for rough sea bottom:

$$C_{\mathrm{Dwb}} = \frac{1}{2} \times 1.39 \left(\frac{U_{\mathrm{bot}} T_{m01}}{2\pi z_0} \right)^{-0.52} \tag{3.31}$$

where z_0 is the bottom roughness, which is equal to $z_0 = 1.8 \times 10^{-2}$ mm for muddy flat bottom (Andersen et al., 2007). The mean wave period T_{m01} is computed using Eq. 3.12.

After calculating both stresses for all data sets, it appears that the laminar stress consistently outweighs the turbulent stress, which would supports the fact that the wave friction on the bays bottom is laminar. It gives an error $d\Gamma_{\mathrm{wbt}}$ that accounts for less than 5 % of Γ_{w} for the shallowest deployments, where it is expected to be the largest.

To add $d\Gamma_{\mathrm{wbt}}$, which is computed at buoy location, x_{ice}, to $d\Gamma^{-}_{\mathrm{w}}$, which is computed at $x_{\mathrm{ice,r}}$, $d\Gamma_{\mathrm{wbt}}$ has to be interpolated on the $x_{\mathrm{ice,r}}$ values. The reason why I detail these calculations below, for such a small error contribution, is that they will be useful in the following Chapters. Indeed, this interpolation is also used to estimate the value of Γ_{w} at any given ice fetch x_{ice}. This value is then compared with the total energy dissipation rates per unit sea surface area calculated for various wave-ice interaction processes.

To find what interpolation to use, I started by investigating what theoretical profile could be expected for Γ_{w} with respect to $x_{\mathrm{ice,r}}$. By substituting Eq. 3.22 and 3.21 in Eq. 3.23, considering that C_g is independent of x_{ice} and using the integrated form of α, Γ_{w} becomes

$$\Gamma_{\mathrm{w}}(x_{\mathrm{ice,r}}) = \alpha\rho_w g e^{-\alpha x_{\mathrm{ice,r}}} \int E_0(f) C_g(f) df = \Gamma_0 e^{-\alpha x_{\mathrm{ice,r}}}, \tag{3.32}$$

with $\Gamma_0 = \alpha\rho_w g \int E_0(f) C_g(f) df$. Therefore, as for the wave energy, an exponential decay is also expected to hold for Γ_{w}.

Fig. 3.4 shows that the exponential decay hypothesis is globally acceptable, although approximate. In practice, not all of the data points fall on the fit line within the uncertainties, even though they are not far from it. This discrepancy is probably due to different ice conditions depending on the ice fetch. Typically, the ice cover near the edge is more fragmented, disorganized, and made up of small ice floes, whereas the ice cover further from the edge is more structured and consists of larger ice floes. To address this discrepancy, a solution has been adopted to consider a different exponential decay between each pair of consecutive data points, as illustrated in Fig. 3.4. The coefficients Γ_0 and α of each independent decay are obtained by calculating the equation of the line passing through the two points considered in logarithmic scale. This approach is in fact interpolating the data linearly in logarithmic space.

As a conclusion concerning the errors on Γ_{w}, after adding statistical and physical errors, the average positive error $d\Gamma^{+}_{\mathrm{w,tot}}$ is about 150 % of Γ_{w} and the average negative error $d\Gamma^{-}_{\mathrm{w,tot}}$ is about 60 % of Γ_{w}.

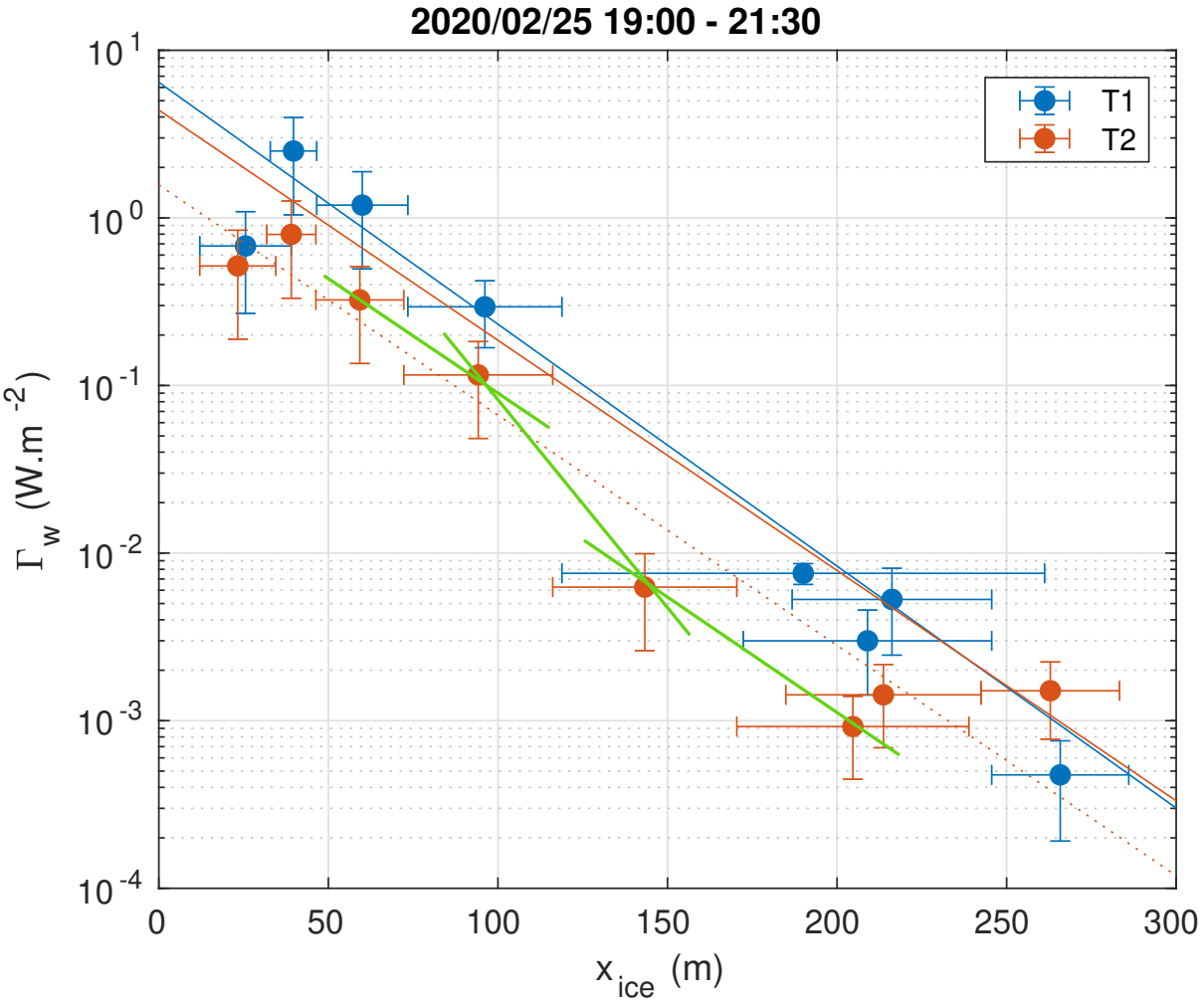

Figure 3.4 – Example of total wave attenuation rate per unit of sea surface area Γ_w as a function of the ice fetch $x_{ice,r}$ for intervals T1 (blue) and T2 (orange) of day 2020-02-25. The dots with error bars are averages of Γ_w over each interval. The solid lines represent Eq. 3.32, where Γ_0 and α are averaged over each interval, and Γ_0 is computed from $E_{0,\mathrm{AWAC}}$. The dashed line for T2 is nearly the same than the solid line, but Γ_0 is computed from a least square fit of the data this time. The green lines illustrate the fit of two consecutive data points with independent exponential decays.

Chapter 4

Under-ice turbulence in the MIZ

4.1 Introduction to turbulence

4.1.1 About turbulent flows

Turbulent flows are characterised by their unsteadiness, their irregularity, their non-linearity and their chaotic behaviour. In the oceanic boundary layer, these properties make them key components of wind, wave and current energy dissipation, and of the transport and mixing of numerous quantities such like temperature and salinity. The characterization of the turbulence of a flow is done by calculating the Reynolds number, $\mathrm{Re} = UL/\nu$, where L is the characteristic size of the flow, U is the characteristic velocity of the flow, and ν is the kinematic viscosity of the fluid. A large Re number means that the flow is turbulent, while a low Re number means that the flow is laminar. The frontier between the two is not fixed, and depends in general on the flow properties.

To study turbulent flows, the velocity $u(\mathbf{x}, t)$ of the flow, in space $\mathbf{x} = (x, y, z)$ and time t, is often decomposed following Reynolds decomposition,

$$u(\mathbf{x}, t) = \bar{u}(\mathbf{x}, t) + u'(\mathbf{x}, t), \tag{4.1}$$

where $\bar{u}$ is the ensemble average of u, and u' is the fluctuating part of u, i.e. the velocity of the turbulent eddies. Applying the velocity decomposition to the Navier Stokes equations of the flow, the Reynolds Average Navier Stokes equations for the turbulent flow in the boundary layer are (using Einstein notation),

$$\rho_w \left[\underbrace{\frac{\partial \bar{u}_i}{\partial t}}_{\text{time dependence}} + \underbrace{\bar{u_j} \frac{\partial \bar{u}_i}{\partial x_j}}_{\text{advection}} \right] = \frac{\partial}{\partial x_j} \left[\underbrace{\mu_w \left(\frac{\partial \bar{u}_i}{\partial x_j} + \frac{\partial \bar{u_j}}{\partial x_i} \right)}_{\text{viscous stress}} \underbrace{-\bar{p}\delta_{ij}}_{\substack{\text{isotropic} \\ \text{pressure stress}}} \underbrace{-\rho_w \overline{u_i' u_j'}}_{\text{Reynolds stress}} \right] \tag{4.2}$$

$$\frac{\partial \bar{u}_i}{\partial x_i} = \frac{\partial u_i'}{\partial x_i} = 0. \tag{4.3}$$

with ρ_w the sea water density and μ_w the sea water dynamic viscosity. In the momentum equations, the Coriolis force has been neglected due to the scales considered in this work and the buoyancy force has been neglected since the flow in the boundary layer under

the ice is well mixed. This set of equations is not solvable since there are more unknowns than equations, due to the additional term called the 'Reynolds stress' τ, representing the stress induced by the turbulent fluctuating velocity field.

The eddy viscosity hypothesis, used by part of the wave-in-ice modeling community, is an attempt to close the set of Equations 4.2 and 4.3. It is based on the assumption that turbulent eddies are small compared to the overall scale of the flow. This assumption allows the eddies to be treated as "local" features of the flow that can be modeled using a local effective viscosity. In that case, the Reynolds stress can be rewritten in the same way as the viscous stress, with the so-called eddy viscosity ν_t in place of the kinematic viscosity of the fluid $\nu_w = \mu_w/\rho_w$:

$$\tau = \rho_w \nu_t \left(\frac{\partial \bar{u}_i}{\partial x_j} + \frac{\partial \bar{u}_j}{\partial x_i} \right). \tag{4.4}$$

Determining the value of the eddy viscosity parameter is difficult, as it is not directly observable in the field. Instead, the value of this parameter is typically tuned to match observations of wave attenuation in sea ice, assuming that all of the turbulence of the flow is generated in the boundary layer just under the ice by the shear between the wave orbital velocity and the ice. This is done by comparing model predictions with available measurements of wave attenuation and adjusting the eddy viscosity parameter until the model matches the observations. While this approach can provide a reasonable fit to the available data, there are several limitations and uncertainties associated with it. One important limitation is that the eddy viscosity parameter may hide the impact of other turbulence sources due to wave-ice interactions, as introduced in Chapter 1 (+ see Fig. 4.6), or even conceal other sources of wave attenuation than turbulence, that are not included in the model. Additionally, the tuned value of the eddy viscosity parameter may depend on the very specific conditions encountered and may not be applicable to a broader parameter space with very different ice and/or waves conditions. Therefore, direct measurements of under ice turbulence is required to get a better understanding of 1) how much wave energy is really dissipated due to turbulence generated from wave-ice interactions, and 2) the sources of under-ice turbulence.

4.1.2 Turbulent boundary layer flows

The turbulent quantity that is considered to study the energy of the flow relative to its turbulence is the Turbulent Kinetic Energy (TKE), $q^2 = \frac{1}{2}(\overline{u_i' u_i'})$, which is proportional to the trace of Reynolds stress tensor. The Turbulent Kinetic Energy (TKE) verifies a transport equation,

$$\frac{\partial q^2}{\partial t} = -\nabla T + P - \epsilon, \tag{4.5}$$

where $\nabla T = \frac{1}{2}\frac{\partial \overline{u_i' u_i' u_j'}}{\partial x_j} + \frac{1}{\rho}\frac{\partial \overline{p' u_j'}}{\partial x_j}$ is the turbulent transport, $P = -\overline{u_i' u_j'}\frac{\partial \bar{u}_i}{\partial x_j}$ is the production of TKE, and $\epsilon = \nu_w \overline{\frac{\partial u_i'}{\partial x_j}\frac{\partial u_i'}{\partial x_j}}$ is the TKE dissipation rate.

The turbulent flows I studied for this thesis are part of the boundary layer flows, which are flows in the vicinity of an interface (here, the interface between the wavy flow and the ice). In this case, the assumption is often made that the flow is statistically homogeneous, in the horizontal plane, with a mean velocity $\bar{u}(z,t)$ in the direction x, only depending on the vertical dimension z. Therefore, there are no spatial gradients in any averaged quantity ($\nabla T = 0$) except for $\bar{u}$ (pure shear flow). The velocity fluctuations are all non zero, and denoted thereafter u' in the direction of the mean flow, v' in the horizontal direction perpendicular to the mean flow, and w' in the vertical direction. In addition, the flow is also considered locally steady, which means that ($\frac{\partial q^2}{\partial t} = 0$). The TKE equation becomes then a balance between TKE production and TKE dissipation:

$$P = -\overline{u'w'}\frac{\partial \bar{u}}{\partial z} \approx \epsilon. \tag{4.6}$$

In the boundary layer, since the Reynolds shear stress has to match the stress exerted by the flow on the boundary, it is often written in terms of a friction (or shear) velocity $u^{*2} = -\overline{u'w'} = \tau/\rho_w$. Under the assumption of homogeneous turbulence in the boundary layer, this friction velocity is supposed to be constant. In addition, using Prandtl's mixing length model, the vertical velocity gradients scale as:

$$\frac{\partial \bar{u}}{\partial z} = \frac{u^*}{\kappa z}, \tag{4.7}$$

where z is the distance to the boundary, and $\kappa = 0.41$ is the von Karmán constant, estimated experimentally. This equation is called the "law of the wall". Mainly, the wall layer theory assumes that the turbulence in the boundary layer is solely a function of the flow conditions at the wall and is independent of the flow conditions further away from the wall. It can be noticed that, by multiplying the equation 4.7 by u^*, this equation is equivalent to the turbulent viscosity model with $\nu_t = u^* \kappa z$. When combining equations 4.6 and 4.7 with the definition of the friction velocity, it gives the law of the wall for the TKE dissipation rate:

$$\epsilon(z) = \frac{u^{*3}}{\kappa z}. \tag{4.8}$$

Thus, to derive the profile of $\epsilon(z)$ in the boundary layer, only the friction velocity has to be estimated.

The space interval of validity of the law of the wall is generally described using the

dimensionless variable $z^+ = \frac{u^* z}{\nu_w}$, such that (Pope, 2000, p. 276,):

$$\begin{aligned} z^+ &\geq 10 \\ z^+ &\leq 1000 \end{aligned} \tag{4.9}$$

The oceanic boundary layers encountered in this work, ocean-ice and ocean-sea bottom, are discussed in the framework of the sea bottom boundary layer (Soulsby, 1997). The flows in these boundary layers are driven by two sources: the ocean waves and the current. Two different sources means two different representative velocities, and therefore two different Reynolds numbers.

For waves only, the Reynolds number $\mathrm{Re_w}$ is based on the RMS orbital velocity of the waves, U_{orb}, and their semi-orbital excursion, $A_{\mathrm{orb}} = \frac{U_{\mathrm{orb}} T}{2\pi}$, where T is the wave period, i.e.

$$\mathrm{Re_w} = \frac{U_{\mathrm{orb}}^2 T}{2\pi\nu_w}. \tag{4.10}$$

The flow generated by the waves at the boundary layer is considered turbulent if $\mathrm{Re_w} > \mathrm{Re_{w,cr}}$. The value of the critical Reynolds number for the waves, $\mathrm{Re_{w,cr}}$, changes depending on the nature of the boundary layer. According to Soulsby (1997), for sea bottom boundary layer, $\mathrm{Re_{w,cr}} = 5 \times 10^5$.

For the current only, the Reynolds number $\mathrm{Re_c}$ is based on the water depth, D_h, and the depth-averaged current velocity, $\overline{U_{\mathrm{cur}}}$, defined as

$$\overline{U_{\mathrm{cur}}} = \frac{1}{D_h} \int_{z_0}^{D_h} U_{\mathrm{cur}}(z) dz, \tag{4.11}$$

where $U_{\mathrm{cur}}(z)$ is the current depth profile, and z_0 is the boundary roughness length, which gives

$$\mathrm{Re_c} = \frac{\overline{U_{\mathrm{cur}}} D_h}{\nu_w}. \tag{4.12}$$

The flow generated by the current at the boundary layer is considered turbulent for $\mathrm{Re_c}$ larger than the critical Reynolds number $\mathrm{Re_{c,cr}} = 2000$.

When waves and current happen in the same time, the turbulence of the flow resulting of the two phenomena starts when at least one of the two critical Reynolds numbers is reached, i.e. when $\mathrm{Re_w} > \mathrm{Re_{w,cr}}$ and/or $\mathrm{Re_c} > \mathrm{Re_{c,cr}}$. In this case, the critical Reynolds number for the current is modified (Soulsby, 1997):

$$\mathrm{Re_{c,cr}} = 2000 + (5.92 \times 10^5 \times \mathrm{Re_w})^{0.35}. \tag{4.13}$$

Interactions between the waves and the current are then known to result in a complex wave-plus-current turbulent stress at the boundary layer. The computation of such shear stress is out of the scope of this work.

The friction velocities of the turbulent current and wave flows separately are often proportional to the representative velocity of the considered phenomenon (Soulsby, 1997), i.e.

$$u_w^* = \sqrt{C_{\mathrm{Dw}}} U_{\mathrm{orb}} \tag{4.14}$$

and

$$u_c^* = \sqrt{C_{\mathrm{Dc}}} \overline{U_{\mathrm{cur}}}. \tag{4.15}$$

C_{Dw} and C_{Dc} are respectively the wave and current drag coefficients. They depend on flow and boundary layer properties.

Substituting these friction velocities in Eq. 4.8 allows to express the TKE dissipation rate as a function of each representative velocity and drag coefficient:

$$\epsilon_w = C_{\mathrm{Dw}}^{3/2} \frac{U_{\mathrm{orb}}^3}{\kappa z} \tag{4.16}$$

and

$$\epsilon_c = C_{\mathrm{Dc}}^{3/2} \frac{\overline{U_{\mathrm{cur}}}^3}{\kappa z}. \tag{4.17}$$

4.1.3 Energy dissipation from turbulence

According to Kolmogorov (1991), in a turbulent flow, energy is transferred from the large-scale eddies to smaller and smaller scales until it is dissipated into heat through the viscous forces acting at the smallest scales. One of the key insights of Kolmogorov's theory is the idea of the inertial subrange, which is the range of scales between the energy injection scale and the viscous dissipation scale. In this subrange, the flow is characterized by a self-similar cascade of energy, where larger eddies transfer their kinetic energy to smaller eddies through a series of nonlinear interactions. This cascade continues until the energy is dissipated at the smallest scales by viscous forces. The rate at which energy is dissipated in the inertial subrange is related to the velocity u_s and length scale l_s of the turbulent eddies, following

$$\epsilon = \frac{u_s^3}{l_s}. \tag{4.18}$$

Several methods follow from this theory for estimating the value of ϵ from measured properties of the flow. Among them, the one I used is based on the calculation of the centered second order structure functions:

$$D(r, dr, \bar{t}) = \overline{[u'(r - dr/2, t) - u'(r + dr/2, t)]^2}. \tag{4.19}$$

D represents the correlations at location r, and around averaged time $\bar{t}$, between the velocity of turbulent eddies separated by a distance $dr/2$ on each side of r. For dr within the inertial subrange, provided that the flow is stationary around $\bar{t}$, locally homogeneous

and isotropic, Kolmogorov (1991) showed that

$$D(r, dr, \bar{t}) = C_0 \epsilon(r, \bar{t})^{2/3} dr^{2/3} \tag{4.20}$$

where $C_0 = 2.0 \pm 0.1$ is a constant (Saddoughi and Veeravalli, 1994). Thus, ϵ can be computed from a fit of the $dr^{2/3}$ spatial evolution of D. The strength of this method is that it can deal with missing data points, which are common in experimental science. Yet, it requires measurements at several locations dr from each data point r to compute ϵ.

Another method to estimate ϵ, that is widely used by the turbulence community, is from the wave number (k) TKE spectrum $S(k)$, which is such that:

$$q^2 = \int_0^\infty S(k) dk. \tag{4.21}$$

Applying a Fourier transform to Eq. 4.20, under the same constraints of stationarity, homogeneity and isotropy, and within the inertial range, this spectrum follows the relation:

$$S(k) = C_k \epsilon^{2/3} k^{-5/3}, \tag{4.22}$$

where $C_k = 0.5$ is a constant (Sreenivasan, 1995). Thus, ϵ can be computed from a fit of the $k^{-5/3}$ spatial evolution of $S(k)$ in the inertial subrange. Since many turbulence measurements are made in one location, with only time variation, the Taylor frozen turbulence hypothesis, that states that the advection of a turbulent eddy past a fixed point is entirely due to the mean flow (and not to the turbulence), is often considered to compute ϵ from the frequency TKE spectrum. However, $S(k)$ is difficult to compute from data with missing points, often implying that some interpolation has to be applied in that very current case, that might add erroneous information to the spectrum.

Both methods have their benefits and their drawbacks, and I choose to work with the first one according to them. Indeed, as described below, the measurements are made both in space and time, allowing to compute second order structure functions, and the data contains missing data points after quality control, for which this method is more robust. Furthermore, Taylor's hypothesis is not needed for the second order structure function method. There is another non trivial point that confirmed this choice. In this work, the flow considered is unsteady due to the wave signal. This unsteadiness appears as a large bump in the TKE spectrum, impinging on most of the inertial subrange available from the measurements, and globally increasing the values of $S(k)$. Even though methods exist to remove the unsteady turbulence advection by the waves from the TKE spectrum (Gerbi, 2008), these were not sufficient to entirely remove the effect of the waves, which lead to large (several orders of magnitude) overestimation of the TKE dissipation rate. Waves also affect the second-order structure function method, but methods have been developed to effectively remove wave contamination from their estimate of wave contam-

ination (Scannell et al., 2017). These techniques are discussed and tested in the analyses below.

4.2 Measuring turbulence under the ice

Under-ice turbulence was estimated using ADCPs in pulse-coherent mode, also called Pulse Coherent Acoustic Doppler Profilers (PCADPs). The pulse-coherent mode works as follows (Lacy and Sherwood, 2004):

- Two acoustic pulses are emitted successively from the device along a beam of fixed direction, with a fixed time interval in between, and the same phase at the origin.
- The first signal is reflected off the particles suspended in the water, whose velocity is assumed to be similar to that of the fluid.
- The second signal is reflected off the same particles, but after they have moved slightly due to their velocity.
- Thus, when the second signal reaches back the device, it is out of phase with the first signal.
- The speed of the fluid is deduced from this phase shift.

The regular Doppler mode is also used when available:

- A single pulse of frequency f_{aq} is emitted from the device, along a beam of fixed direction.
- It is reflected off the particles suspended in the water, whose velocity is assumed to be similar to that of the fluid.
- After the reflection, the frequency of the pulse has been increased if the particles were going towards the device, and decreased in the opposite situation, due to the Doppler effect.
- The speed of the fluid is deduced from this frequency shift.

Whether it be for the Doppler or the pulse coherent mode, the process is repeated at a very high frequency, forming a "burst" of data, and is then averaged over a much lower sampling frequency, forming a "ping" of data.

In 2017, 2018 and 2019, a single Nortek Aquadopp HR Profiler was used. It is composed of one beam looking vertically downwards and two beams looking horizontally with 90° between each beam (see Fig. 4.1.b). In 2020, two upward-looking Nortek Signature 1000 (S1000) ADCPs were used instead. They consist in one vertical beam looking upwards, and four slanted beams with an angle of 25° with respect to the vertical beam, and an angle of 90° with respect to each other (Janus configuration, see Fig. 4.1.a). The vertical beam works in pulse-coherent mode (HR for High Resolution), whereas the slanted beams work in Doppler mode.

The devices were deployed within the buoy deployment line, directly adjacent to one of the SKIBs. A hole was drilled inside an ice floe to insert the ADCP in the water column

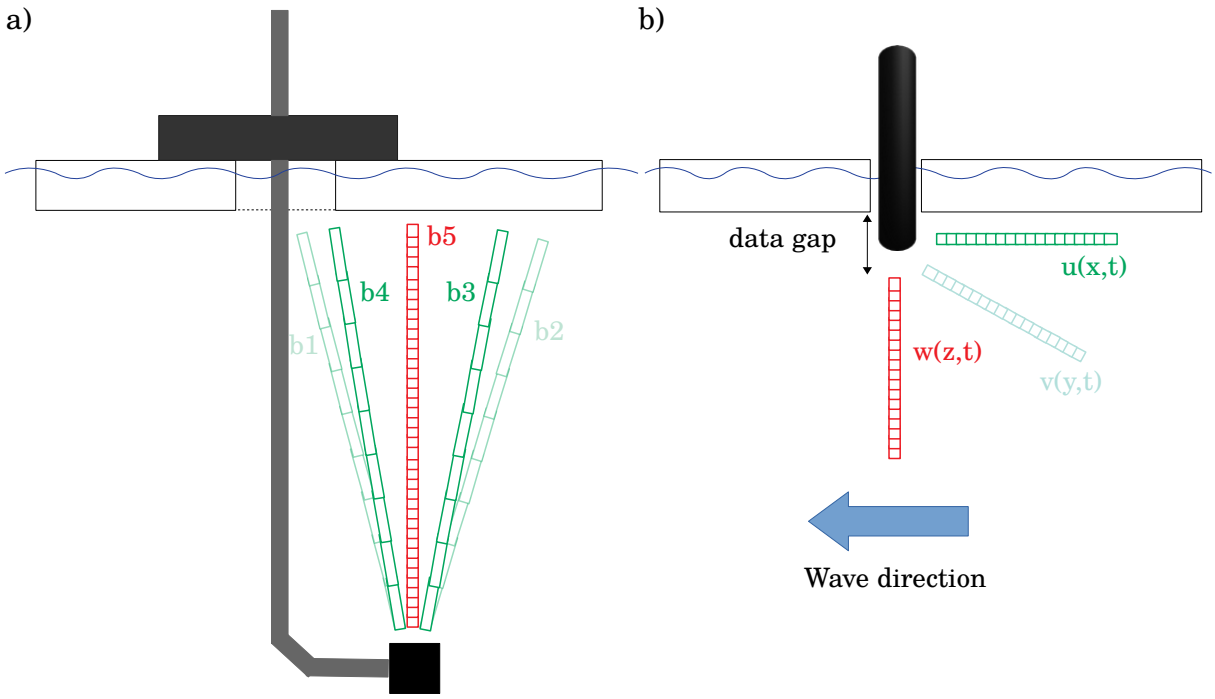

Figure 4.1 – Schematic of a) S1000 and b) Aquadopp when deployed within a hole in an ice floe.

under the ice. The Aquadopp was inserted directly in the hole as in Fig. 4.1.b. The S1000s were mounted on a mast, as in Fig. 4.1.a, so that their beams were facing the base of the ice. They were placed upstream (in the wave direction) of the hole in the ice and the mast to avoid measuring turbulence induced by their presence. The size of the space discretization, called "bin", is chosen as a compromise between fine space resolution and a size large enough to reduce the noise. The maximum range of the beams is chosen as long as possible, yet not too long to avoid getting a too low ambiguity velocity (see Eq. 4.23 below). As a result, for the Aquadopp, vertical velocity fluctuations were measured at 2 MHz and sampled at 4 Hz, within 2.2 cm bins, ranging from 0.3 m to down to 1.30 m under the ice base. For the S1000s, vertical velocity fluctuations were measured at 1 MHz and sampled at 8 Hz, within 2 cm bins, ranging from 2.40 to up to 0 m under the ice for one of the devices (s497), and from 1.40 to up to 0 m under the ice for the other one (s489). This range was modified in some cases depending on the ice thickness.

4.3 Turbulence data processing

The energy dissipation due to turbulent processes in the water column under the ice is estimated by computing the TKE dissipation rate ϵ using the vertical velocities measured with the vertical beams of the ADCPs. Theses velocities are measured in the reference frame of the ice, meaning that, unlike the Galilean reference frame, where the

velocities reach a maximum at the sea surface, here the velocities reach a minimum at the interface between the ice and the ocean, and a maximum below. Fig. 4.2 shows an example of PCADP data, using the upward-looking s497 during day 2020-02-25. The amplitude of the back-scattered signal decreases slightly with the distance to the device (from 75 close to the device to 60 close to the ice, on average) as expected, since part of the signal is scattered along the way. It locally increases when the signal meets scatterers like organic materials, ice crystals or patches of slush, which appear as tiny orange spots over the yellow to green background. When meeting the ice surface, the remaining energy is reflected, leading to the orange band (high backscatter) on top of the plot ($X_{\mathrm{B5}} = 2.4$ m). The correlation gives an estimate of the quality of the velocity measurement. In addition to a slight increase at the location of the ice edge, a remarkable feature of panel b) is the low correlation band between $X_{\mathrm{B5}} = 2.2$ m and $X_{\mathrm{B5}} = 2.3$ m, which is noise due to the reflection of the signal off the ice.

To remove low quality data while avoiding information loss, data with correlation $< c = 50$ % and backscatter amplitude $< a = 30$ counts out of 150 were masked for the analysis (Rusello, 2009; Thomson, 2012). These threshold values have been compared to both higher and lower thresholds, as summarized in Fig. 4.3. The TKE dissipation rate ϵ is computed, following Wiles et al. (2006) as discussed in the data analysis below, for each couple (c, a), and compared to the reference TKE dissipation rate ϵ_{ref} computed for $c = 50$ and $a = 30$. The comparison is done by subtracting $\log(\epsilon_{ref})$ to $\log(\epsilon)$, which is called thereafter 'TKE bias'. The correlation, amplitude, velocity and TKE dissipation rate fields relative to the time period plotted on Fig. 4.3 are visible on Fig. 4.2 for reference. The amplitude threshold has no impact on the TKE bias from $a = 30$ to $a = 0$, regardless of the correlation threshold, as seen between Fig. 4.3.e) and d). This is due to the fact that all of the data points of this sample have an amplitude over 30. However, increasing the amplitude threshold to over 50, in this specific case, lead to a significant loss of information. For $a = 55$ (e.g. Fig. 4.3.f), the TKE bias becomes much noisier, independently from the range, which means that relevant data is probably removed, leading for less points for the computation of $\epsilon(z)$. For $a > 60$ (not shown here), too much of the data is removed, resulting in an empty TKE dissipation field. The change in correlation threshold shows that decreasing the threshold to $c = 20$ (e.g. Fig. 4.3.b) adds TKE dissipation mainly close to the device and close to the ice, where the data is noisy. Yet, increasing the threshold to $c = 70$ (e.g. Fig. 4.3.i) adds noise to the TKE bias, independently of the range, which could mean as for a that relevant data starts to be removed. This analysis on the data quality does not aim to validate or invalidate the choice of the thresholds, but allows to visualize the locations where these thresholds have the more effect on the calculation of the TKE dissipation rate.

The velocity signal in Fig. 4.2 shows positive and negative velocities alternating as a function of time, with a period of approximately 3 s, which is the signature of the

wave orbital motion. Moreover, away from the ice, where the velocities are the highest, phase wrapping occurs in the form of velocity jumps, from positive high to negative high velocity (or the opposite). This is due to the pulse coherent mode, for which the velocity is a function of the phase shift between to successive pulses. Since the phase shift is bounded in $[-\pi, \pi]$, so is the velocity in $[-V_a/2, V_a/2]$ where V_a is called the velocity ambiguity. Following Lacy and Sherwood (2004), the ambiguity velocity V_a can be related to the maximum range $r_{\max}$ of PCADP in each case,

$$V_a r_{\max} = \frac{c^2}{4 f_{aq}}, \tag{4.23}$$

where c is the sound speed in sea water and f_{aq} is the acoustic frequency of the device. c is computed by the internal software of the device using the equation of state, with the prescribed salinity value of 28 psu (mean value from this region; Saucier et al., 2003), and the temperature measured by the heat sensor of the device, usually close to 0°C, leading to speeds around 1441.5 ± 0.5 m s^{-1}. For Aquadopp and S1000 devices, it leads to ambiguity velocities respectively close to 0.26 m s^{-1} and 0.20 m s^{-1} (varying with the sea water temperature), meaning that the maximum velocity that can be measured before the signal is wrapped is respectively around $v_{\max} = 0.13$ m s^{-1} and $v_{\max} = 0.10$ m s^{-1}.

For the S1000s, HR velocity data was unwrapped using first the Doppler measurements from the slanted beams, since they have a much higher ambiguity velocity. The Doppler velocities were processed by masking bad quality data as for HR velocities. Then, they were corrected from the motion of the S1000 the instrument movement measured by the built-in accelerometer, magnetometer and gyroscope. To count the number of times the HR velocity is wrapped, the wrapped HR velocity is subtracted from the processed Doppler velocity, and the result is divided by the ambiguity velocity and then rounded. The integer obtained is multiplied by the ambiguity velocity, and the resulting velocity is added to the HR velocity to unwrap it. Then, Matlab `unwrap` function (p. 13183, MathWorks®, 2020) was applied to correct for along beam jumps. The `unwrap` function assumes that the input signal has a periodic nature, and it works by adding multiples of 2π (replaced here by V_a) to the phase of each sample in the signal so that adjacent samples have a phase difference of less than π (replaced here by $V_a/2$). Last, the velocity data was again compared to the Doppler velocities to remove offsets introduced by the previous step. For the Aquadopp, the unwrapping of the data was done by using Matlab unwrapper only, in the absence of Doppler measurements for reference. Aquadopp data were first unwrapped along time and then along beam to remove offsets introduced by the first step.

There are two differences in Aquadopp data compared to S1000 data. The first one is that the Aquadopp was facing downwards, so there was no interface facing Aquadopp's vertical beam, and therefore no reflection interference. The second one is that, with the

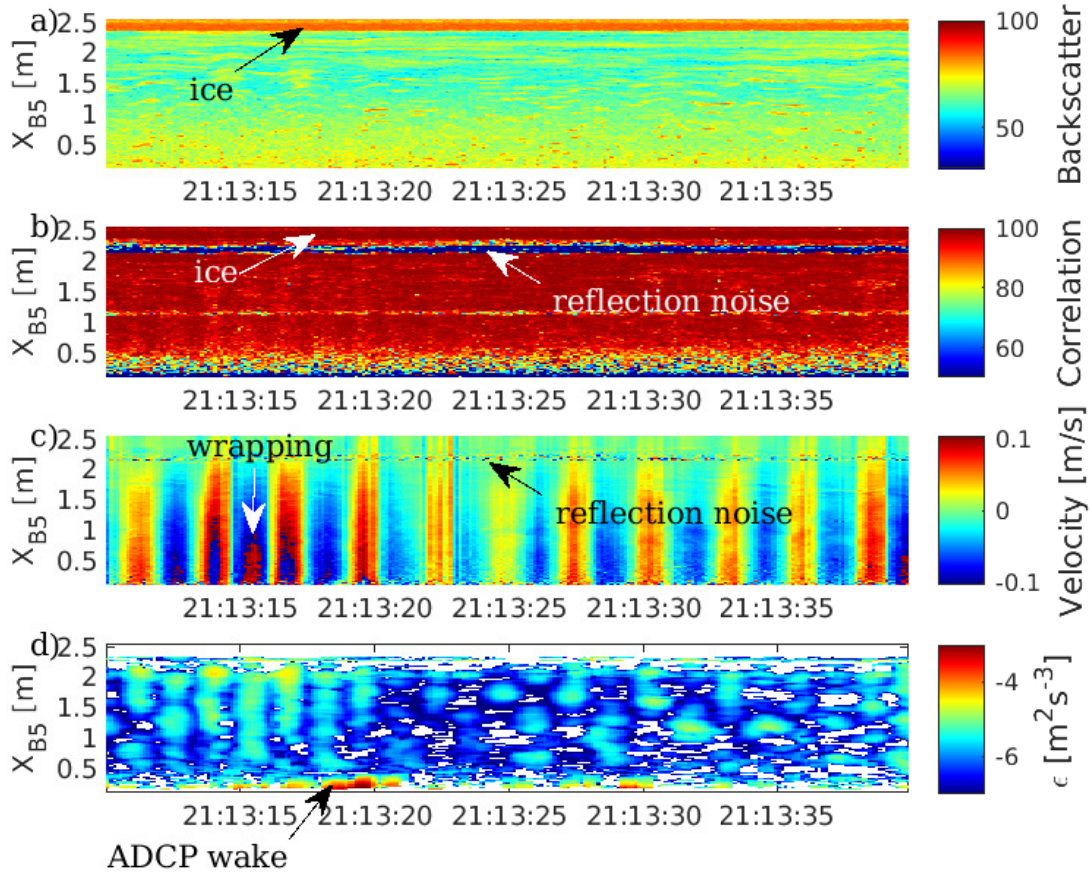

Figure 4.2 – a) Amplitude of the back-scattered signal in counts, b) statistical measurement of behaviour similarity between two received signals, called correlation, in %, c) raw vertical velocity of the flow under the ice in $m.s^{-1}$ and d) computed TKE dissipation rate in power of 10 $m^2.s^{-3}$, as a function of time and distance from the device, as measured by beam 5 of s497 on day 2020-02-25 between 21:13:10 and 21:13:40 UTC. Ice, reflection noise, phase wrapping and instrument wake are localised with arrows.

Aquadopp, there is only one velocity measurement cell 20 cm under the ice using the two horizontal beams (2 and 3), and then the measurements along beam 3 start at 30 cm from the ice, whereas S1000s allow measurement of velocity fluctuations directly beneath the ice. Otherwise, the processing and the analysis of the data acquired using Aquadopp and S1000 are similar.

4.4 Analysis of turbulence data

The second-order structure function method (Kolmogorov, 1991) is used to derive the TKE dissipation rate. The centred second-order structure function $D(r, dr, \bar{t})$ is given by Eq. 4.19. In the case of turbulence measurements using ADCPs, r is the along-beam range, dr is a multiple of twice the bin size and represents the separation distance between

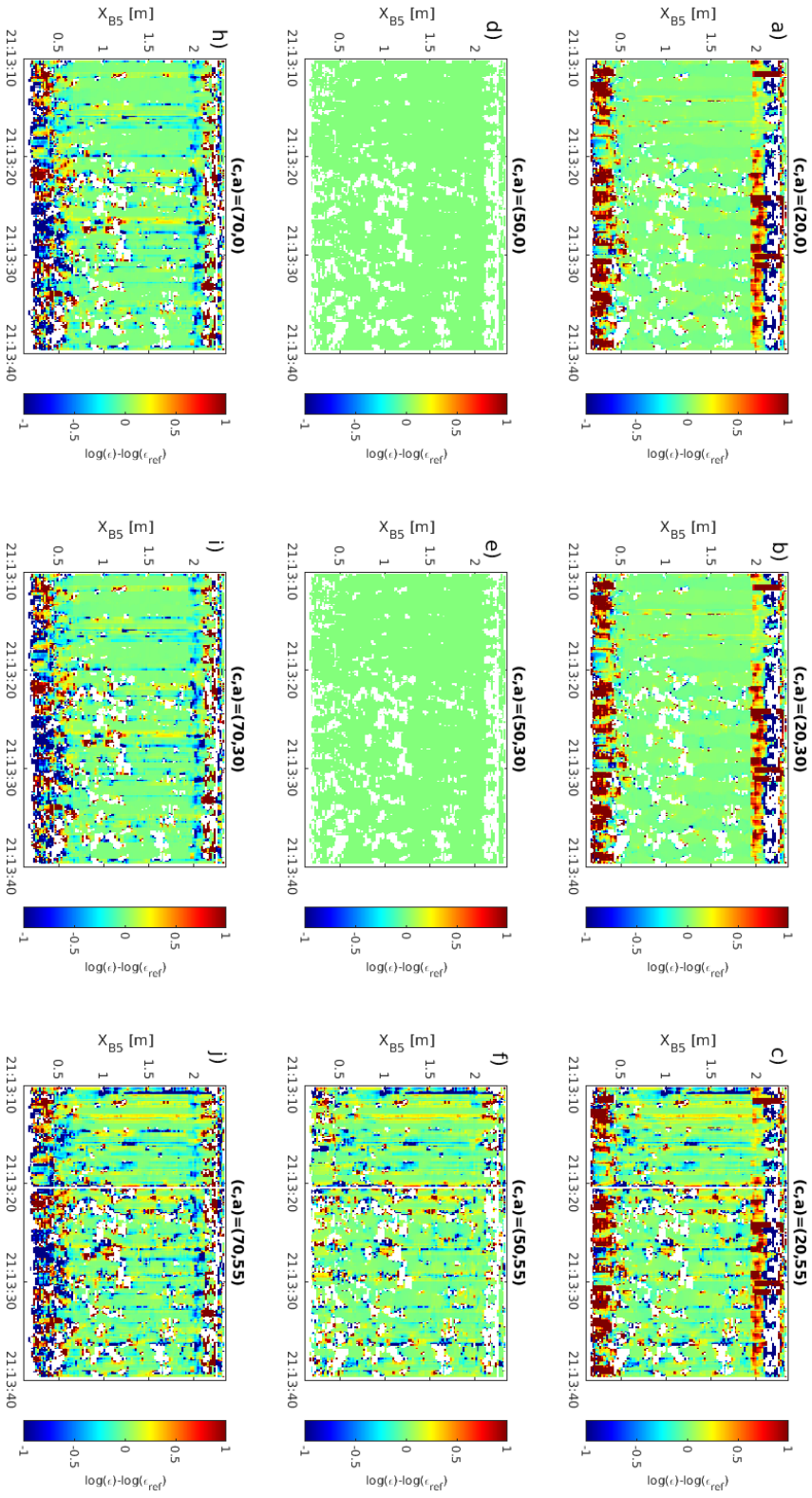

Figure 4.3 – Difference between the logarithm of the TKE dissipation rate with several values of correlation $c = [20; 50; 70]$ and amplitude $a = [0; 30; 55]$, and the logarithm of the TKE dissipation rate computed for reference values of correlation and amplitude ($c = 50$, $a = 30$), as functions of time and ADCP range X_{B5}. Measurements are made along beam 5 of s497 on day 2020-02-25 between 21:13:10 UTC and 21:13:40 UTC. The value of c and a used for each plot is shown in the titles.

correlated velocity bins on either sides of r, the overline is the average over 5 pings for S1000s, i.e. 0.625 s, and over 3 pings for the Aquadopp, i.e. 0.75 s, around time $\bar{t}$, and t is the instantaneous time. These durations were chosen to be much shorter than the wave period (≥ 3 s). The maximum distance for velocity correlation between bins is set to $dr_{\max} = 0.4$ m (Gemmrich and Farmer, 2004). Thus, the structure functions are computed on $dr_{\max}/(2 \text{ bin size}) = 10$ bins for the S1000s (9 for the Aquadopp) on either sides of r for most of the range. At the edges of the velocity profiles (e.g. $r < dr_{\max}/2$), where $dr/2$ is limited by the distance to the edge, the structure functions are computed on fewer bins, and therefore more sensitive to noise and more likely to result in a bad fit (see below).

ADCPs have inherent Doppler noise, which varies depending on the hardware of the instrument and from flow conditions. This noise is often considered white, and has been accounted for by Wiles et al. (2006) in the structure function method as:

$$D(r, dr, \bar{t}) = N(r, \bar{t}) + A(r, \bar{t}) dr^{2/3}, \tag{4.24}$$

where $N(r, \bar{t})$ is the contribution from Doppler noise and $A(r, \bar{t}) = C\epsilon^{2/3}$ the one from turbulent velocity fluctuations. In addition, as alluded to in the introductory part of this Chapter, the wave unsteady signal also contaminates the structure function due to the vertical gradients of the wave orbital velocities. Therefore, including the contribution of both the noise and the waves to the measured structure functions, following Scannell et al. (2017), gives:

$$D(r, dr, \bar{t}) = N(r, \bar{t}) + A(r, \bar{t}) dr^{2/3} + B(r, \bar{t}) dr^2, \tag{4.25}$$

where $B(r, \bar{t})$ is the effect of the waves. This second method is based on the hypothesis that the length scales of turbulence and wave orbital motion are well separated, which is discussed below. In this work, N and A, or N, A and B are obtained from a non-negative least-square fit of D, using the Matlab function `lsqnonneg` (MathWorks®, 2020, p.7295). The TKE dissipation rate in the water column is then deduced from $A(r, \bar{t})$:

$$\epsilon(r, \bar{t}) = \left(\frac{A(r, \bar{t})}{C} \right)^{3/2}. \tag{4.26}$$

Panel d) of Fig. 4.2 shows that the turbulence is stronger when more intense wave packets are propagated under the ice (around 21:13:15 UTC). Patches of high TKE dissipation rate are also observed close to the instrument (at 21:13:20 UTC), due to its wake. White patches are points where the structure function could not be fitted with the non-negative constraint on N, A and B, or points where the correlation and/or amplitude were below the quality thresholds. The occurrence of such patches seem to be partly correlated with the presence of suspended particles (ice or organic material) of size larger than the bin size, appearing as points of increased backscatter compared to the back-ground level. However, that relation has not been quantified.

For consistency with wave analysis time interval, and for the same reasons (ensure stationarity while capturing the dynamics), $\epsilon(r, \bar{t})$ is averaged over the same 10-min segment as for wave buoy data. Fig. 4.4 presents example profiles of TKE dissipation rate during T1 and T2. Both Wiles et al. (2006) and Scannell et al. (2017) methods are plotted for comparison. The values of ϵ are lower when computed using Scannell et al. (2017) method than when using Wiles et al. (2006) method. It is due to the fact that Scannell et al. (2017) method removes the contribution of the waves to D, assuming that the wave orbital motion and the turbulence do not interact. Yet, according to Scannell et al. (2017), this modified method tends to produce an underestimation of the TKE dissipation rate in case of short wavelength and shallow water depth, which are both conditions observed in this work. Using the modified method here would thus remove too much signal in D, and in a non-linear way with depth, also modifying the profile of ϵ. Therefore, I decided to use Wiles et al. (2006) method as a reference to compute the TKE dissipation rate, and I kept Scannell et al. (2017) method to compute an estimate of the lower bound.

Instrument wake and edges effect on ϵ are discarded from the data. The remaining data is fitted with a linear least square fit of $\log(\epsilon(z))$ with respect to $\log(z)$ (e.g. $\epsilon(z)$ computed using Wiles et al. (2006) method during T2 on Fig. 4.4). The fit is considered valid when the R-squared is larger than 0.5 (value experimentally chosen). This kind of profile is observed in all the data sets, but not at each time interval, as seen from Fig. 4.4. Otherwise, the remaining data is compared to a constant value, computed as the average of $\epsilon(z)$ (e.g. other cases on Fig. 4.4). In practice, the R-squared of the fit is either above ~ 0.5, or very close to 0, which makes a rather clear separation between the cases. These comparisons are used below to extend the data outside the valid data range, and to discuss the phenomena inducing under-ice turbulence.

4.5 Total TKE dissipation rate

The total TKE dissipation rate per unit of sea surface Γ_t is estimated by integrating the vertical profile of the TKE dissipation rate over the water column under the ice

$$\Gamma_\mathrm{t}(x_\mathrm{ice}) = \rho_w \int_{z_\mathrm{max}}^{z_\mathrm{min}} \epsilon(z, x_\mathrm{ice}) dz. \tag{4.27}$$

To compute a reference value for Γ_t using Eq. 4.27, z_min and z_max are imposed by the range over which the TKE dissipation measurement is considered valid, after throwing out bad data. This range varies depending on the ADCP used and on the wave conditions (e.g. stronger waves mean higher wake effect close to the device). Thereafter, in Fig. 4.5 and 5.6, it is this value that is represented as a data point.

To extend Γ_t outside this interval, wider values $z_\mathrm{min,ex}$ and $z_\mathrm{max,ex}$ are computed, according to the turbulent boundary layer theory, based on the interval over which the law

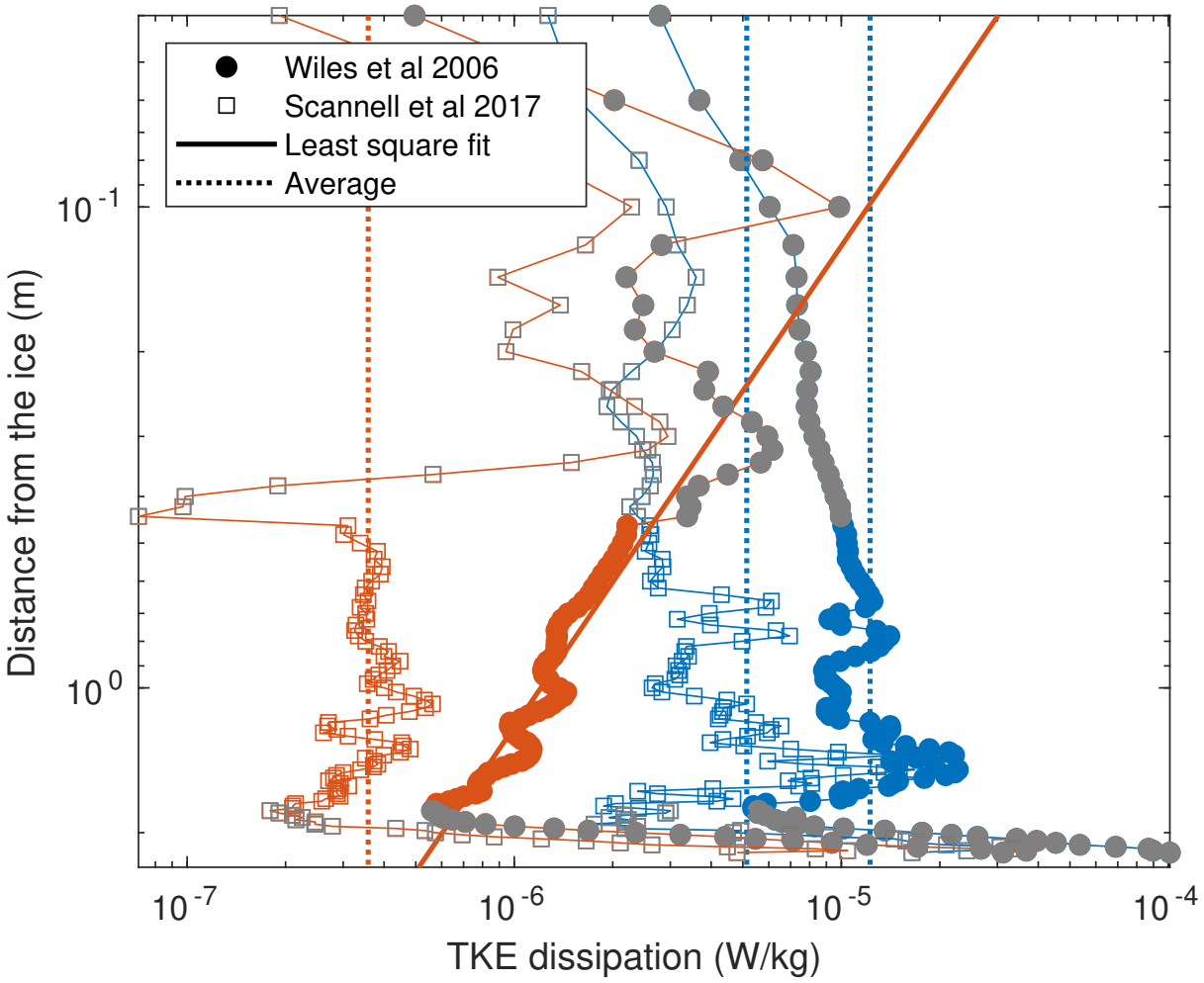

Figure 4.4 – TKE dissipation as a function of vertical distance to the ice, 2020-02-25. The dots are TKE dissipation rate estimated following Wiles et al. (2006). The squares are TKE dissipation rate estimated following Scannell et al. (2017). The solid line represents the least square fit of data following the "law of the wall". The dashed lines are average of the data not following the "law of the wall". The blue color is relative to a 10-min time interval during T1 (19:00-20:30 UTC) and the orange color is relative to a 10-min time interval during T2 (20:30-21:30 UTC). The grey dots and squares are discarded data due to instrument wake effect and edge effect.

of the wall applies (see Eq. 4.9). In this framework, the distance to the wall is scaled using the friction velocity of the waves, u_w^*, and the kinematic viscosity of the fluid, $\nu_w = 2 \times 10^{-6}$ m^2.s^{-1} (for sea water at temperature -2 ° C and salinity 28 psu). An order of magnitude of the wave friction velocity, $u_w^* = 1 \times 10^{-3}$ m.s^{-1}, is estimated using the data of 2020 with the slanted beams of the S1000. Thus, $z_{\text{min,ex}} \simeq 0.02$ m and $z_{\text{max,ex}} \simeq 2$ m. It should be noted that these values are also consistent with the largest range of the ADCPs, namely the one of S497. For consistency, and without better alternative, the depth range computed in the case of the "law of the wall" is also used when $\epsilon(z)$ is following a constant profile with depth. Extending the data in both cases leads to an increase in Γ_t from 10 to 50 % for S497 and S489 data to up to one order of magnitude for Aquadopp data. In Fig. 4.5, this increase is accounted for in the error bars in term of positive error.

The Wiles et al. (2006) model is used to compute a reference value of the total TKE dissipation rate, for the reasons explained above. Using Scannell et al. (2017) model produces values between 50 and 10 % of the total TKE dissipation rate computed using Wiles et al. (2006) model. This decrease is not accounted for in the error bars of Fig. 4.5 since the values obtained are regularly lower than the physical errors discussed below. Nevertheless, it gives an idea of the minimum values expected for Γ_t.

In the data analysis, no assumption were made about the source(s) of the under-ice turbulence. However, the value of Γ_t of interest for this study needs to only involve turbulence due to wave-ice interactions, to be able to discuss about the sources of wave attenuation under sea ice. Other possible sources of under-ice turbulence in the ocean water column include sea bottom friction due to waves and currents, current friction on the ice, and upper-ocean processes like wind driven shear, wave breaking and Langmuir circulations. The latter three are not involved in our cases since the ice cover prevented the occurrence of such processes. Moreover, the wave friction on sea bottom has been shown to be non turbulent in Chapter 3, after comparing the wave turbulent stress to the wave laminar stress on the sea bottom, so it is not suspected to add turbulence under the ice. As discussed in Sutherland and Dumont (2018), the tidal range of 4 m and the strong tidal currents in the LSLE affect both wave propagation and current stress on the ice cover in the studied MIZs . Due to the shallow bathymetry at some locations in BdHH and RB, turbulent sea bottom friction by current can increase the turbulence level up to just under the ice. In addition, turbulent current friction on the ice happens at the right place to be measured by the ADCPs. Therefore, both current friction on sea bottom and current friction on the ice are discussed for the calculation of Γ_t, as two additional sources of error.

In what follows, the sources of under-ice turbulence are treated as if they were not interacting, i.e. as if the measured TKE dissipation rate was equal to the sum of the TKE dissipation rates of each sources computed separately. This work does not address the coupling between these sources, which may lead to more or less turbulence under the ice.

The turbulent friction of the current on the sea bottom and on the ice can be both treated in the same framework, as introduced in this Chapter, using Eq. 4.17, with the depth-averaged current velocity $\overline{U_{\mathrm{cur}}}$, and a specific drag coefficient for each interface, sea bottom-ocean and ocean-ice. The current velocity profile was only measured for cases of 2020, using the slanted beams of the S1000s. To that purpose, the velocities from the slanted beams where corrected from the motion of the S1000 using the instrument movement measured by the built-in accelerometer, magnetometer and gyroscope, and put in the East North Up reference frame using the rotation matrix provided by the software of the instrument. Then the mean current velocity depth profile is computed,

$$U_{\mathrm{cur}} = \sqrt{\overline{u_{\mathrm{E}}}(z)^2 + \overline{u_{\mathrm{N}}}(z)^2}, \tag{4.28}$$

where $\overline{u_{\mathrm{E}}}$ and $\overline{u_{\mathrm{N}}}$ are the current velocity in the East and North directions, averaged over each 10-minutes intervals to remove the contribution of the waves. The depth-averaged current velocity cannot exactly be computed from these measurements using Eq. 4.11 since the range of the ADCPs never covers the full depth under the ice. Thus, the range-averaged current is computed instead, over the range $\Delta z_r = z_{\max} - z_{\min}$, and in the direction of the current:

$$\overline{U_{\mathrm{cur}}} = \frac{1}{\Delta z_r} \int_{z_{\min}}^{z_{\max}} U_{\mathrm{cur}}(z) dz. \tag{4.29}$$

For the three deployment days of 2020, the range-averaged current under the ice is between 0.05 and 0.12 m.s^{-1} at the ADCP the closest to the ice edge, and between 0.01 and 0.1 m.s^{-1} at the ADCP the farthest away from the ice edge. The variation in current intensity at any measurement location is correlated to the phase and the amplitude of the tide. For the other deployment years, mean current velocities between 0.1 and 0.2 m.s^{-1} are used, depending on the phase of the tide, following the reference Particle Image Velocimetry (PIV) measurements in Appendix B of Sutherland and Dumont (2018). The tide phase $\varphi_{\mathrm{tide}}(t)$ is retrieved from the Hilbert transform H of the tide elevation $\eta_{\mathrm{tide}}(t)$ as:

$$\varphi_{\mathrm{tide}}(t) = \arctan \frac{\Im[H(\eta_{\mathrm{tide}}(t))]}{\Re[H(\eta_{\mathrm{tide}}(t))]}. \tag{4.30}$$

The mean current velocity for a 10-minutes time interval is then obtained as the mean of the different PIV data sets at the corresponding tide phase . Taking the overall smaller current velocity (0.01 m.s^{-1}) and the shallowest depth (2.4 m) gives the minimum Reynolds number due to the current, $\mathrm{Re_c} > 1.2 \times 10^4$ (Eq. 4.12), which is much larger than the critical Reynolds number for the current to be turbulent, $\mathrm{Re_{c,cr}} \simeq 5 \times 10^3$ for $\mathrm{Re_w} = 10^4$ (which is the upper bound of the wave Reynolds number computed in this work). This means that current friction has to be considered for each deployment at each ADCP.

For sea bottom friction, C_{Dbc} is taken from the literature (Soulsby, 1983; Andersen et al., 2007) for muddy flat bottom (as observed from field), between 1.4×10^{-3} and

2.2×10^{-3}, i.e. equal to 1.8×10^{-3}. These values are consistent with the average drag coefficient estimated in the Gulf of St. Lawrence by Saucier et al. (2003) for various flat bottom, $C_{\mathrm{Dbc}} = 2.4 \times 10^{-3}$. In every case, within the interval $[z_{\min}, z_{\max}]$ under the ice, the TKE dissipation rate measured remains generally one order of magnitude higher than the one computed for sea bottom current friction. Subtracting the TKE dissipation due to current friction on the ice bottom from the total measured Γ_{t} results in an extension of the lower uncertainty bound in Fig. 4.5 by below 1% to 20% of the measured value.

For ice bottom friction, the drag coefficient C_{Dic} depends on the ice conditions, and is estimated following Lu et al. (2011). Their work consists in studying current drag on a set of separated plates of length L, draft $D_t = \frac{\rho_I}{\rho_w}\delta$ and ice concentration c_{ice}. They assume that the drag force applied by the current on the ice cover is the sum of the form drag, the drag due to the presence of large ice obstacle called 'ridges', and the skin friction. It leads to a total ice-ocean drag coefficient $C_w = C_w^e + C_w^r + C_w^s$ where C_w^e is the form drag coefficient, C_w^r is the drag coefficient due to the ridges, and C_w^s is the skin drag coefficient. In absence of ridges in the present work, where the turbulence was measured, $C_w^r = 0$. The form drag coefficient is

$$C_w^e = \frac{C_e c_{\mathrm{ice}} D_t}{2L}\left[1 - \left(\frac{c_{\mathrm{ice}}}{1-c_{\mathrm{ice}}}\frac{D_t}{L}\right)^{1/2}\right]^2, \; c_{\mathrm{ice}} < \frac{1}{1+\frac{D_t}{L}} \tag{4.31}$$

where $C_e \sim 1$ is the form drag coefficient for a single floe. The condition on c_{ice} is not valid in case of high sea ice concentration, inducing reduced drag due to wake effect (Steele et al., 1989). In these cases, which are prevalent in this work, C_w^e is set to 0. The form drag coefficient, C_w^e, is computed when the ice concentration is sufficiently low, i.e. on 2018-02-26 ($C_w^e = 1.1 \times 10^{-2}$) and 2019-03-06 ($C_w^e = 1.6 \times 10^{-2}$). The skin friction coefficient is

$$C_w^s = C_s c_{\mathrm{ice}} \tag{4.32}$$

where $C_s \sim 2.0 \times 10^{-3}$ is the skin friction coefficient for the bottom of a continuous ice cover. The ridge dependence of C_w^s that appear in Lu et al. (2011) was set to 0 in absence of ridges. The value of C_w^s for each days is computed, giving values very close to C_s, due to the high ice concentration, except on 2018-02-26 and 2019-03-06 where it is about 1.0×10^{-3}. Thereafter, the largest drag coefficient between C_w^e and C_w^s is chosen for the value of C_{Dic} for each days.

Depending on the deployment, within the interval $[z_{\min}, z_{\max}]$ under the ice, the TKE dissipation rate computed for current friction on the ice is between 1 and 100 % of the TKE dissipation rate derived from the High Resolution (HR) measurements. The fact that it reaches 100 % would either mean that, in that cases, the turbulence under the ice is not due to wave-ice interactions, but only to current-ice interactions, or that the estimate of the TKE dissipation due to the current is excessive. The first hypothesis seems

a bit more likely, as discussed below. Yet, the second one cannot be discarded, due to the assumptions made to compute the current TKE dissipation rate. When the 100 % current turbulence condition is met, Γ_t is set to 0. It happens for day 2018-02-19 and 2018-02-26 over the whole duration of the data sets.

Day 2020-02-25 is a good example where several conditions happen depending on the time and location. At the location of S489, for most of the deployment, the TKE dissipation rate computed for ice bottom current friction always reaches 100 % of the measured TKE dissipation rate. As discussed in next section, this is coincident with the Reynolds number, $\mathrm{Re_{wi}}$, of the wave flow near sea surface being much smaller than the threshold Reynolds number $\mathrm{Re_T} = 1000$. It should be noted that this Reynolds number is well below the critical Reynolds number for wave turbulence, $\mathrm{Re_{w,cr}} = 1.5 \times 10^5$. At the location of S497, two slightly different dynamics are observed. During time interval T1, the Reynolds number of the wave flow near sea surface is much higher than $\mathrm{Re_T}$, and, in the meantime, the modeled current friction on both the ice and the sea bottom make below 1 % of the turbulence measured under the ice. Then, during T2, the wave energy decreases until $\mathrm{Re_{wi}}$ becomes close to $\mathrm{Re_T}$, and the modeled current friction on both the ice (in majority) and the sea bottom (secondary) slightly increase in comparison to the measured turbulence, up to ~ 10 %. It is tempting to say that these two different regimes might explain the two depth profiles observed in the measured TKE dissipation rate plotted on Fig. 4.4. Indeed, the law of the wall observed during T2 could be related to the current friction on the ice, whereas the nearly constant ϵ with depth during T1 could be attributed to a mix of current-ice friction, wave-ice interactions and/or wave-current interactions (though that does not explain this particular profile). However, this is not always the case in the other data sets, since there are cases where the profile of the measured ϵ follows the law of the wall in case of both wave-ice turbulence (e.g. on 2018-03-02 and 2018-02-05), and there are cases of apparent constant ϵ when only current-ice turbulence happens (e.g. on 2018-02-19 and 2018-02-26).

Subtracting the TKE dissipation due to current friction on the ice bottom from the total measured Γ_t results in an extension of the lower uncertainty bound in Fig. 4.5 by 1% to 100% of the measured value.

Once the sum of the negative errors on Γ_t is subtracted from Γ_t, it gives the value of the total TKE dissipation rate per unit of sea surface area due to wave-ice interactions and potentially wave-current interactions. A comparison of the measured Γ_t is plotted in Fig. 4.5 for all the 10-minute average sampling periods investigated. To compare TKE dissipation to wave energy attenuation at the same ice fetch, Γ_w is computed at the location $x_{\mathrm{ice,r}}$ where Γ_t is estimated, as explained at the end of Chapter 3. What stands out in this graph is the fact that most of the points with uncertainties are spread between ~ 10 % and well below 10 % of wave attenuation, meaning that the turbulence is far from being the main cause of wave attenuation in these field studies.

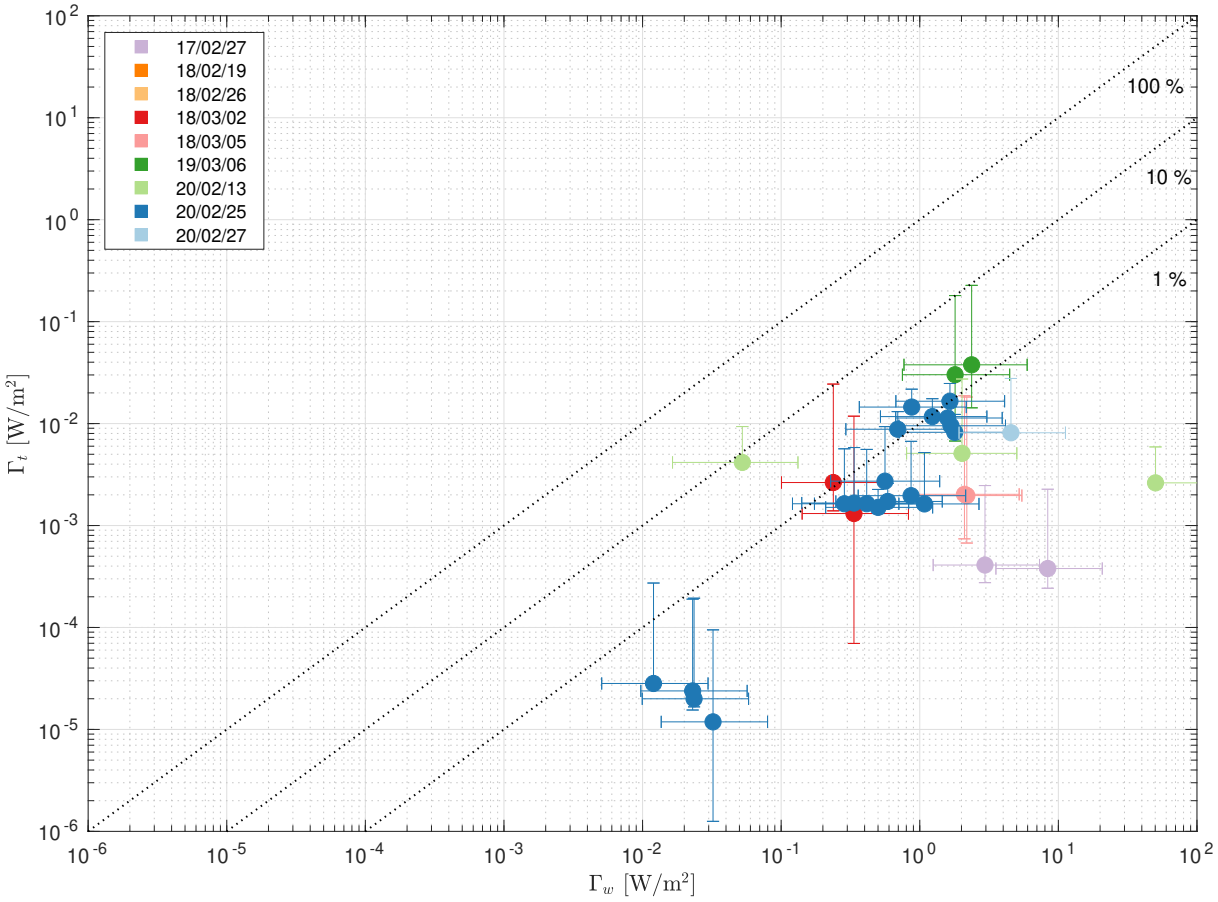

Figure 4.5 – Total TKE dissipation rate per unit of surface area, Γ_t, plotted against the total wave attenuation rate per unit of surface area, Γ_w. Each symbol represents an average of the data over 10 minutes, and the colors represent the different data sets. The dashed lines are delimiting the areas over which more than 100 %, 10 % and 1 % of wave attenuation is due to under-ice turbulence.

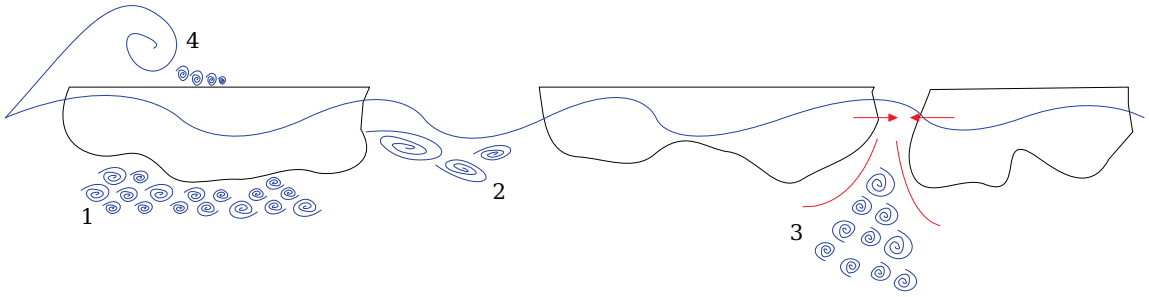

Figure 4.6 – Diagram of several sources of turbulence due to wave ice interactions. 1) skin friction, 2) form drag, 3) turbulent jet from floe-floe convergence, 4) overwash.

4.6 Turbulence sources in wave-ice interactions

Though the turbulence does not appear to be particularly important for wave energy dissipation due to wave-ice interactions, it is interesting to discuss the sources of under-ice turbulence related to the waves. Three sources of turbulence induced by wave-ice interactions are addressed from the data sets (see Fig. 4.6): skin friction, form drag and jets induced by floes convergence. Although I observed it qualitatively several times during field work, I had no means to quantitatively measure overwash. The turbulence generated through flow friction just between the floes was also not measured.

4.6.1 Wave friction under sea ice

The friction of ocean waves under sea ice happens in the form of skin friction and form drag, as discussed above for the current with Eq. 4.31 and 4.32 from Lu et al. (2011). They can be considered as different phenomena, since the first is based on the horizontal surface area of the floe, whereas the second works on the frontal area. Yet, it is difficult to separate them using turbulence measurements, since they both are expected to come with a TKE dissipation rate depth profile following the law of the wall. For this work, I did not go further than the distinction proposed by Lu et al. (2011), mostly depending on the ice concentration, that was applied above in the study of current-ice friction. In that case, mostly form drag would occur for day 2019-03-06, and mostly skin friction for the other days.

Another problem comes from the fact that the TKE dissipation rate depth profile measured under the ice seems to be largely due to current friction under the ice. Subtracting the friction of the current from the measurements often changes the TKE dissipation rate depth profile in addition to its mean amplitude, leading sometimes to profiles no longer following the law of the wall. My intuition is that this can be due to other wave-ice interactions at stake, which is partly discussed below, or to wave-current interactions, not studied in this work.

Despite my misgivings concerning the TKE profile, I decided to calculate the drag coefficient of the waves on the ice as if all the turbulence under the ice was due to skin friction or form drag. The purpose of this choice is to be able to compare the obtained coefficients with the results of Voermans et al. (2019), as well as simply to provide values of drag coefficients due to wave friction under the ice, which are still very rare in the literature. On the one hand, the TKE dissipation rate supposedly only due to wave-ice interactions was computed as explained above, and integrated over the interval $[z_{\min}, z_{\max}]$ to compute the total TKE dissipation rate per unit of sea surface area due to wave-ice interactions, Γ_{twi}. On the other hand, Eq. 4.16 was used to express the TKE dissipation rate, ϵ_{wi}, as a function of the drag coefficient due to wave-ice interactions, C_{Dwi} and of the surface wave orbital velocity, U_{surf}, defined by Eq. 3.10. Considering that

$$\Gamma_{\text{twi}} = \rho_w \int_{z_{\min}}^{z_{\max}} \epsilon_{\text{wi}}(z) dz = \rho_w C_{\text{Dwi}}^{3/2} \frac{U_{\text{surf}}^3}{\kappa} \log\left(\frac{z_{\max}}{z_{\min}}\right), \tag{4.33}$$

allows to derive an expression for the drag coefficient for wave-ice interactions:

$$C_{\text{Dwi}} = \left(\frac{\kappa \Gamma_{\text{twi}}}{\rho_w U_{\text{surf}}^3 \log\left(\frac{z_{\max}}{z_{\min}}\right)}\right)^{2/3}. \tag{4.34}$$

The drag coefficients C_{Dwi} is computed at each ADCP for each day when $\Gamma_{\text{twi}} \neq 0$, i.e. when there were potentially turbulence due to wave-ice interactions.

The surface waves Reynolds number Re_{wi} is estimated for each day using Eq. 4.10 with U_{surf} for the velocity scale,

$$\text{Re}_{\text{wi}} = \frac{U_{\text{surf}}^2 T_{\text{m01}}}{2\pi\nu_w}. \tag{4.35}$$

They are both shown in Tab. 4.1. The values in the Table are means over all of the 10-minutes intervals for each data set, and the errors are one standard deviation from the mean. No statistical error are computed for day 2020-02-27 since there is only one time interval.

Two results, to be taken with caution, emerge from Tab. 4.1. First, there seem to be a transitional waves Reynolds number, Re_{T}, close to 1000, below which $\Gamma_{\text{twi}} = 0$, i.e. below which there is for sure no turbulence due to wave-ice interactions, and over which $\Gamma_{\text{twi}} \neq 0$, which could be attributed to wave friction under the ice. This transitional Reynolds number does not separate overall laminar flow from overall turbulent flow, since the turbulence is at least generated by the current friction under the ice. Neither does it allow to affirm that the wave driven flow is turbulent or not, since the critical Reynolds number for wave driven flow, $\text{Re}_{\text{w,cr}} = 1.5 \times 10^5$, is much larger than this transitional Reynolds number. Again, it could be related to another wave-ice interaction that would become dominant below that threshold, or to changes in the wave-current interactions.

Second, considering that wave-ice interactions only happen through wave-ice friction leads to wave-ice drag coefficient between 1×10^{-2} and 2×10^{-2}. The exception of day 2018-03-02 is dubious since the associated Reynolds number is quite lower than the transition Reynolds number. Most of the literature about under-ice turbulence deals about current friction on the ice (e.g. Steele et al., 1989; Lu et al., 2011; Fer et al., 2022), which happens at different scales than wave friction. Yet, it can be noted that the obtained drag coefficients for the waves are within the range of this literature, which is between 10^{-4} and 10^{-2}.

To my knowledge, the only other paper discussing measurements of drag coefficient from wave friction on sea ice is the one of Voermans et al. (2019), already introduced in Chapter 1. In this paper, they observe generally lower ice concentrations, between 0.1 and 0.6, and comparable to higher wave Reynolds numbers, between 7×10^3 and 1.5×10^5 (according to the Supporting Information and using Eq. 4.35). They also seem to remove the effect of the current shear on the ice from their turbulence measurements under the ice. Supposing that all of the remaining measured turbulence is due to turbulent wave friction on the ice, they come up with a coefficient b_2 analogous to a drag coefficient, as a function of the ice concentration. For an ice concentration higher than 0.4, its expression is $b_2 = 1.0 \times 10^{-7} \exp(20c_{\text{ice}})$. Using this expression in the present work, where the ice concentration is generally close to 1, gives drag coefficients that should be of order 1 to 10, which is much higher than the drag coefficients in Tab. 4.1. This discrepancy is probably due to a lack of measurements at high ice concentration to perform the fit leading to b_2. But it could also be related to the fact that they were actually not always measuring turbulence from wave friction on the ice (probably as in this work), according to their wave Reynolds numbers that are mostly below $\text{Re}_{\text{w,cr}}$.

This observation suggests that, when studying turbulence in wave-ice interactions, one must consider both all sources of turbulence due to these interactions, and probably also the interactions between waves and current.

4.6.2 Jet turbulence

The generation of turbulent jets due to floe-floe convergence was investigated using the theoretical framework of the plane jet (e.g. Pope, 2000), of mean velocity $u_j(z)$ and width $L_j(z)$ at a distance z from the jet nozzle (which is here also the distance from the ice bottom). Under the assumption that the jet follows the law of similarity, i.e. that the cross section of the jet has a Gaussian shape and that the velocity profile in cross sections at different distances z only changes in amplitude with respect to z, the mean jet velocity at the centre of the jet is (e.g. Pope, 2000):

$$u_j(z) = \frac{1}{2} B_j d \frac{V_0}{z}, \tag{4.36}$$

Table 4.1 – Wave-ice Reynolds number and drag coefficient for the different deployments.

Day	Device	$\mathrm{Re_w}$	$C_{\mathrm{Dwi}} \times 10^{-2}$
2017-02-27	Aquadopp	1100 ± 600	1.2 ± 0.7
2018-02-19	Aquadopp	470 ± 80	N/A
2018-02-26	Aquadopp	100 ± 100	N/A
2018-03-02	Aquadopp	800 ± 90	4.0 ± 4.0
2018-03-05	Aquadopp	2300 ± 400	1.1 ± 0.1
2019-03-06	Aquadopp	7200 ± 1600	1.4 ± 0.2
2020-02-13	S489	100 ± 100	N/A
2020-02-13	S497	2000 ± 300	2.1 ± 0.7
2020-02-25	S489	17 ± 5	N/A
2020-02-25	S497	4300 ± 1500 (T1) 1600 ± 500 (T2)	1.1 ± 0.4 0.9 ± 0.4
2020-02-27	S489	8000	1.7

where $B_j = 5.8$ is an experimental constant (see Pope, 2000), d the width of the nozzle of the jet, which is here the distance between the ice floes that are converging, and V_0 the velocity at the nozzle of the jet. This expression of $u_j(z)$ is only valid outside the nozzle of the jet, away from the ice.

The velocity V_0 is computed on average as the product of the average water volume per unit of sea area, ϕ_w, and the horizontal divergence of the wave orbital velocity at the surface.

The average water volume per unit of sea area is the mean fraction of the volume of water being ejected between the floes, over the total sea surface:

$$\phi_w = \delta(1 - c_{\mathrm{ice}}), \tag{4.37}$$

where the factor $(1-c_{\mathrm{ice}})$ represents the mean water concentration between the floes. This mean water concentration includes ice in the form of frazil/slush between the floes, since it is also impacted by the convergence/divergences of the floes. However, the effect of this presence of ice crystals between the floes on the eventual damping of the convergence of the floes has not been studied.

The surface velocity is obtained using the wave omnidirectional spectrum $E(f)$ measured thanks to the SKIB on the ice floe where the ADCP is measuring the turbulence. The maximum of the wave spectrum E_p is used to derive the peak angular frequency ω_p and the peak amplitude $a_p = \sqrt{2E_p}$, and the peak wave number k_p is derived from the wave dispersion relation in sea ice (see Eq. 3.15). Then the horizontal component of

the surface velocity, u, in the wave direction, are calculated, for position x in the wave direction and time t:

$$u(x) = a_p \omega_p \cos(k_p x - \omega_p t), \tag{4.38}$$

where $g = 9.81$ m.s^{-1}, ρ_i and ρ_w are respectively sea ice and sea water density. Then, the velocity at the nozzle of the jet is:

$$V_0 = \phi_w \frac{du}{dx}. \tag{4.39}$$

The width of the jet is often observed proportional to the square root of the distance from the nozzle of the jet for plane jets, i.e. $L_j(z) \sim z^{1/2}$ (Pope, 2000), outside the nozzle of the jet. In the nozzle of the jet, the dominating scale is d.

Considering that u_j is also the velocity of turbulent eddies of size L_j, an order of magnitude of the TKE dissipation rate in a turbulent flow is computed using Eq. 4.18:

$$\epsilon = \frac{u_j^3}{L_j}. \tag{4.40}$$

Therefore, the TKE dissipation rate for the jet is

$$\epsilon_j(z) \sim \min\left(\frac{(B_j d V_0)^3}{8 z^{7/2}}, \frac{V_0^3}{d}\right). \tag{4.41}$$

The TKE dissipation rate due to wave-ice interactions, ϵ_{wi}, for day 2020-02-25, during time interval T1, at the location of S497, was compared to the modeled TKE dissipation rate using Eq. 4.41, with a mean distance between the floes d estimated to be close to 0.2 m after manual segmentation of the ice cover around S497. For both time interval T1 and T2, ϵ_j remained one order of magnitude below ϵ_{wi}. In addition, the profile of $\epsilon_{wi}(z)$ with distance to the ice was not following a $z^{-7/2}$ law expected for $\epsilon_j(z)$. Even for other days, when d was not estimated, testing realistic values for d between 1 m and 0.05 m did not allow to reach TKE dissipation rates values comparable to ϵ_{wi}. This means that jet turbulence under the ice generated through convergence and divergence of the ice floes was negligible compared to other sources of turbulence in these data sets. This is consistent with the measurements of Løken et al. (2022) that compared under ice turbulence to jet turbulence, using ADCPs under the ice, and between the colliding floe and the pool. They did observe the occurrence of a jet, using a Remotely Operated underwater Vehicle, but they found that the TKE dissipation rate due to under ice turbulence was on average one order of magnitude larger than the one due to jet turbulence.

However, the parameter space of the present work was limited to generally high floe concentration (implying a small d) and small wave amplitudes, whereas the velocity dependence of u_j suggests that the jet would be stronger for larger d and for higher (and steep) waves. Such wave would not propagate far into the ice cover, but could potentially

generate non-negligible jet turbulence close to the ice edge.

Chapter 5

Floe-floe interactions in dense MIZ

5.1 Ice cover segmentation

Automatic segmentation of an image is a topic widely covered in the literature, and already broadly used in case of ice cover pictures (see review of Zhang and Skjetne, 2018) to separate the ice from the ocean. This separation is used to compute properties of the ice field, such like the ice concentration, the Floe Size Distribution (FSD), and other distributions based on the area, the perimeter or the orientation of the floes. The different floe properties distributions are used in part for the classification of the different ice covers encountered. They are also necessary to quantify how much ice properties change when getting farther and farther away from the ice edge, to explain the observed deviations from the exponential decay of the wave energy, represented by the green slopes in Fig. 3.4. Such quantification is an important step towards the modeling of wave-ice interactions. In particular, the calculation of the dominant floe scales of the ice cover can be used in the context of turbulence modeling for the estimation of roughness lengths of the ice cover, or to derive the most relevant scale that can be used to compute the Reynolds number of the wave flow.

Estimating the ice concentration does not require a clean segmentation since the only thing required is to distinguish the ice from the sea water. Yet, for other properties based on the shape of the floes, the ice pieces need to be individually segmented, which can be challenging depending on the quality of their separation. A threshold method (Otsu, 1979) is often enough to compute the ice concentration, and can be sufficient to get a clean ice segmentation if the floes are well separated and if the sea water in between the floes is free of ice (brash and slush). When floes are touching, the segmentation becomes more complicated since the contact point is considered by the threshold method as part of the ice layer (oversegmentation), merging the touching floes into one piece of ice in the binary picture. In that case, if the contact points are small enough compared to the floes, morphological image analysis operations (Soille, 1999) can be used to erode these points, and thus separate the floes. Real cases are often more complicated, with floes being in contact along a full edge, with snow hiding the junction between the floes, with

new snow on some floes and floes where the snow has been overwashed by waves, and/or with brash ice and slush in the water between the floes. In these conditions, a portion of the water might be oversegmented as part of the ice matrix, and some greyish portions of overwashed floes might be undersegmented as part of the water matrix. Other more sophisticated methods are thus needed, such like the watershed method (Vincent and Soille, 1991) or the gradient vector flow snake algorithm (Zhang and Skjetne, 2015).

In this work, the ice field properties (concentration, area and sizes) are derived from the segmentation of the pictures taken by the UAVs, when available. However, the richness of the shades of grey present in each image, due to variable superimpositions of water, snow and ice, as for example on Fig. 5.1.a, did not allow to reliably distinguish ice floes from each other without human intervention. Fig. 5.1.b is an example segmentation of a typical ice cover, using a kmeans thresholding method (p. 17-33, MathWorks®, 2022b) to separate the shades of grey of the picture in 5 different categories, coupled to morphological image analysis operations (erosion + dilation) on each category to remove the links between the segmented floes as often as possible. This processing did not allow to separate the floes as needed to compute a FSD, but is a good example of the problem encountered in general: part of the floes are undersegmented, cutting the floes in several pieces and also resulting in water holes within the floes, and many floes are oversegmented. Watershed method and gradient vector flow snake algorithm were also tested on this picture without better results.

For comparison, Fig. 5.1.c shows an ideal segmentation, manually produced. Since it is very time consuming, I could not apply it for all of the ice covers of this work, but it is a good reference to check the computation of the ice concentration using the automated segmentation on this case. Using Fig.5.1.b, the ice concentration computed is $c_{\text{ice}} = 0.7$, which differs from the reference $c_{\text{ice}} = 0.87$ computed from Fig.5.1.c with a 20 % error. In general, for most of the deployment days, both from field experience and according to the segmentation, the ice concentration was close to 1 (see Table 2.1). The main exceptions are day 2019-03-06, where the ice concentration was estimated between 0.3 and 0.4, and day 2020-02-26, where it was between 0.5 and 0.7. Yet, even for these two cases, one could consider that the ice concentration was close to 1, since the space between the solid ice floes was mostly filled with a thick layer of slush/frazil. Therefore, c_{ice} as it is computed here would more precisely correspond to the concentration of solid ice. This definition is the one used throughout this work, for it was focused on solid ice to explain wave attenuation, but keeping in mind that the rheology of the soup of ice in between the floes has properties different from sea water.

In addition, I computed the cumulative FSD for both automated and manual segmentation. The cumulative FSD is, at each floe size L_f, the number of floes N_f with size larger than L_f divided by the total number of floes N_0, i.e. $F_{\text{cum}} = \frac{N_f(>L_f)}{N_0}$. It is often

observed following one or two power laws (Stern et al., 2018):

$$F_{\text{cum}} = C_{\text{FSD}} L_f^{1-\gamma_f}, \tag{5.1}$$

where $C_{\text{FSD}} = F_{\text{cum}}(\min(L_f))^{-1}$ and $1-\gamma_f < 0$ is the power law exponent. Here, I choose to use $1-\gamma_f$ according to Stern et al. (2018) to refer to γ_f which is the exponent of the non-cumulative FSD F_{ncum}.

The cumulative FSDs based on the automated and manual segmentation of Fig. 5.1 are plotted on Fig. 5.2. The floe size considered is the mean between the major and the minor axis of each floe. Two least square linear fits of the logarithm of the distributions (Eq. 5.1) are performed on the two slopes observed for each distribution in the log-log plot. For the FSD based on the automated segmentation, $\gamma_f = 2.72 \pm 0.08$ for the steepest slope, and $\gamma_f = 1.95$ for the less steep one. For the FSD based on the manual segmentation, $\gamma_f = 3.83 \pm 0.03$ for the steepest slope, and $\gamma_f = 1.81 \pm 0.01$ for the less steep one. The values of γ_f for the flattest slope are consistent with the literature (see review of Stern et al., 2018) for cumulative FSDs, and the steepest slopes are a bit steep, but still within what can be find in the literature. Comparing the FSDs from automated and manual segmentation, the steepest slope is less steep for the automated segmentation due to the fusion of a lot of segmented floes, generating artificially more large floes, but the flattest slopes are rather close. Another difference is at small scale (below 0.5 m), where the FSDs derived from the manual segmentation exhibits a plateau, not observed from the other distribution since artificially smaller floes are generated from the automated segmentation. This plateau does not appear in the literature either, which could be due to the fact that the floe size in the literature is generally well over 1 m, compared to this work where the manual segmentation allowed to resolve floes down to 0.2 m, meaning that a minimum floe size has perhaps been reached. Another reason could be more pragmatic: the manual segmentation is limited by the human ability to distinguish the smallest floes from the noise in the picture, and this difference would then be a matter of resolution.

This issue has not been resolved in the following due to the fact that the thesis time is incompressible. Only the ice concentration and the shape of very specific floes is computed when needed and when possible. However, the work done on the FSD paved part of the way for future efforts in similar ice cover conditions.

5.2 Floe-floe interactions

5.2.1 Floe collisions

Physically, collisions between one floe and its neighbours are momentum transfer from the considered floe to the others. Given that the movement of the floe before collision is

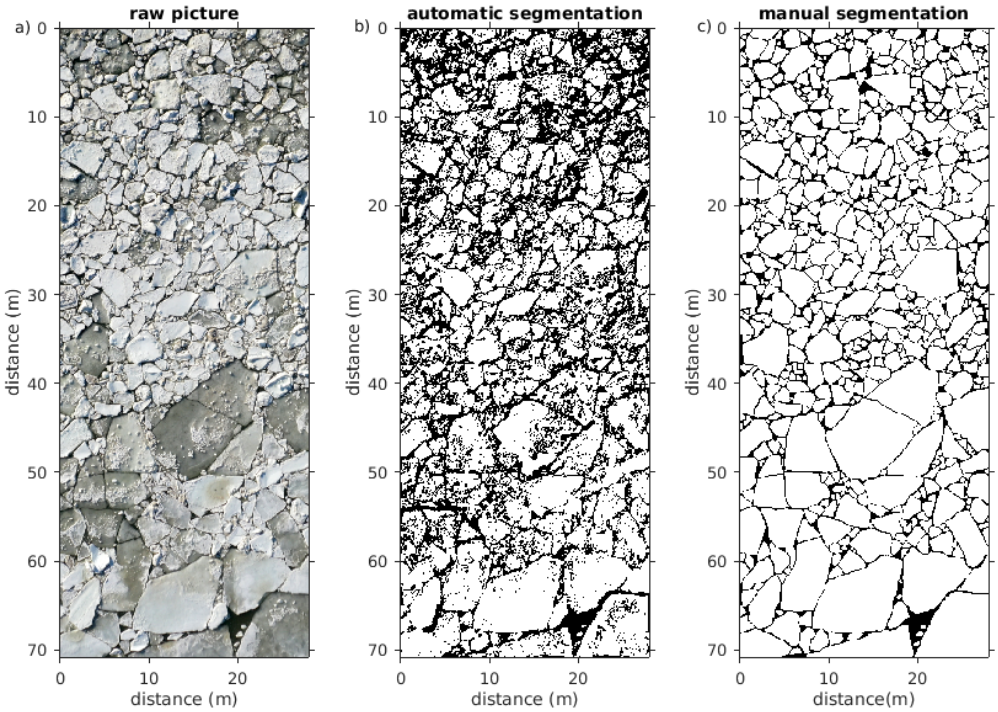

Figure 5.1 – Example of ice cover segmentation based on a UAV picture taken on day 2020-02-25. a) is the raw picture, b) is the automated segmentation and c) is the manual segmentation.

driven by the wave field, collisions are also energy transfer from the wave field to the ice field. This energy transfer can be computed in terms of the difference of kinetic energy E_{coll} before (K_b) and after (K_a) the impact (Li and Lubbad, 2018; Løken et al., 2022):

$$E_{\text{coll}} = |K_a - K_b|. \tag{5.2}$$

The kinetic energy of a solid body of mass m is:

$$K = \frac{1}{2}m(v_x^2 + v_y^2 + v_z^2) + \frac{1}{2}m(I_x\omega_x^2 + I_y\omega_y^2 + I_z\omega_z^2), \tag{5.3}$$

where v_i (for $i = x, y, z$ in the solid body reference frame) is the velocity of the body along axis i, I_i is the moment of inertia of the body with respect to axis i and ω_i is the angular velocity of the body around axis i. For the case of an ice floe, to compute the moments of inertia, I made the assumption that a floe is a cylinder of radius R and height equal to the floe thickness, δ, to avoid computing the orientation of the floe with respect to the wave direction. The pseudo-radius R is computed using the measurement of the area A_f of the floe from UAV data as $R = \sqrt{\frac{A_f}{\pi}}$ to conserve the area of the real floe. Therefore, the moments of inertia of the floe, in the reference frame at the center of the top of floe, are $I_x = I_y = \frac{1}{2}R^2\left(\frac{1}{2} + \frac{2}{3}\left(\frac{\delta}{R}\right)^2\right)$ and $I_z = \frac{1}{2}R^2$. E_{coll} is computed for all of

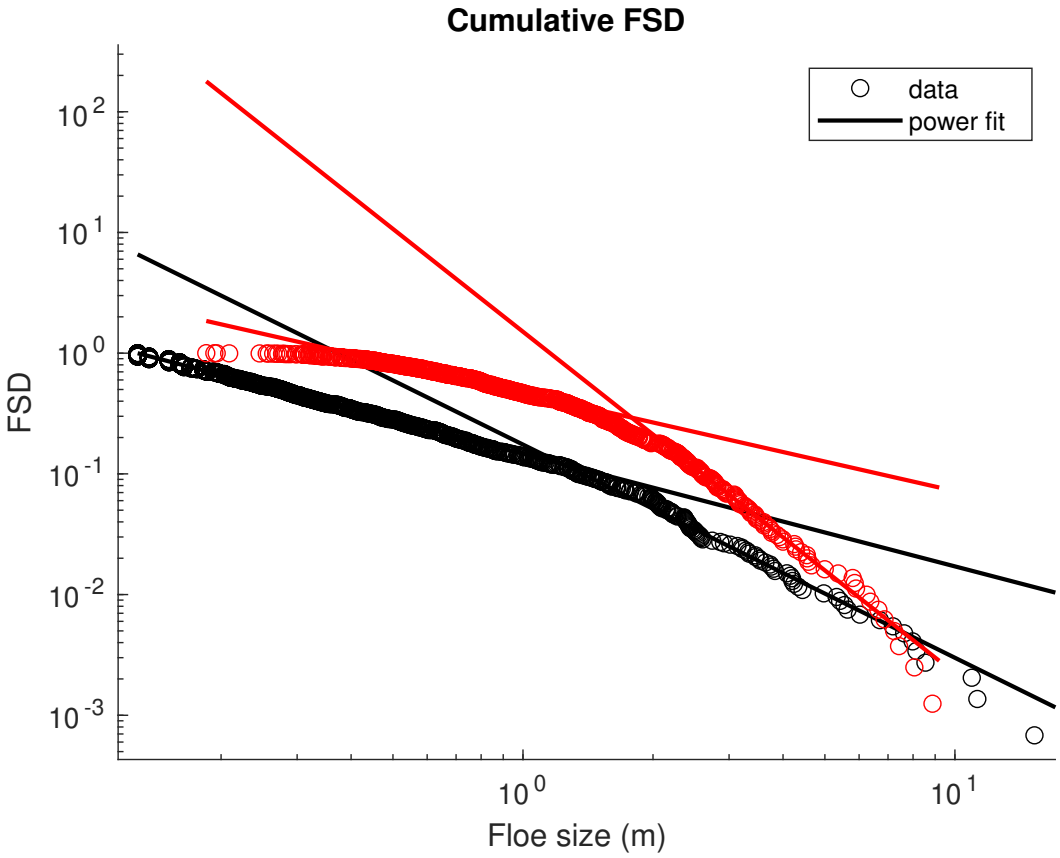

Figure 5.2 – Cumulative FSD of the mean between the major and minor axis of each floe in Fig. 5.1 using the automated segmentation (black) and the manual segmentation (red). The lines represent the two power laws fitted to the data (circles).

the N_c collisions occurring during the reference 10-minutes segments of the wave data analysis, and summed, before being divided by this duration Δt_c to obtain the collisions power. Dividing the power by the horizontal surface area A_f of the floe gives the total energy dissipation rate per unit of sea surface due to floe collisions,

$$\Gamma_{\text{coll}} = \frac{1}{\Delta t_c A_f} \sum_{p=1}^{N_c} E_{\text{coll,p}}, \tag{5.4}$$

which can be compared to Γ_w. In Eq. 5.4, $\sum$ represents the summation over the N_c collisions happening during the time interval Δt_c.

Ice floe collisions were investigated using the SKIB data. In the data, the collisions appear as spikes induced by the abrupt change in acceleration and angular velocity of the floe (see Fig. 5.3.a). The trend of the data is computed using Matlab algorithm `medfilt1` (p. 1408, MathWorks®, 2020), with filter order 15, to remove the spikes. Then, this trend is subtracted from the raw data to only keep the spikes, which are detected using Matlab algorithm `findpeaks` (p. 798, MathWorks®, 2022a). `findpeaks` allows to obtain both the location of the peaks, as well as their height and their width at mid-height. A peak is considered to be a collision when the associated acceleration exceeds a threshold of 0.25 m.s^{-2}. Below this threshold, I observed that either the change in velocity (and therefore kinetic energy) induced by the collision is negligible (for example, the second red circle starting from the left of Fig. 5.3), or the peak is not a collision. In the second case, the peak is often larger (in time) than for a collision, and the observed change in speed (or angular momentum) is due to the wave orbital motion. The time width between just before and just after the collision is set experimentally as twice the width of the peak at mid-height, which gave average values close to the 0.2 s used by Løken et al. (2022). The velocity of the floe is computed by integrating the acceleration data using cumulative trapezoidal numerical integration and then a Butterworth high pass filter of cutoff frequency 0.1 Hz to remove low frequency noise (see Fig. 5.3.b). Last, the mass of the floe $m = \rho_w A_f \delta$ is computed using the area A_f times the thickness δ of the floe, as well as the ice density, which is roughly estimated close to $\rho_I = 900$ kg.m^{-3}.

This processing is used on all the floes upon which there was a SKIB, if collisions were detected in the data, and only when I had a picture of the floe to compute the area, the pseudo-radius and the mass of the floe. Given these conditions, Γ_{coll} was computed for days 2018-02-19, 2018-02-26, 2019-03-06, 2020-02-13 and 2020-02-25. For all of these days, as Løken et al. (2022) also observed, the share of collision energy due to the change in acceleration during the collisions is 2 orders of magnitude higher than the share due to change in angular momentum, which means that the cylindrical assumption made for the computation of the moments of inertia of the floe does not affect significantly the value of Γ_{coll}. In addition, the collision energy due to the change in acceleration along the z axis is 2 to 3 orders of magnitude below the collision energy due to the change in acceleration

along the x and y axes, meaning that the collision energy dissipation is mostly based on the accelerations in the horizontal plane.

This result allow to simplify the expression of Γ_{coll} :

$$\begin{aligned} \Gamma_{\text{coll}} &= \frac{1}{A_f \Delta t_c} \frac{1}{2} m \sum_{p=1}^{N_c} \left[\left| v_{x,a,p}^2 - v_{x,b,p}^2 \right| + \left| v_{y,a,p}^2 - v_{y,b,p}^2 \right| \right] \\ &= \frac{1}{\Delta t_c} \frac{1}{2} \rho_w \delta \sum_{p=1}^{N_c} \left[\left| v_{x,a,p}^2 - v_{x,b,p}^2 \right| + \left| v_{y,a,p}^2 - v_{y,b,p}^2 \right| \right] \end{aligned} \tag{5.5}$$

Fortunately, the floe area vanishes from the expression of Γ_{coll}, meaning that it can be computed for any data set, provided that there are collisions. Therefore, Γ_{coll} is computed for every data set except day 2018-03-02 (during which no collisions are recorded).

The main source of error in Γ_{coll} is the error on the ice thickness, which is about 30 % of the total ice thickness (Sutherland and Dumont, 2018), leading to 30 % of error on Γ_{coll}. The error on the estimation of the velocities before and after collision are not computed systematically. However, by comparing the velocity automatically detected, thanks to the algorithm `findpeaks`, to the velocity detected by eye (which is supposed to be more accurate) for a couple of collision spikes, only 1 to 2 % of error were found. The uncertainty of the attachment of the buoy to the floe was not computed, but would result in a weak underestimation of E_{coll}.

To compare energy dissipation due to collisions to wave energy attenuation at the same ice fetch, Γ_{w} is interpolated at the location $x_{\text{ice,r}}$ where Γ_{coll} is estimated, as explained at the end of Chapter 3. Fig. 5.4 shows that the energy dissipation rate due to ice floe collisions is much higher than the TKE dissipation rate in a large number of cases. For days 2018-02-19, 2020-02-25, and 2020-02-27, within the uncertainties, collisions accounted locally for up to 100 % of wave attenuation. In total, after averaging the energy dissipation due to collisions over time and buoy location for each data set, collisions can explain all of the wave energy attenuation for 1 deployment day out of 9.

However, there are also cases where collisions are less significant for wave attenuation. Among these cases, day 2019-03-06 is characterised by a low concentration of solid ice floes, which is relevant with the fact that collisions are less likely to happen in this case compared to higher concentration cases. Days 2017-02-27, 2018-03-05 and 2020-02-13 are a cases where the proximity of the floes and the presence of slush in between the floes might have limited the amplitude of the collisions. For day 2020-02-25, even though the ice concentration was high, a couple of collision points are below 1 % of wave attenuation. This is coincident to lower wave energy, since these points belong to time interval T2.The low Γ_{coll} for day 2018-02-26 is likely due to a medium ice concentration and to the fact that the colliding floe was only surrounded by smaller floes, inducing lower kinetic energy transfer. More data points in various ice and wave conditions would be necessary to derive a reliable trend. For future field experiments, to properly estimate the share of wave attenuation due to floe collisions, the following quantities have to be measured systematically: the

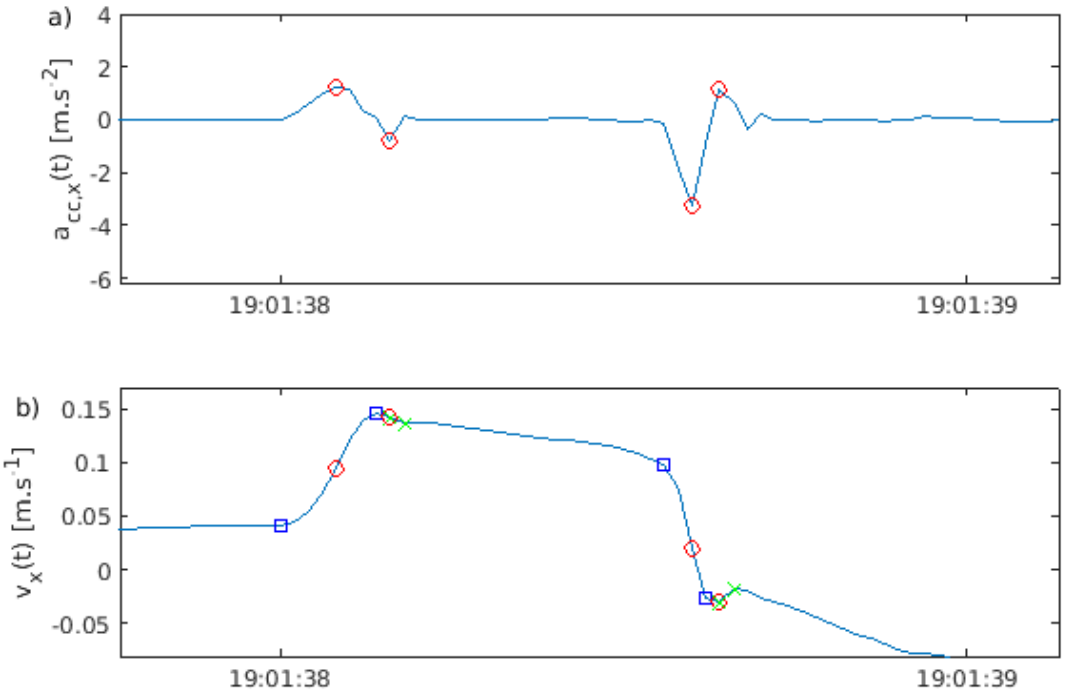

Figure 5.3 – x-wise a) floe acceleration $a_{cc,x}$ and b) floe velocity v_x data with time in the reference frame (x, y, z) of a SKIB placed on the considered ice floe, 2020-02-25. Red circles indicate the location of the tip of the collision spike. Blue squares are located one spike width at mid-height before the red circle, and green crosses are located one spike width at mid-height after the red circle. The vertical distance between a blue square and a green cross indicate the change in floe velocity induced by a collision.

acceleration and thickness of the colliding floe to compute Γ_{coll}, and the wave energy at two floes near upstream and downstream of the colliding floe, to compute Γ_{w}. In any case, adding collision to turbulence induced wave energy dissipation does not always explain all of the wave energy attenuation in sea ice.

5.2.2 Floe raft compaction

Under very concentrated ($\sim$ 100 %) ice conditions, the ice floes tend to raft on top of each other (e.g. see Fig. 2.4.i), and to be compressed in a rough ice layer by the wave radiation stress (Longuet-Higgins and Stewart, 1964). To deal with this type of floe-floe interactions, I relied on the work of Sutherland and Dumont (2018), following previous literature (Dai et al., 2004; Hopkins and Tuhkuri, 1999; Uzuner and Kennedy, 1976), who applied Mohr-Coulomb (MC) theory to similar ice conditions as the one of this work during the BicWin 2016 and 2017 field experiment.

MC granular materials theory has been used to describe the behaviour of floating ice in a variety of circumstances including ice jams in rivers, (Uzuner and Kennedy, 1976), frazil

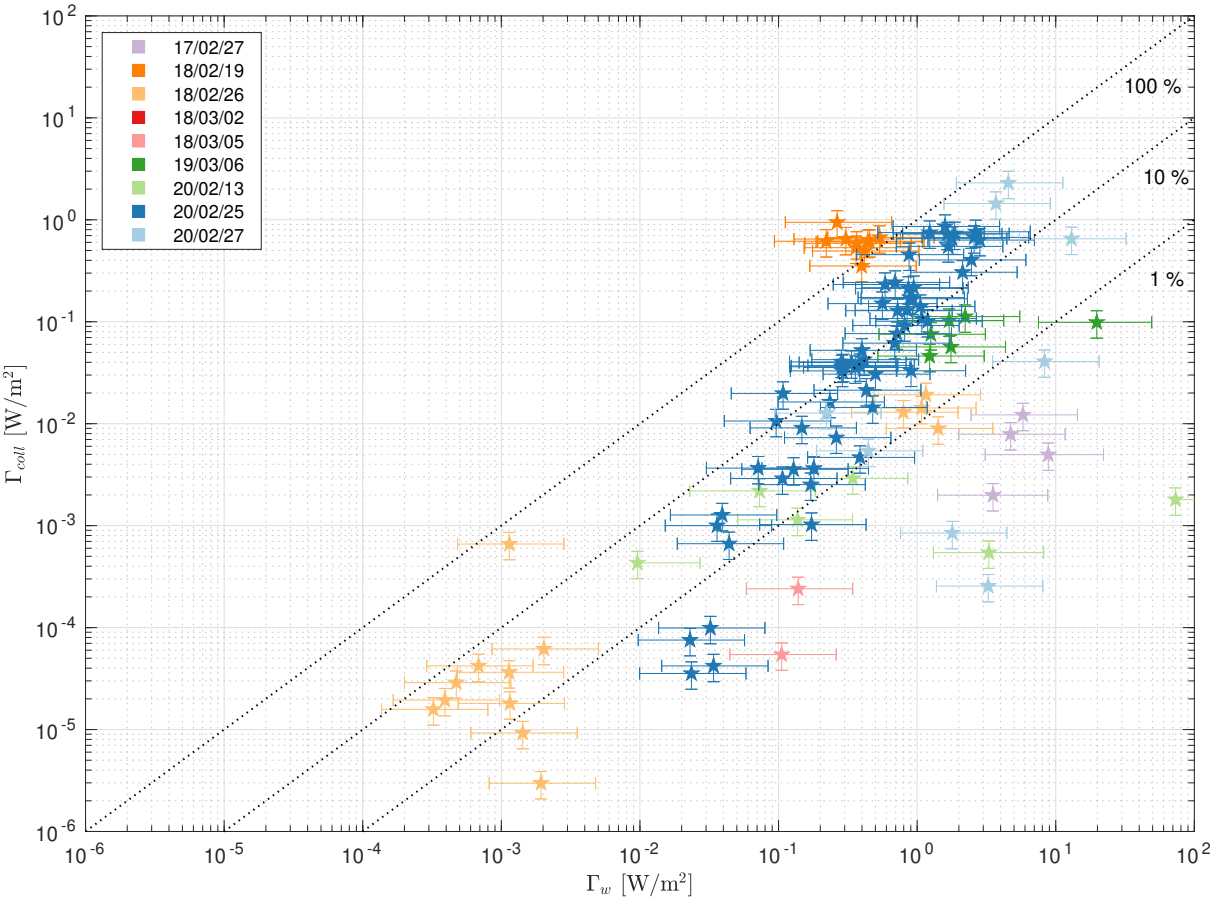

Figure 5.4 – Total energy dissipation rate per unit of surface area due to collisions, Γ_{coll}, plotted against the total wave attenuation rate per unit of surface area, Γ_{w}. Each symbol represents an average of the data over 10 minutes, and the colors represent the different data sets. The dashed lines are delimiting the areas over which more than 100 %, 10 % and 1 % of wave attenuation is due to floe-floe collisions.

compaction (Martin and Kauffman, 1981), and floe stacking in the MIZ (Dai et al., 2004; Sutherland and Dumont, 2018), as well as for larger-scale 2D ice behaviour (Williams et al., 2017). The basic tenet of MC theory is that the failure stress of a MC material in one direction is related to the compressive stress in an orthogonal direction. In the case of floating ice, this is typically expressed as the horizontal failure stress σ_x can be written in terms of the vertical stress σ_z as

$$\sigma_x = \sigma_z \left(\frac{1 + \sin\beta}{1 - \sin\beta} \right), \tag{5.6}$$

where β is the internal friction angle of the material.

To compute the vertical stress, the gravity force acting on the ice above and below the water surface is computed. The vertical stress at any level z above the water line is determined by the weight per unit area of ice above that level:

$$\sigma_z(z)\Big|_{0 \leq z \leq \delta_f} = \rho_I g (1 - n)(\delta_f - z). \tag{5.7}$$

In Eq. 5.7, n is the fraction of the ice matrix that is filled with air or water, called porosity, ρ_I is the ice density, and δ_f is the ice freeboard (the part of the ice above the water surface). The vertical stress at any level z below the water line is determined by the integrated buoyancy force per unit area of ice below that level,

$$\sigma_z(z)\Big|_{-\delta_d \leq z < 0} = g(1 - n)(\rho_w - \rho_I)(\delta_d + z), \tag{5.8}$$

where δ_d is the ice draft (the part of the ice below the water surface). The average vertical normal stress can then be determined by integrating the stress over the entire thickness $\delta = \delta_f + \delta_d$ of the ice raft:

$$\overline{\sigma_z} = \frac{1}{\delta} \int_{-\delta_d}^{\delta_f} \sigma_z(z) dz = \frac{1}{2} \rho_I g (1 - n) \left(1 - \frac{\rho_I}{\rho_w} \right) \delta \tag{5.9}$$

Combining Eqs. 5.6 and 5.9, the mean horizontal stress σ_x is derived, and multiplied by the ice thickness δ to get the horizontal force per unit length (in the cross-wave direction), G, required to compress the ice raft further:

$$G = K_r \delta^2, \tag{5.10}$$

where

$$K_r = \frac{1}{2} \left(1 - \frac{\rho_I}{\rho_w} \right) (1 - n) \rho_I g \frac{1 + \sin\beta}{1 - \sin\beta}. \tag{5.11}$$

Hereafter, I used the following values for the parameters in Eq. 5.11: $g = 9.81$ m.s^{-2}, $\rho_w = 1020$ kg.m^{-3}, $\rho_I = 900$ kg.m^{-3}, $\beta = 34 \pm 2°$ and $n = 0.375 \pm 0.025$ according to

Sutherland and Dumont (2018).

The MC-radiation stress framework provides a potential method for estimating wave energy attenuation in floe jumbles. When the ice converges and diverges with wave motions, it can be thought to be moving against a resisting MC stress, over a distance related to the horizontal component of the wave orbital motion. The force per unit crest length required to compress the ice jumble is given in Eq.5.10, so the energy attenuated per wavelength and wave period can be written

$$\Delta E_{\lambda,T} = K_r \delta^2 l_c, \tag{5.12}$$

where l_c is the amplitude of the compression of the floe jumble for each wave period (related to the wave amplitude, a). Division by T and λ then gives the dimensional dissipation rate,

$$\Gamma_{\mathrm{MC}} = \frac{K_r \delta^2 l_c k \omega}{4\pi^2}, \tag{5.13}$$

which has units of $\mathrm{W.m^{-2}}$. Clearly then, the compression amplitude, l_c, is the key to successful estimation of energy attenuation. Two potential formulations for l_c are considered.

The compression amplitude, l_c, depends on the relaxation velocity, v_{rx}, the speed at which the floes separate when forcing is removed, and can be approximated by,

$$l_c \approx \begin{cases} 2a & , \quad v_{rx} > a\omega \\ 2\pi v_{rx}/\omega & , \quad v_{rx} < a\omega \end{cases}. \tag{5.14}$$

This states that if v_{rx} is faster than the wave orbital velocity, then the distance over which the ice is compressed will be proportional to the wave amplitude, a. If v_{rx} is slower, then the ice will be compressed over the distance it has expanded since its previous compression. This second condition was not met in the different wave ice interactions of this work, and therefore not further investigated.

In the case of this work, where the restoration of the floe-field is faster than the wave orbital velocity, $v_{rx} > a\omega$, then substituting Eq. 5.14 into Eq. 5.13 gives

$$\Gamma_{\mathrm{MC}} = \frac{K_r \delta^2 k a \omega}{2\pi^2} \tag{5.15}$$

Using the open-water dispersion relation to get ω and k from the peak frequency observed in the wave spectra $E(f)$, and the wave amplitude $a = \sqrt{2E}$, Γ_{MC} was estimated using the fast restoration case, for all of the field deployments, and at the buoys that were in the location of the MIZ where floe raft compaction was observed.

The errors on Γ_{MC} are based on the statistical errors on n, β, δ and a. They are

computed using the propagation of errors on Eq. 5.15:

$$d\Gamma_{\mathrm{MC}} = \left[\left(\frac{\partial \Gamma_{\mathrm{MC}}}{\partial n} dn \right)^2 + \left(\frac{\partial \Gamma_{\mathrm{MC}}}{\partial \beta} d\beta \right)^2 + \left(\frac{\partial \Gamma_{\mathrm{MC}}}{\partial \delta} d\delta \right)^2 + \left(\frac{\partial \Gamma_{\mathrm{MC}}}{\partial a} da^{\pm} \right)^2 \right]^{1/2} \tag{5.16}$$

i.e.

$$d\Gamma_{\mathrm{MC}} = \left[\left(\frac{dn}{1-n} \right)^2 + \left(\frac{2d\beta}{\cos\beta} \right)^2 + \left(\frac{2d\delta}{\delta} \right)^2 + \left(\frac{da^{\pm}}{a} \right)^2 \right]^{1/2} \tag{5.17}$$

The errors on n ($dn = 0.025$), β ($d\beta = 2°$), and δ ($d\delta/\delta = 30$ %) are taken from Sutherland and Dumont (2018). They represent respectively 4 %, 8 % and 60 % of relative error on Γ_{MC}. The error on a is computed directly from the error on E, leading to $da^{\pm}/a = \frac{1}{2}(\pm e^{\pm} \mp 1)$. It represents 20 % (-) and 50 % (+) of relative error on Γ_{MC}. After summation according to Eq. 5.17, the total relative errors on Γ_{MC} are 60 % (-) and 80 % (+).

As explained in Chapter 4, Γ_{w} is interpolated over the locations $x_{\mathrm{ice,MC}}$ at which Γ_{MC} is computed, for comparison between wave energy attenuation and energy dissipation due to floe raft compaction. The values of Γ_{MC} plotted in Fig. 5.5 are between 1 and 100 % of wave attenuation, within the uncertainties. It means that dissipation through friction during ice compaction is also a key component of wave attenuation in sea ice. In total, after averaging the energy dissipation due to compaction, over time and buoy location, for each data set, floe raft compaction can explain all of the wave energy attenuation for 4 deployment days out of 9. However, as noted for turbulence and collisions, this phenomenon does not always explain all of the wave attenuation.

5.2.3 Other wave attenuating floe-floe interactions

Some phenomena belonging to the category of floe-floe interactions could explain the rest of the wave attenuation observed during the BicWin campaigns. Though I did not study quantitatively these sources of energy dissipation during my PhD studies, they are possible paths to follow for future work.

Squire et al. (1995) mentions in particular the shear between floes, i.e. when two ice floes in contact perpendicularly to the wave direction move in the wave direction at different speeds, and friction is generated at the contact points. This phenomenon has been observed during the BicWin campaigns, and quantified in case of high ice concentration along with rafted floes using MC theory, but could also occur outside the scope of MC theory, for lower ice concentration, and without floe rafting. In this case, it would be necessary to separate the acceleration of the floes due to the wave orbital motion from the acceleration induced by the friction between floes. One way to do this would be to place SKIB buoys on at least two adjacent floes to visualize the events whose acceleration gradient is of the same magnitude but of opposite sign. Once the acceleration generated by the friction is identified, it would be sufficient to calculate the induced kinetic energy,

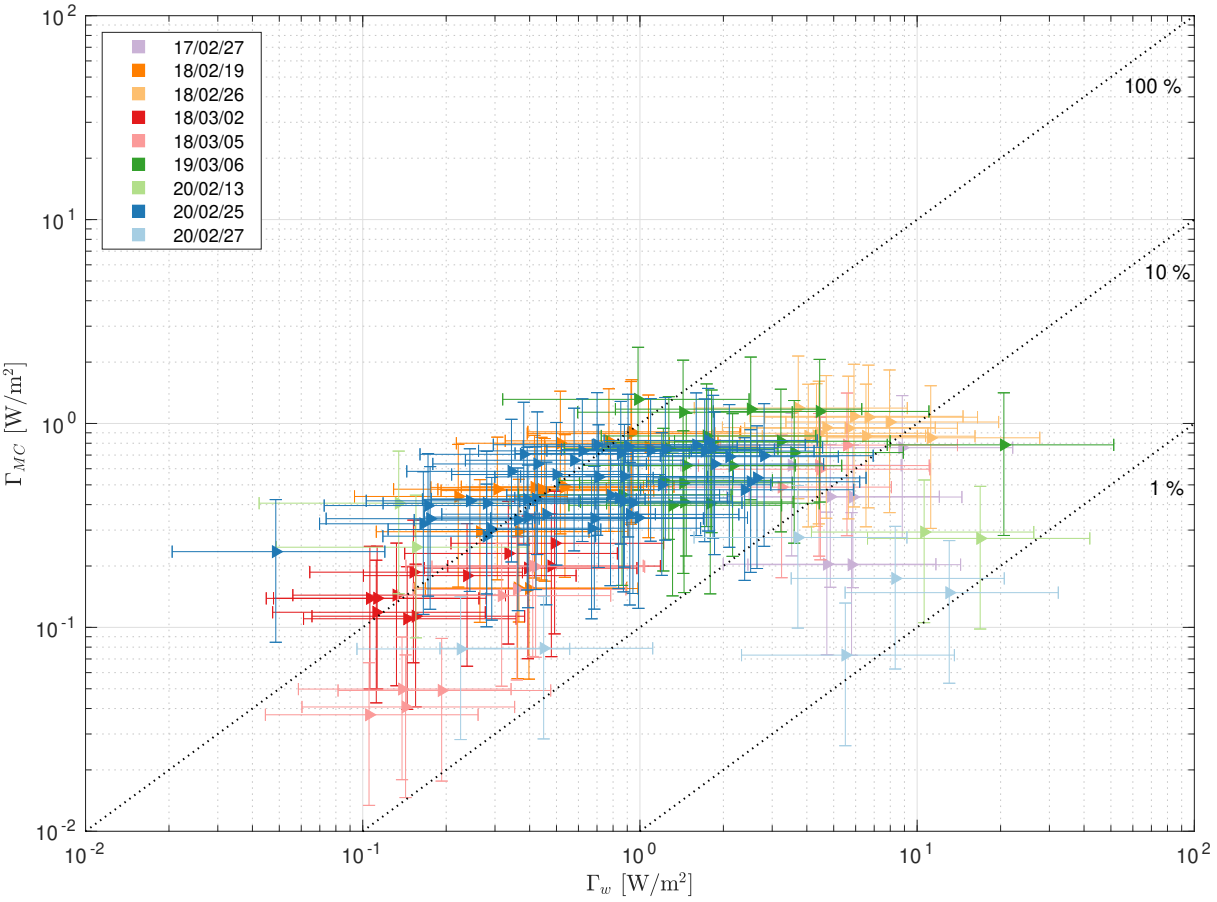

Figure 5.5 – Total floe compaction energy dissipation rate per unit of surface area, Γ_{MC}, plotted against the total wave attenuation rate per unit of surface area, Γ_w. Each symbol represents an average of the data over 10 minutes, and the colors represent the different data sets. The dashed lines are delimiting the areas over which more than 100 %, 10 % and 1 % of wave attenuation is due to floe compaction.

then the energy dissipation rate per unit area in the same way as for collisions.

Løken et al. (2022) mentions ice erosion under the impact of collisions, which dissipates energy, and adds brash ice and slush between floes, that will also participates in viscous energy dissipation in the slush (De Carolis et al., 2005; Rabault et al., 2017), and TKE dissipation under the ice (Rabault et al., 2019). The energy dissipated in the ice erosion is difficult to estimate. Using acceleration data from a high temporal resolution inertial motion unit with a extremely low noise level, it may be possible to identify in the collision signal a break in the slope just before the floe rebound, due to the energy dissipation generated by the erosion. Quantifying the viscous dissipation in the slush-brash mixture would require measuring its viscosity, as well as its spatial extension relative to the rest of the ice cover. Concerning turbulent dissipation, it would be necessary to make turbulence measurements with an ADCP under the ice between two floes without disturbing the collisions (for example with an Autonomous Underwater Vehicle) to obtain a TKE dissipation profile (Rabault et al., 2019). Some technical difficulties are to be considered in the execution of such a measurement. 1) The slush will block the ADCP signal, meaning that turbulence measurement would be restricted to below the slush layer. 2) The noise induced by side-lobe reflections of the signal on the wavy surface will be difficult to deal with. 3) The two floes would be frequently blocking the beam. Furthermore, it is very likely that this measurement is enhanced by wave advection of the turbulence generated by friction under the floes upstream of the measurement.

5.3 Wave attenuation and ice conditions

In the previous Chapters, I have discussed several phenomena leading to wave attenuation in the presence of sea ice. Here, I relate these results to the ice cover conditions encountered, and compare them to the literature.

First, for all of the deployments, the size of the ice floes was generally much smaller than the wavelength in the active area of the MIZ, meaning that no scattering nor ice flexure and break-up were expected, nor observed.

Then, in all of the cases where the ice concentration was close to one, the wave energy dissipation through turbulent processes under the ice remained below 10 % of total wave energy attenuation (see Fig. 5.6 and 5.7). In comparison, Voermans et al. (2019) obtained between 30 and 100 % of wave attenuation due to turbulence. The difference can probably be explained by differences in the ice cover, which was at the early stages of formation for Voermans et al. (2019) (frazil and pancake ice), with ice concentrations between 0.1 and 0.6. Low ice concentrations limits the possibility of floe-floe interactions, and since the floes in Voermans et al. (2019) study were much smaller than the wavelength, neither scattering nor ice flexion could occur, meaning that the wave energy could only be attenuated in the ocean layer through turbulent processes. However, it should be noted that for day

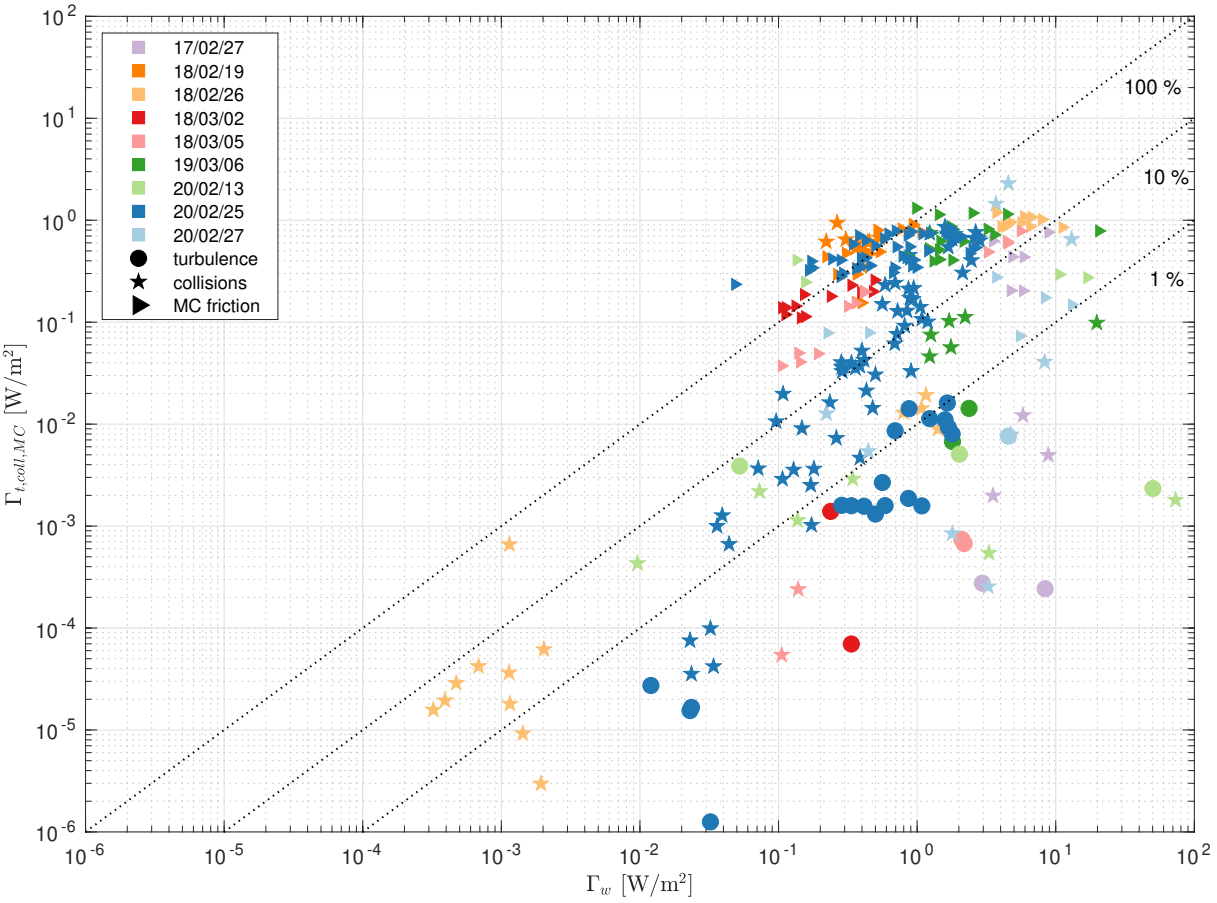

Figure 5.6 – Total TKE dissipation rate per unit of surface area without current effects (dots), total energy dissipation rate per unit of surface area due to floe collisions (stars) and total energy dissipation rate per unit of surface area due to floe compaction (triangles) plotted against the total wave attenuation rate per unit of surface area. Each symbol represents an average of the data over 10 minutes, and the colors represent the different data sets. The dashed lines are delimiting the areas over which more than 100 %, 10 % and 1 % of wave attenuation is due to either under-ice turbulence, floe collisions or floe compaction. The physical errors on the total TKE dissipation rate per unit of surface area are subtracted from the measurements. Data points are presented without error bars for better readability.

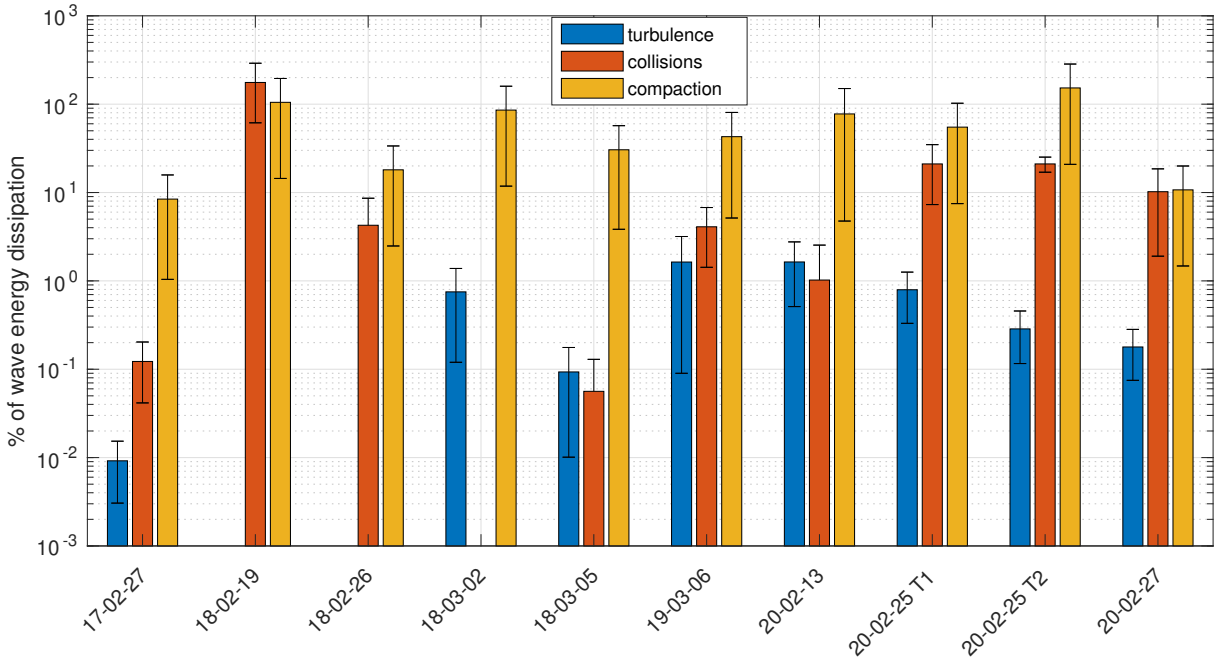

Figure 5.7 – Total TKE dissipation rate per unit of surface area (blue), total energy dissipation rate per unit of surface area due to floe collisions (orange) and total energy dissipation rate per unit of surface area due to floe compaction (yellow) divided by the total wave attenuation rate per unit of surface area. Each bar represents the percentage of wave energy dissipated by one of the above dissipation sources, averaged over a full data set.

2019-03-06 in the present work, where the ice concentration (0.4) was comparable to the ones in Voermans et al. (2019) study, the wave energy attenuation due to under ice turbulence remained below 10 %. The difference here might come from the definition of the ice concentration used in this work, based on the solid ice only, while on this day the large space between the floes was filled by slush, which would more likely dissipate wave energy through the compaction than turbulence. Hence, high floe concentrations, such as in the cases I encountered, induced floe-floe interactions that overtake under ice turbulence (see Fig. 5.6 and 5.7).

Between the two types of floe-floe interactions studied here, floe compaction seems to play a major role in most of the cases encountered, with more intense effect when floe rafting occurred. Floe collisions happen to be significant when the floes remained unrafted and more separated. The presence of slush and/or brash ice between the floes seems to dampen the collisions, compared to the cases where there was mostly sea water between the floes.

CONCLUSION

Summary of the thesis

In this manuscript, I presented collocated measurements of wave energy and under-ice turbulence that were undertaken during 9 deployments in natural laboratories of the Lower St. Lawrence Estuary. Incoming waves of peak frequency between 0.1 and 0.6 Hz, and significant wave height between 0.3 an 1.8 m were measured, using specially designed wave buoys, along their propagation in mostly highly concentrated MIZ. These MIZ were composed of floes with size much smaller than the wavelength and thickness between 0.3 and 1 m. In the meantime, the turbulence was measured in the water column within the first one to two meters under the ice, using one or two PCADPs inserted in holes near the center of ice floes.

The first part of this work, relative to Chapter 3, was focused on computing the waves statistics while they propagate through the sea ice covered ocean, and on estimating how much they are being attenuated along the propagation line. Wave omnidirectional frequency power spectra were computed integrated to obtain the wave energy as a function of the ice fetch. Exponential wave attenuation coefficients between 10^{-2} and 10^{-1} m^{-1} were observed. The wave energy attenuation rate per unit of sea surface area was computed as the spatial gradient of the wave energy flux in order to have a representative quantity of wave attenuation relative to the ice fetch. Values between 10^{-4} $W.m^{-2}$ (away from the ice edge) and 10 $W.m^{-2}$ (close from the ice edge) were obtained.

The second part, relative to Chapter 4, was dedicated to the evaluation of the turbulence in the water column under the ice, generated through wave-ice interactions. The measured under-ice water vertical velocities were first quality controlled, before the TKE dissipation rate was computed. Values between 10^{-7} and 10^{-4} $W.kg^{-1}$ were derived. Then, the total TKE dissipation rate per unit of sea surface area was computed by integrating the TKE dissipation rate in the water column under the ice, over an interval prescribed by the wall layer theory, and equivalent to the maximal range of the ADCPs. The physical errors on the total TKE dissipation rate per unit of sea surface area were investigated, involving current friction on sea bottom and current friction on the ice. It showed that, within the uncertainties, the modeled current friction could explain up to 100 % of the measured turbulence. After removing these errors, values of the TKE dissipation rate per unit of sea surface area possibly due to wave-ice interactions between 0 and 10^{-2} $W.m^{-2}$ were obtained, and compared to the total wave energy attenuation rate per unit of sea surface area. From this comparison, I showed that wave attenuation can not exclusively

be explained by turbulent processes in the water column under the ice, since less than 10 % of wave energy was dissipated by turbulence. The sources of under ice turbulence were discussed, and under the assumption that all of the turbulence related to wave-ice interactions was due to skin friction or form drag, ice-wave drag coefficients between 10^{-2} and 2×10^{-2} were obtained. The turbulent jet induced by the convergence of two neighbouring floes was modeled and confronted to the data, but was not able to match the TKE dissipation rate due to wave-ice interactions, reaching at best an insignificant 1 % of it.

The focus of the third part of this work, as detailed in Chapter 5, was to investigate the interactions between ice floes in order to understand how the majority of wave energy is dissipated, if not from under-ice turbulence. First, the study of collisions between ice floes was conducted by analyzing the acceleration data from the SKIB to calculate the transfer of kinetic energy between an ice floe and its neighboring floes during collisions. The energy calculated, which is equivalent to the energy of the waves dissipated due to the collisions, was used to determine the total energy dissipation rate per unit of sea surface area caused by collisions. It was found that this rate matched the wave energy dissipation rate per unit of sea surface area in some of the data sets, with values between 10^{-5} and 1 W.m^{-2}, accounting for between less than 1 % and 100 % of wave attenuation. Second, Mohr-Coulomb granular materials theory was used to estimate the energy dissipated in rafted ice floe compaction. The total energy dissipation rate per unit of sea surface area caused by floe compaction was computed as a function of the horizontal failure stress of the ice jumble, the ice thickness and the wave parameters, computed from the wave buoy measurements. Values between 10^{-2} and 1 W.m^{-2} were obtained, and explained between 1 % and 100 % of wave attenuation. Both result showed that, in case of highly concentrated MIZ of small floes relative to the wavelength, the major source of wave attenuation comes from floe-floe interactions. Combined or alone, floe collisions and multi-floe compaction allowed to explain at least 40 % of wave energy attenuation for 8 deployment days out of 9, and even 100 % of the attenuation for 5 of these days. However, the wave energy attenuation could not always be explained from the measurements of this work, and I suggested possible avenues to measure and analyse other floe-floe interactions such like floe-floe shear not attributable to floe raft compaction, viscous dissipation in the slush, and floe erosion due to collisions.

Dead ends, future work and a few personal considerations

This last section is the opportunity to deal with the dead ends encountered during this thesis, as well as with possible improvements and future work in the continuity of

what was discussed above.

Participation in the BicWin 2020 mission and the subsequent analysis of the data has provided me with some insights into field experimentation over the ice covered ocean. For example, the tedious process of discovering my turbulence measurement instrument, the S1000, in real conditions, made me realize the importance of being well prepared before the field experiments, by learning to handle the equipment beforehand. This observation is as true for the programming of the tool as for the understanding of the observed signals. A better preparation would have allowed, for example, to envisage a method to limit the noise induced by the reflection of the signal on the base of the ice.

It is necessary to take pictures of all the ice on which measuring devices are placed, because it regularly happens that there is no UAV image in the considered zones. In practice, it is not always easy to do all the desired manipulations when equipment is placed on the ice, because it is necessary to go quickly to have time to make all the measurements, and then return to land.

Turbulence was not important for wave attenuation in sea ice in the cases studied. However, this might not be always the case, as observed by Voermans et al. (2019) for lower ice concentration. And whatever the case, studying what causes under-ice turbulence is important for the understanding of the upper ocean mixing in ice covered conditions. Regarding turbulence measurements, it would be interesting to compare the S1000 measurements to measurements with higher temporal resolution, for example using an acoustic Doppler velocimeter. Such measurements could perhaps allow to calculate the TKE dissipation rate by the spectral method, while dealing with the signal of the waves thanks to a wider coverage of the inertial range. Indeed, other methods than the one of Scannell et al. (2017) have been tested in this perspective, using the S1000 data, such as filtering the velocity data with a high-pass filter, or using phase averaging methods, to remove the wave signal, without conclusive results.

The turbulence due to current friction on the ice appears to be important to quantify for a better estimation of under ice turbulence only due to wave ice interactions. Therefore, the use of instruments as the S1000s able to make measurements in both Doppler mode, along slanted beams to get the horizontal depth profile of current, and pulse-coherent mode, along the axis orthogonal to the sea surface to measure the turbulence in the water column, is to consider. Or, there should be at least one instrument dedicated to the measurement of the current velocity.

Turbulence measurements in stronger wave conditions, as during day 2020-02-27, but closer to the ice edge, could allow to get more turbulence responsible to wave energy dissipation. However, the ice canoe would be unadapted and unsafe to such conditions, and other solution could be investigated, as sending underwater rover from a ship place in the open water prior to the MIZ.

A part of this thesis was dedicated to the implementation of a wave model, based on

the BdHH, using WAVEWATCH III, to model the attenuation of waves in the wave and ice conditions encountered, and test parameterizations of this attenuation. This step could not be completed due to lack of time and some dead ends, but it is part of the possible avenues to follow in the continuity of this work. In particular, floe-floe interactions as floe collisions and multi-floe compaction are not yet implemented in wave-ice interactions models. Among them, the compaction phenomenon, that is described using MC theory, could not broadly be applied to the MIZs in current models, since the ice that is considered in such models is much more resistant to compression than the rafted floe observed in this work, for a similar thickness. This is thus another possible path to follow for future work on the topic.

Last, the presence of slush/frazil ice in between the floes and its effects on wave attenuation and on the other wave attenuation sources has been observed several times in this work without further investigations. Studying wave attenuation due to such ice would require more efforts, involving measurements of its rheological properties, and of its behaviour under compression.

Appendix A

Data

The purpose of this appendix is to present data from each BicWin deployment to complement the illustrative figures in the body of this manuscript. Tidal conditions during the experiments are shown, as well as maps showing the position of the various measuring instruments, the ice edge and wave direction for each deployment, and the wave spectra specific to each experiment. Please refer to Fig. 2.1 for the bathymetry of the bays and to Fig. 2.3 for the location of each deployment within the bays.

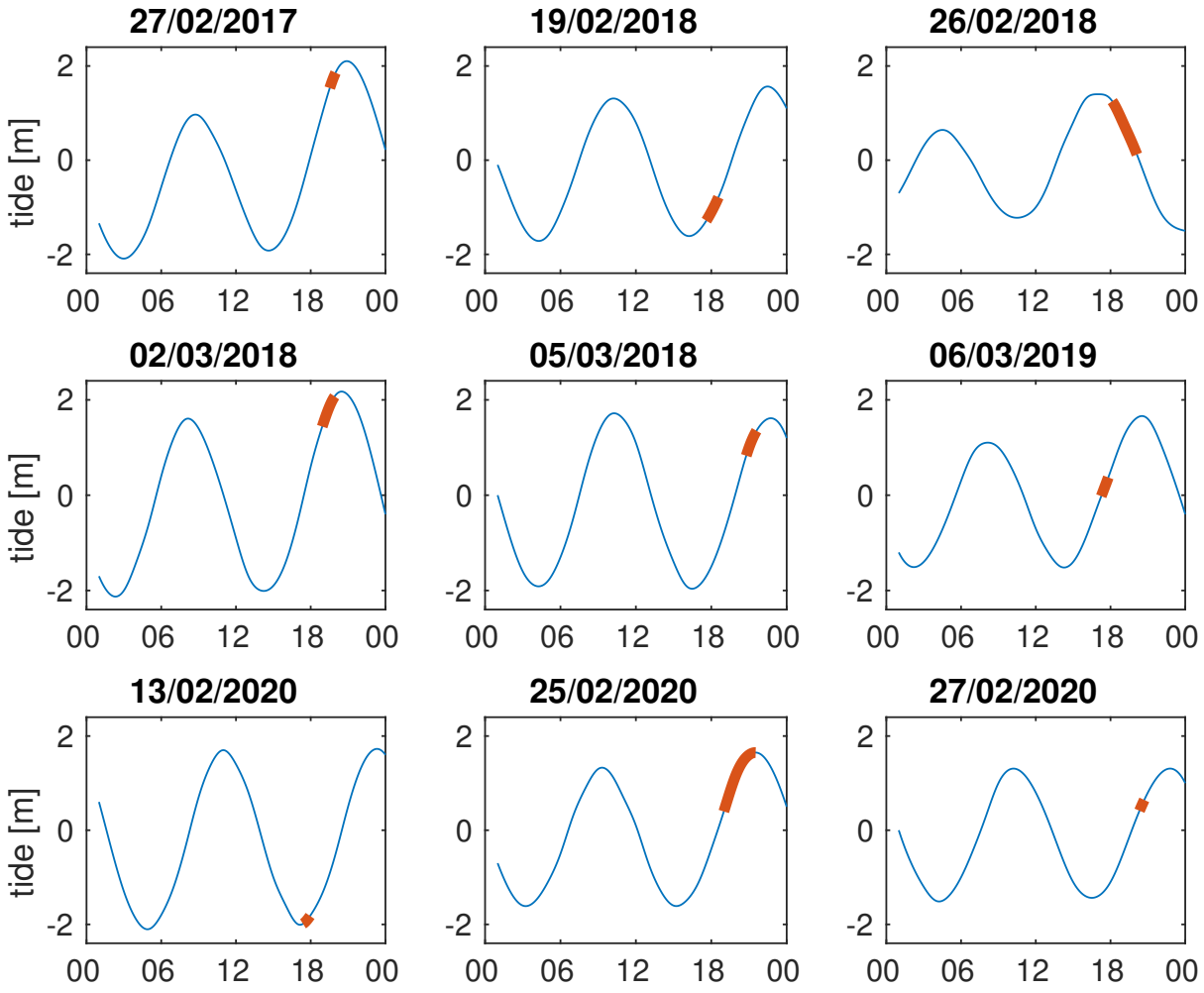

Figure A.1 – Time amplitude in mean sea level reference for each deployment day. The thin blue curve represents the tide during the entire day from 00:00 UTC to 24:00 UTC, and the thick red curve is the tide during each full deployment.

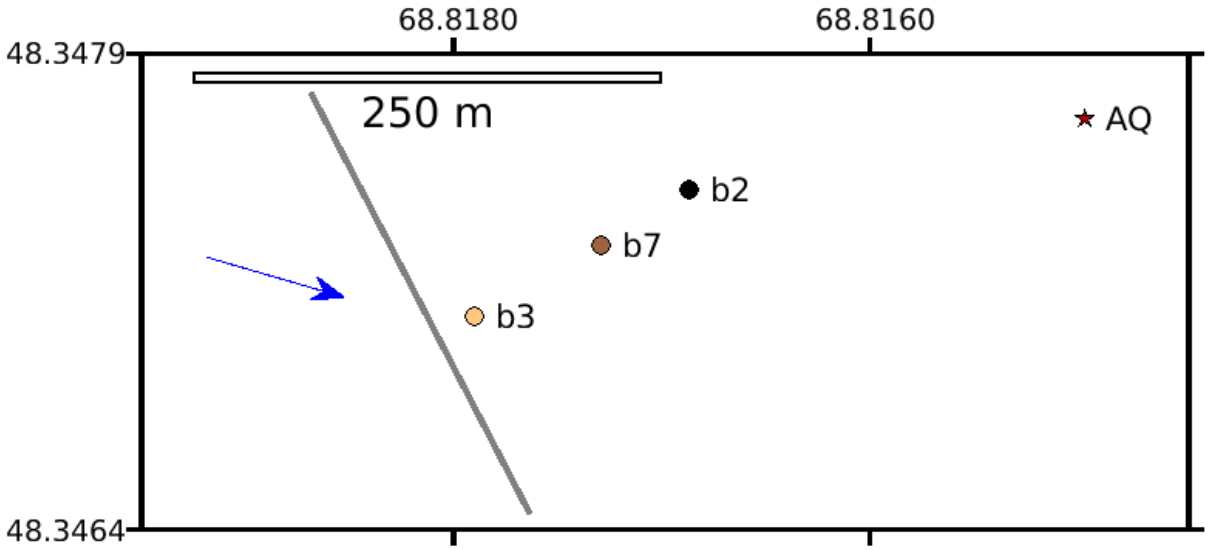

Figure A.2 – Map of the deployment for day 2017-02-27. The average location of each buoy, over the full deployment, is numbered and represented with a circle filled with a color from yellow (close to the ice edge) to black (far from the ice edge). The red star (AQ) represents the location of the Aquadopp HR profiler. The thick gray line is the ice edge, and the blue arrow represents the mean wave direction during the full duration of the deployment.

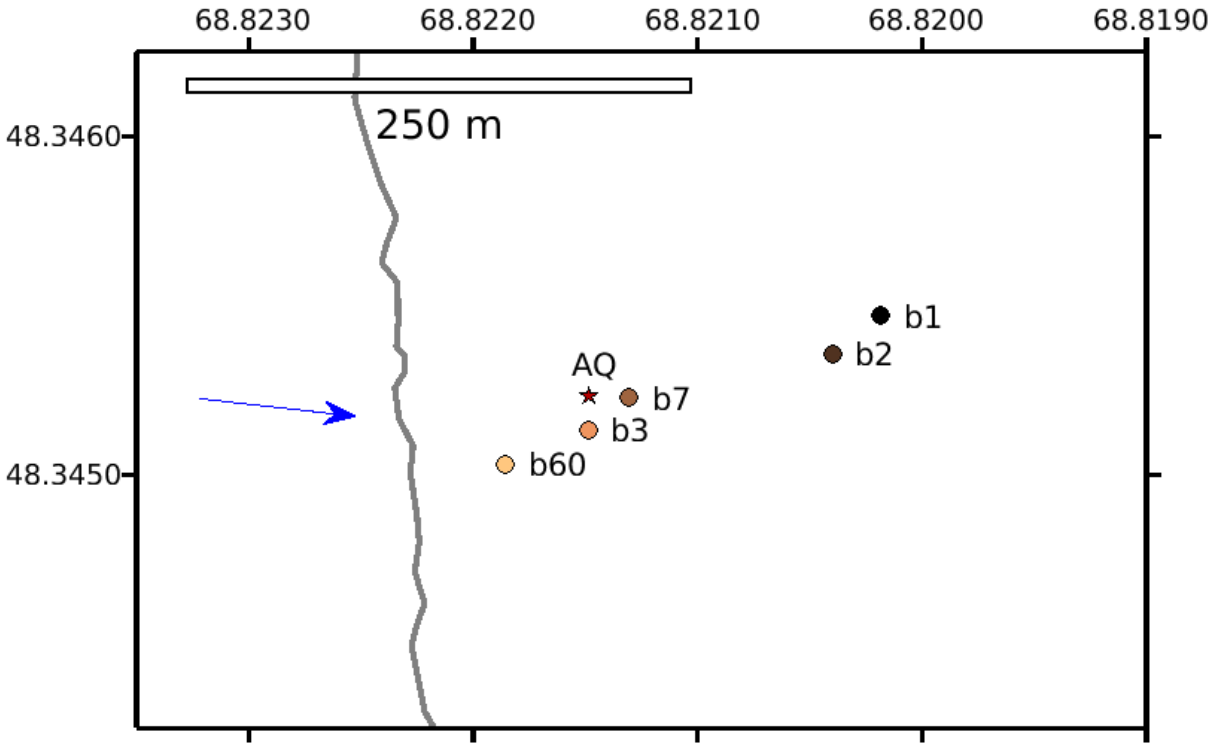

Figure A.3 – Map of the deployment for day 2018-02-19. The average location of each buoy, over the full deployment, is numbered and represented with a circle filled with a color from yellow (close to the ice edge) to black (far from the ice edge). The red star (AQ) represents the location of the Aquadopp HR profiler. The thick gray line is the ice edge, and the blue arrow represents the mean wave direction during the full duration of the deployment.

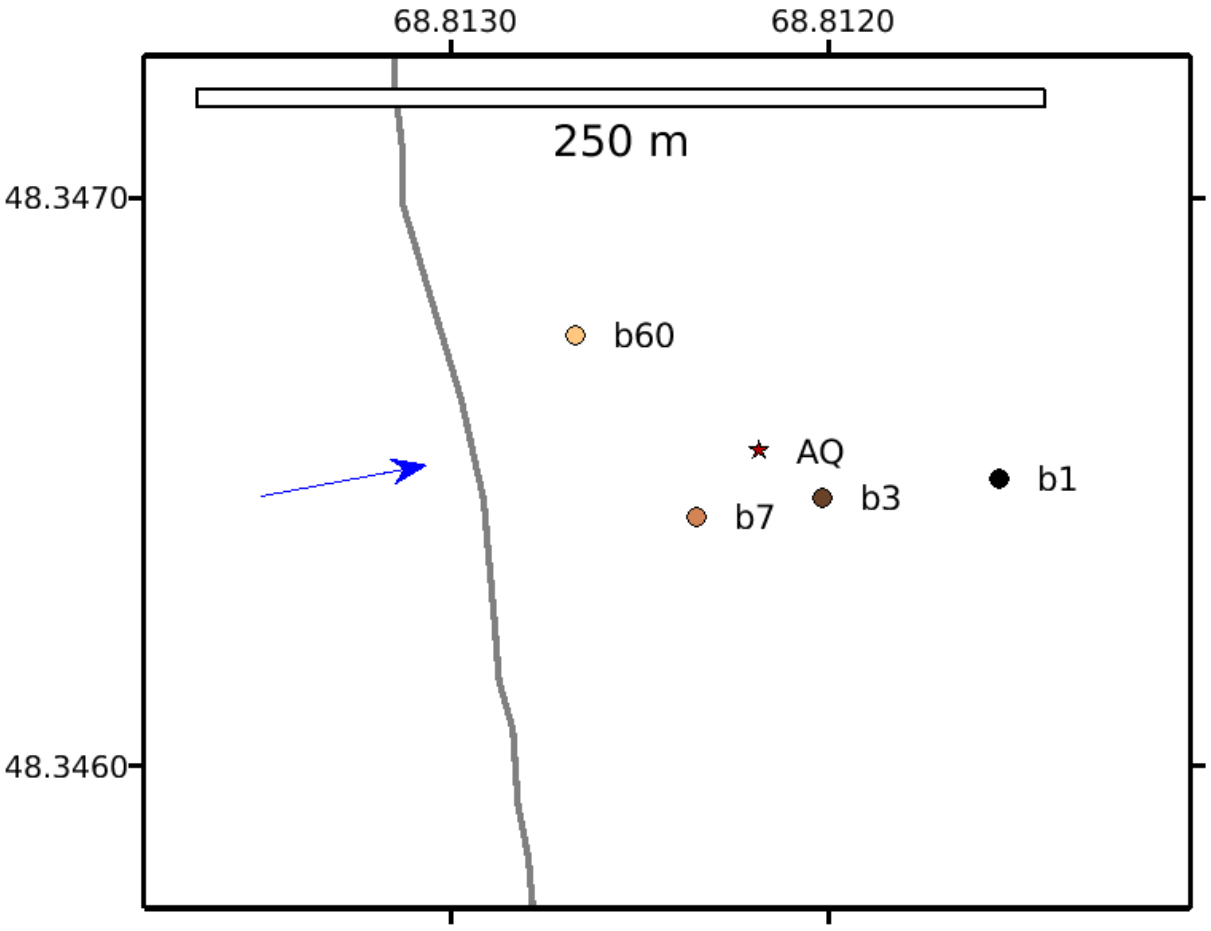

Figure A.4 – Map of the deployment for day 2018-02-26. The average location of each buoy, over the full deployment, is numbered and represented with a circle filled with a color from yellow (close to the ice edge) to black (far from the ice edge). The red star (AQ) represents the location of the Aquadopp HR profiler. The thick gray line is the ice edge, and the blue arrow represents the mean wave direction during the full duration of the deployment.

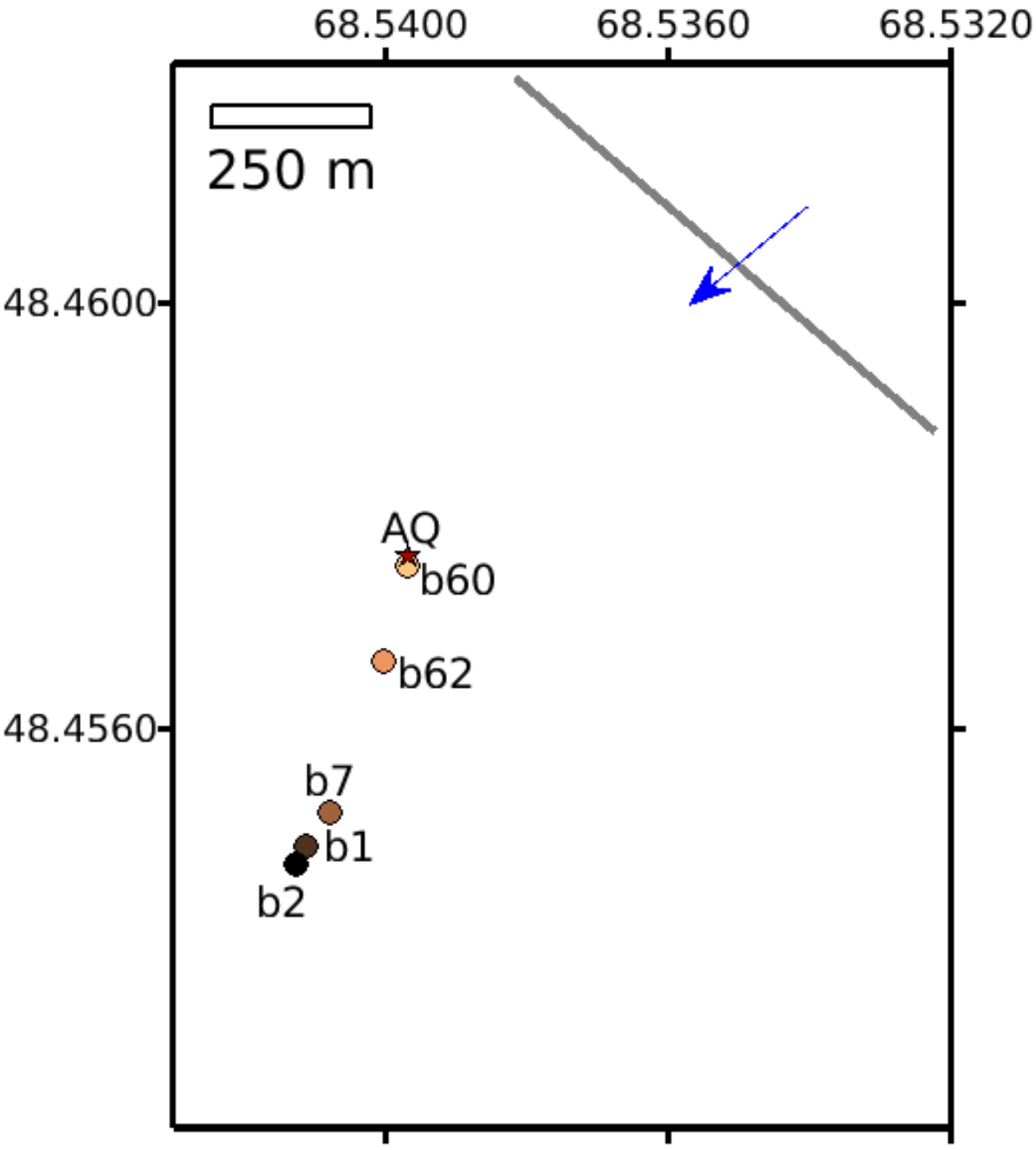

Figure A.5 – Map of the deployment for day 2018-03-02. The average location of each buoy, over the full deployment, is numbered and represented with a circle filled with a color from yellow (close to the ice edge) to black (far from the ice edge). The red star (AQ) represents the location of the Aquadopp HR profiler. The thick gray line is the ice edge, and the blue arrow represents the mean wave direction during the full duration of the deployment.

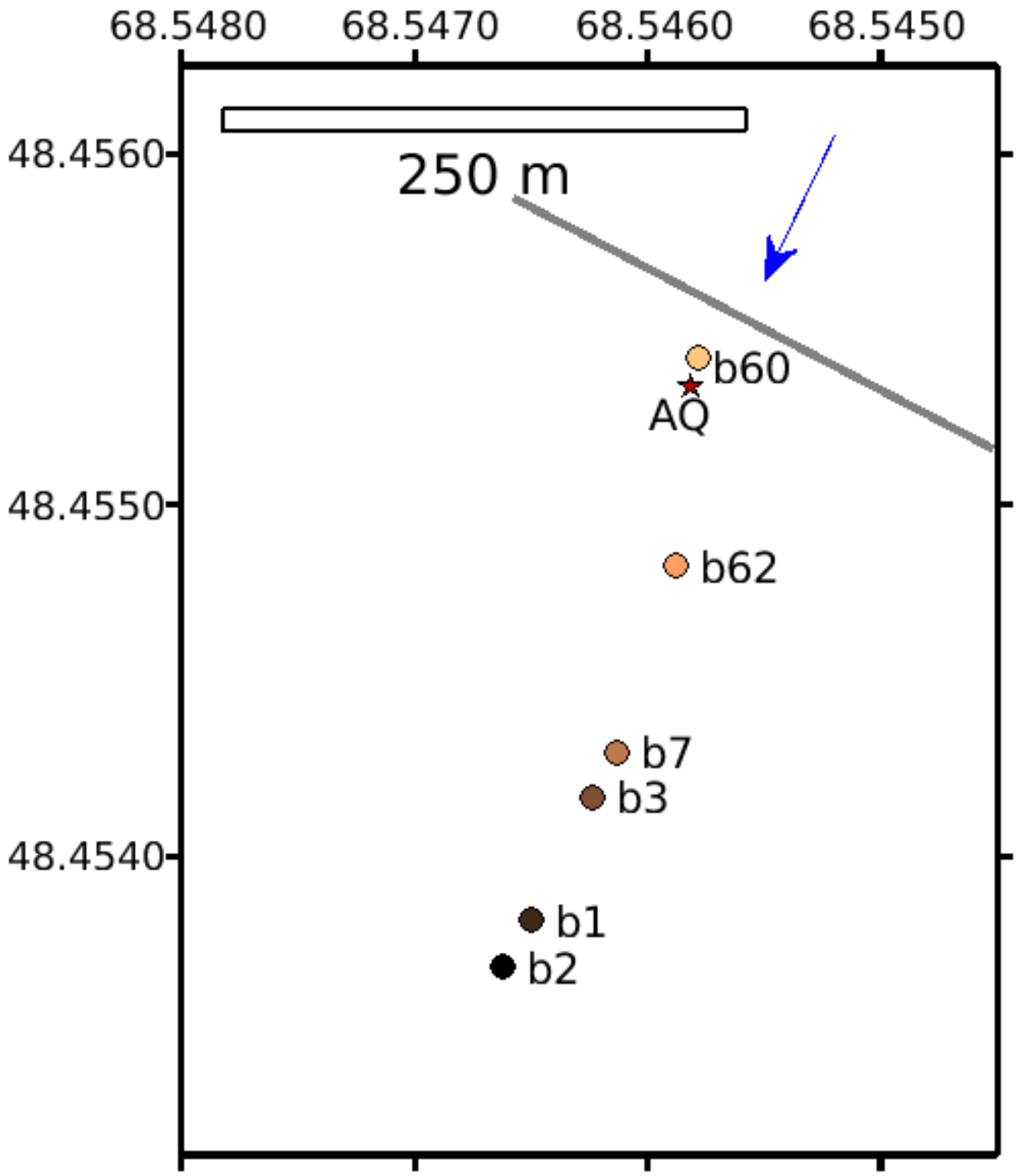

Figure A.6 – Map of the deployment for day 2018-03-05. The average location of each buoy, over the full deployment, is numbered and represented with a circle filled with a color from yellow (close to the ice edge) to black (far from the ice edge). The red star (AQ) represents the location of the Aquadopp HR profiler. The thick gray line is the ice edge, and the blue arrow represents the mean wave direction during the full duration of the deployment.

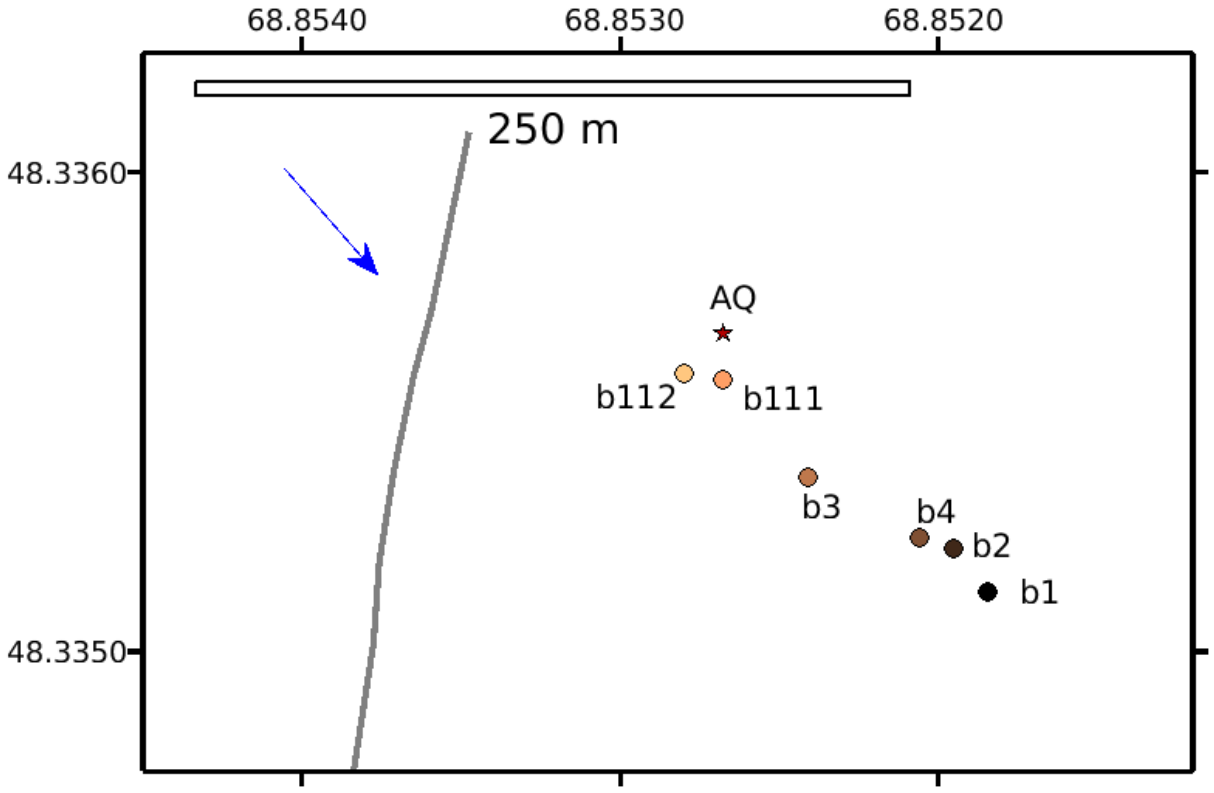

Figure A.7 – Map of the deployment for day 2019-03-06. The average location of each buoy, over the full deployment, is numbered and represented with a circle filled with a color from yellow (close to the ice edge) to black (far from the ice edge). The red star (AQ) represents the location of the Aquadopp HR profiler. The thick gray line is the ice edge, and the blue arrow represents the mean wave direction during the full duration of the deployment.

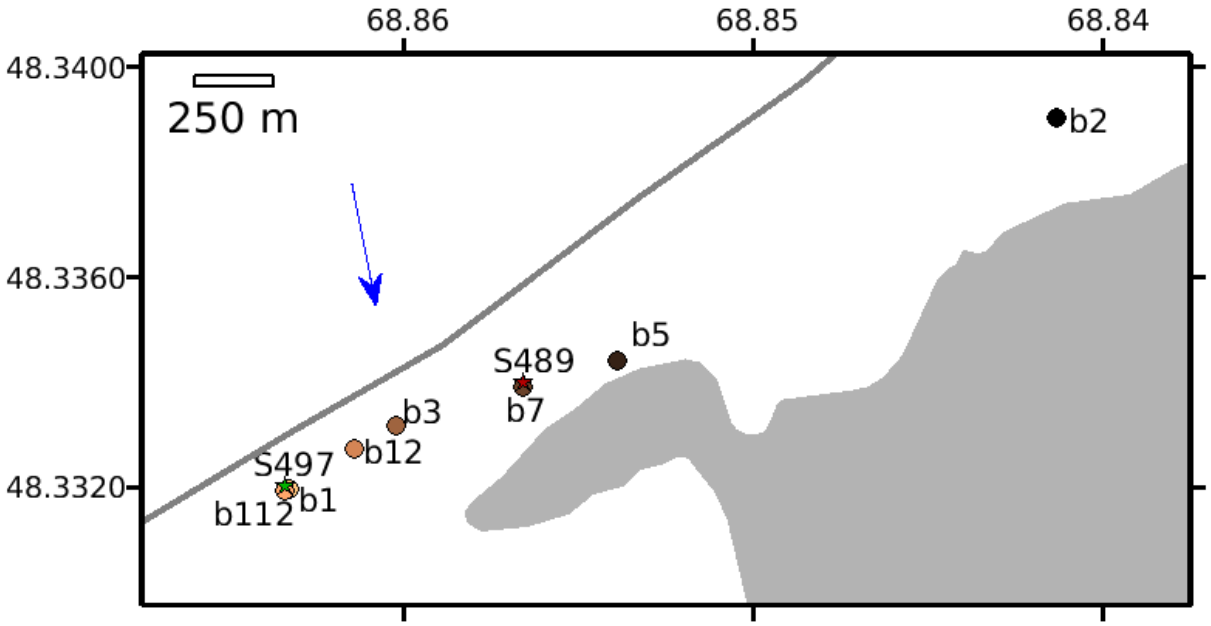

Figure A.8 – Map of the deployment for day 2020-02-13. The average location of each buoy, over the full deployment, is numbered and represented with a circle filled with a color from yellow (close to the ice edge) to black (far from the ice edge). The red star represents the location of the Signature S489 and the green star the location of the Signature S497. The thick gray line is the ice edge, and the blue arrow represents the mean wave direction during the full duration of the deployment.

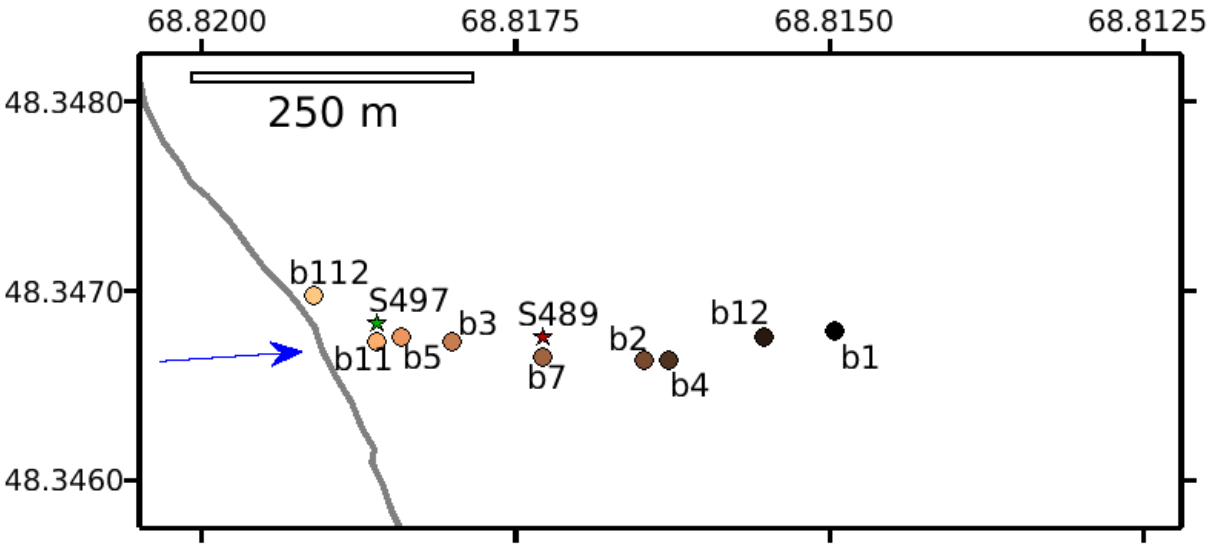

Figure A.9 – Map of the deployment for day 2020-02-25. The average location of each buoy, over the full deployment, is numbered and represented with a circle filled with a color from yellow (close to the ice edge) to black (far from the ice edge). The red star represents the location of the Signature S489 and the green star the location of the Signature S497. The thick gray line is the ice edge, and the blue arrow represents the mean wave direction during the full duration of the deployment.

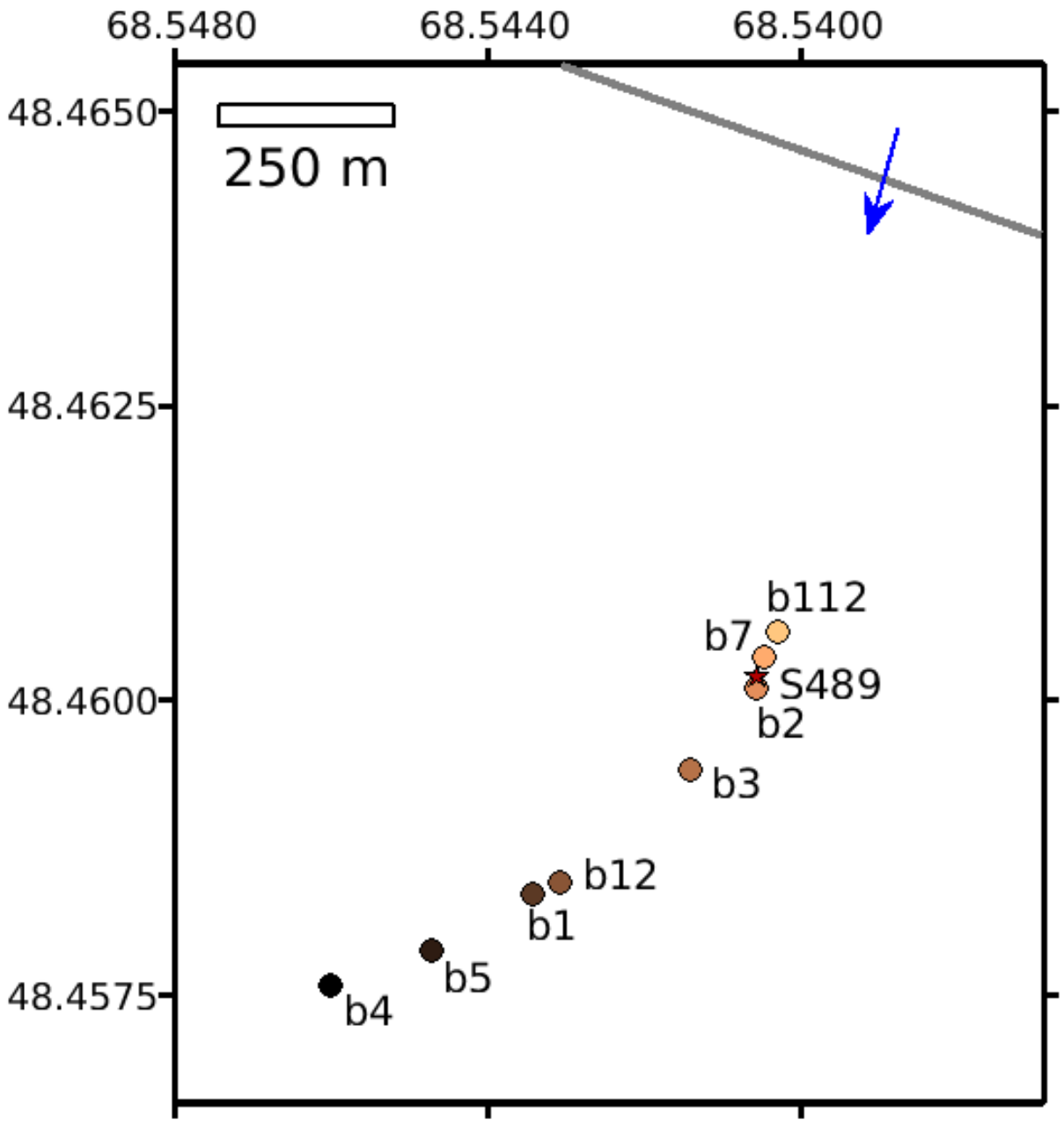

Figure A.10 – Map of the deployment for day 2020-02-27. The average location of each buoy, over the full deployment, is numbered and represented with a circle filled with a color from yellow (close to the ice edge) to black (far from the ice edge). The red star represents the location of the Signature S489. The thick gray line is the ice edge, and the blue arrow represents the mean wave direction during the full duration of the deployment.

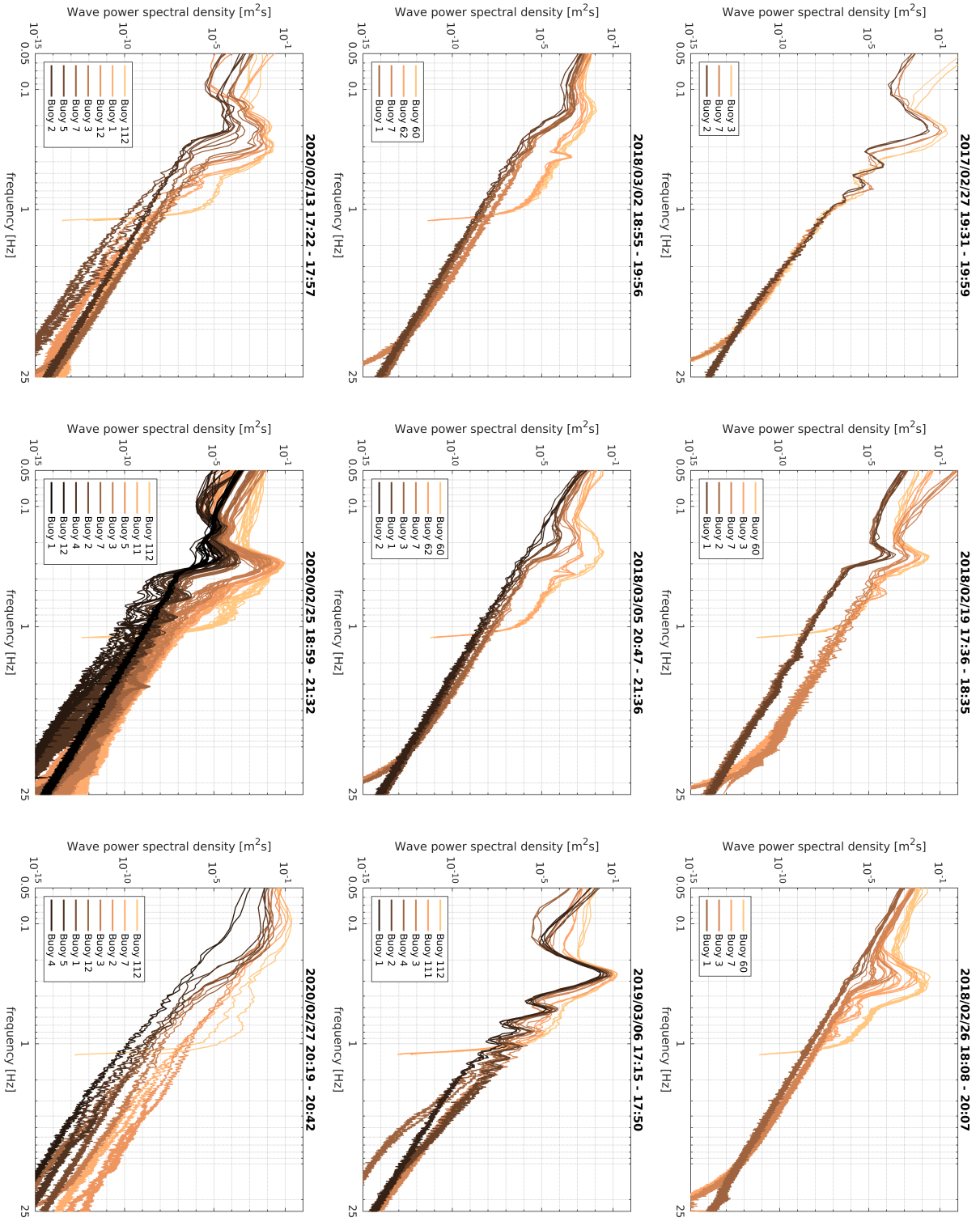

Figure A.11 – Wave energy spectra in the MIZ as a function of frequency for all 10-min intervals of all data sets between 2017 and 2020. Each color corresponds to one buoy number, the lighter the color the closer the buoy is to the ice edge. These colors correspond to the colors of each deployment map in Fig. A.2 to A.10.

BIBLIOGRAPHY

Airy, G. B., 1841: Tides and waves. encyclopaedia metropolitana (1817–1845). *Mixed Sciences, edited by HJ Rose*, **3**.

Andersen, T. J., J. Fredsoe, and M. Pejrup, 2007: In situ estimation of erosion and deposition thresholds by Acoustic Doppler Velocimeter (ADV). *Estuarine, Coastal and Shelf Science*, **75 (3)**, 327–336, doi: 10.1016/j.ecss.2007.04.039.

Ardhuin, F., and J.-F. Filipot, 2019: *Ocean waves in Geosciences*. Brest, 276 pp., doi: 10.13140/RG.2.2.16019.78888/5.

Ardhuin, F., P. Sutherland, M. Doble, and P. Wadhams, 2016: Ocean waves across the Arctic: Attenuation due to dissipation dominates over scattering for periods longer than 19 s. *Geophysical Research Letters*, **43**, 5775–5783, doi: 10.1002/2016GL068204.

Barton, B. I., Y.-D. Lenn, and C. Lique, 2018: Observed Atlantification of the Barents Sea Causes the Polar Front to Limit the Expansion of Winter Sea Ice. *Journal of Physical Oceanography*, **48 (8)**, 1849–1866, doi: 10.1175/JPO-D-18-0003.1, URL http://journals.ametsoc.org/doi/10.1175/JPO-D-18-0003.1.

Bendat, J. S., and A. G. Piersol, 1987: *Random Data - Analysis and Measurement Procedures*, Vol. 729. John Wiley & Son, 619 pp., doi: 10.2307/2289430.

Boutin, G., F. Ardhuin, D. Dumont, C. Sévigny, F. Girard-Ardhuin, and M. Accensi, 2018: Floe Size Effect on Wave-Ice Interactions: Possible Effects, Implementation in Wave Model, and Evaluation. *Journal of Geophysical Research: Oceans*, **123 (7)**, 4779–4805, doi: 10.1029/2017JC013622.

Cole, D. M., 1998: Modeling the cyclic loading response of sea ice. *International Journal of Solids and Structures*, **35 (31-32)**, 4067–4075, doi: 10.1016/S0020-7683(97)00301-6, URL http://dx.doi.org/10.1016/S0020-7683(97)00301-6.

Dai, M., H. H. Shen, M. A. Hopkins, and S. F. Ackley, 2004: Wave rafting and the equilibrium pancake ice cover thickness. *Journal of Geophysical Research: Oceans*, **109 (7)**, 1–9, doi: 10.1029/2003JC002192.

Davis, P. E. D., C. Lique, H. L. Johnson, and J. D. Guthrie, 2016: Competing Effects of Elevated Vertical Mixing and Increased Freshwater Input on the Stratification and Sea Ice Cover in a Changing Arctic Ocean. *Journal of Physical Oceanography*, doi: 10.1175/JPO-D-15-0174.1.

De Carolis, G., and D. Desiderio, 2002: Dispersion and attenuation of gravity waves in ice: A two-layer viscous fluid model with experimental data validation. *Physics Letters, Section A: General, Atomic and Solid State Physics*, **305 (6)**, 399–412, doi: 10.1016/S0375-9601(02)01503-7.

De Carolis, G., P. Olla, and L. Pignagnoli, 2005: Effective viscosity of grease ice in linearized gravity waves. *Journal of Fluid Mechanics*, **535**, 369–381, doi: 10.1017/S002211200500474X.

Doble, M. J., M. D. Coon, and P. Wadhams, 2003: Pancake ice formation in the Weddell Sea. *Journal of Geophysical Research C: Oceans*, **108 (7)**, 2–1, doi: 10.1029/2002jc001373.

Dumont, D., 2022: Marginal ice zone dynamics: History, definitions and research perspectives. *Philosophical Transactions of the Royal Society A: Mathematical, Physical and Engineering Sciences*, **380 (2235)**, doi: 10.1098/rsta.2021.0253.

Dumont, D., A. L. Kohout, and L. Bertino, 2011: A wave-based model for the marginal ice zone including a floe breaking parameterization. *Journal of Geophysical Research: Oceans*, **116 (4)**, 1–12, doi: 10.1029/2010JC006682.

Fer, I., T. M. Baumann, Z. Koenig, M. Muilwijk, and S. Tippenhauer, 2022: Upper-Ocean Turbulence Structure and Ocean-Ice Drag Coefficient Estimates Using an Ascending Microstructure Profiler During the MOSAiC Drift. *Journal of Geophysical Research: Oceans*, **127 (9)**, 1–23, doi: 10.1029/2022jc018751.

Gebhardt, C., J. R. Bidlot, J. Gemmrich, S. Lehner, A. Pleskachevsky, and W. Rosenthal, 2016: Wave observation in the marginal ice zone with the TerraSAR-X satellite. *Ocean Dynamics*, **66 (6-7)**, 839–852, doi: 10.1007/s10236-016-0957-8, URL http://dx.doi.org/10.1007/s10236-016-0957-8.

Gemmrich, J., and D. M. Farmer, 2004: Near-Surface Turbulence in the Presence of Breaking Waves. *Journal of Physical Oceanography*, **34 (5)**, 1067–1086, doi: https://doi.org/10.1175/1520-0485(2004)034<1067:NTITPO>2.0.CO;2.

Gerbi, G. P., 2008: Observations of turbulent fluxes and turbulence dynamics in the ocean surface boundary layer. Ph.D. thesis, MIT and WHOI, doi: 10.1575/1912/2321.

Guimarães, P. V., and Coauthors, 2018: A surface kinematics buoy (SKIB) for wave-current interaction studies. *Ocean Science*, **14 (6)**, 1449–1460, doi: 10.5194/os-14-1449-2018.

Hasselmann, K., and Coauthors, 1973: Measurements of Wind-Wave Growth and Swell Decay during the Joint North Sea Wave Project (JONSWAP). *Ergnzungsheft zur Deutschen Hydrographischen Zeitschrift Reihe*, **A(8) (8 0)**, p.95, doi: citeulike-article-id:2710264.

Herbers, T. H. C., P. F. Jessen, T. T. Janssen, D. B. Colbert, and J. H. MacMahan, 2012: Observing ocean surface waves with GPS-tracked buoys. *Journal of Atmospheric and Oceanic Technology*, **29 (7)**, 944–959, doi: 10.1175/JTECH-D-11-00128.1.

Herman, A., 2021: Spectral Wave Energy Dissipation due to Under-Ice Turbulence. *Journal of Physical Oceanography*, **51 (4)**, 1177–1186, doi: 10.1175/jpo-d-20-0171.1.

Herman, A., S. Cheng, and H. H. Shen, 2019: Wave energy attenuation in fields of colliding ice floes – Part 2: A laboratory case study. *The CryosphereCryosphere*, **13 (11)**, 2901–2914, doi: 10.5194/tc-13-2901-2019.

Holthuijsen, L. H., 2007: *Waves in Oceanic and Coastal Waters*. 1–405 pp., URL www.cambridge.org/9780521860284.

Hopkins, M. A., and J. Tuhkuri, 1999: Compression of floating ice fields. *Journal of Geophysical Research: Oceans*, **104 (C7)**, 15 815–15 825, doi: 10.1029/1999jc900127.

Jackett, D. R., T. J. McDougall, R. Feistel, D. G. Wright, and S. M. Griffies, 2006: Algorithms for density, potential temperature, conservative temperature, and the freezing temperature of seawater. *Journal of Atmospheric and Oceanic Technology*, **23 (12)**, 1709–1728, doi: 10.1175/JTECH1946.1.

Jackson, L. C., A. Biastoch, M. W. Buckley, D. G. Desbruyères, E. Frajka-Williams, B. Moat, and J. Robson, 2022: The evolution of the North Atlantic Meridional Overturning Circulation since 1980. *Nature Reviews Earth and Environment*, **3 (4)**, 241–254, doi: 10.1038/s43017-022-00263-2.

Kohout, A. L., and M. H. Meylan, 2008: An elastic plate model for wave attenuation and ice floe breaking in the marginal ice zone. *Journal of Geophysical Research: Oceans*, **113 (9)**, 1–17, doi: 10.1029/2007JC004434.

Kohout, A. L., M. H. Meylan, and D. R. Plew, 2011: Wave attenuation in a marginal ice zone due to the bottom roughness of ice floes. *Annals of Glaciology*, doi: 10.3189/172756411795931525.

Kolmogorov, A. N., 1991: The local structure of turbulence in incompressible viscous fluid for very large Reynolds numbers. *Proceedings of the Royal Society of London. Series A: Mathematical and Physical Sciences*, Vol. 434, 9–13.

Komen, G. J., L. Cavaleri, M. Donelan, K. Hasselmann, S. Hasselmann, and P. A. E. M. Janssen, 1994: *Dynamics and Modelling of Ocean Waves*. Cambridge University Press, Cambridge, UK, 554 pp.

Lacy, J. R., and C. R. Sherwood, 2004: Accuracy of a pulse-coherent acoustic Doppler profiler in a wave-dominated flow. *Journal of Atmospheric and Oceanic Technology*, **21**, 1448–1461, doi: 10.1175/1520-0426(2004)021<1448:AOAPAD>2.0.CO;2.

Li, H., and R. Lubbad, 2018: Laboratory study of ice floes collisions under wave action. *Proceedings of the International Offshore and Polar Engineering Conference*, **2018-June**, 1516–1524.

Lique, C., H. L. Johnson, and Y. Plancherel, 2018: Emergence of deep convection in the Arctic Ocean under a warming climate. *Climate Dynamics*, **50 (9-10)**, 3833–3847, doi: 10.1007/s00382-017-3849-9.

Liu, A. K., B. Holt, and P. W. Vachon, 1991: Wave propagation in the marginal ice zone: model predictions and comparisons with buoy and synthetic aperture radar data. *Journal of Geophysical Research*, **96 (C3)**, 4605–4621, doi: 10.1029/90JC02267.

Liu, A. K., and E. Mollo-Christensen, 1988: Wave propagation in a solid ice pack. *Journal of Physical Oceanography*, **18**, 1702–1712, doi: 10.1175/1520-0485(1988)018<1702:WPIASI>2.0.CO;2.

Løken, T. K., A. Marchenko, T. J. Ellevold, J. Rabault, and A. Jensen, 2022: Experiments on turbulence from colliding ice floes. *Physics of Fluids*, **34 (6)**, 065 133, doi: 10.1063/5.0088953.

Longuet-Higgins, M. S., D. E. Cartwright, and N. D. Smith, 1963: Observations of the Directional Spectrum of Sea Waves using the Motions of a Floating Buoy. *Ocean Wave Spectra*, Easton, 111–132.

Longuet-Higgins, M. S., and R. W. Stewart, 1964: Radiation stresses in water waves; a physical discussion, with applications. *Deep-Sea Research and Oceanographic Abstracts*, **11 (4)**, 529–562.

Lu, P., Z. Li, B. Cheng, and M. Leppäranta, 2011: A parameterization of the ice-ocean drag coefficient. *Journal of Geophysical Research: Oceans*, **116 (7)**, 1–14, doi: 10.1029/2010JC006878.

Maksym, T., 2019: Arctic and Antarctic Sea Ice Change: Contrasts, Commonalities, and Causes. *Annual Review of Marine Science*, **11 (1)**, 187–213, doi: 10.1146/annurev-marine-010816-060610.

Martin, S., and P. Kauffman, 1981: A Field and Laboratory Study of Wave Damping by Grease Ice. *Journal of Glaciology*, **27 (96)**, 283–313, doi: 10.3189/s0022143000015392.

MathWorks®, 2020: *MATLAB® Function Reference (R2020b)*. MathWorks®.

MathWorks®, 2022a: *Signal Processing Toolbox™ Reference (R2022b)*. MathWorks®.

MathWorks®, 2022b: *Statistics and Machine Learning Toolbox ™ User's Guide (R2022b)*. MathWorks®.

Meylan, M. H., L. G. Bennetts, J. E. Mosig, W. E. Rogers, M. J. Doble, and M. A. Peter, 2018: Dispersion relations, power laws, and energy loss for waves in the marginal ice zone. *Journal of Geophysical Research: Oceans*, **123 (5)**, 3322–3335, doi: 10.1002/2018JC013776.

Meylan, M. H., and V. A. Squire, 1996: Response of a circular ice floe to ocean waves. *Journal of Geophysical Research: Oceans*, **101 (C4)**, 8869–8884, doi: 10.1029/95JC03706.

Otsu, N., 1979: A threshold selection method from gray-level histograms. *IEEE Trans. on Systems, Man and Cybernetics*, **9 (1)**, 62–66.

Overland, J. E., and M. Wang, 2013: When will the summer Arctic be nearly sea ice free? *Geophysical Research Letters*, **40 (10)**, 2097–2101, doi: 10.1002/grl.50316.

Pope, S. B., 2000: *Turbulent Flows*. Cambridge University Press, 1–807 pp., doi: 10.1088/0957-0233/12/11/705.

Rabault, J., G. Sutherland, O. Gundersen, and A. Jensen, 2017: Measurements of wave damping by a grease ice slick in Svalbard using off-the-shelf sensors and open-source electronics. *Journal of Glaciology*, **63 (238)**, 372–381, doi: 10.1017/jog.2017.1.

Rabault, J., G. Sutherland, A. Jensen, K. H. Christensen, and A. Marchenko, 2019: Experiments on wave propagation in grease ice: combined wave gauges and PIV measurements. *Journal of Fluid Mechanics*, **864**, 876–898, doi: 10.1017/jfm.2019.16.

Rantanen, M., A. Y. Karpechko, A. Lipponen, K. Ruosteenoja, T. Vihma, A. Laaksonen, K. Nordling, and O. Hyvärinen, 2022: The Arctic has warmed nearly four times faster than the globe since 1979. *Communications Earth and Environment*, **3 (1)**, 1–10, doi: 10.1038/s43247-022-00498-3.

Roach, L. A., M. M. Smith, and S. M. Dean, 2018: Quantifying Growth of Pancake Sea Ice Floes Using Images From Drifting Buoys. *Journal of Geophysical Research: Oceans*, **123 (4)**, 2851–2866, doi: 10.1002/2017JC013693.

Robin, G. d. Q., 1963a: Ocean waves and pack ice. *Polar Record*, **11 (73)**, 389–393, doi: 10.1017/S003224740005350X.

Robin, G. d. Q., 1963b: Wave Propagation Through Fields Of Pack Ice. *Philosophical Transactions of the Royal Society of London*, **255 (1057)**, 313–339.

Rusello, P. J., 2009: A practical primer for pulse coherent instruments. Tech. rep., Nortek, 1–17 pp. doi: 10.1016/S0123-9392(10)70090-4.

Saddoughi, S. G., and S. V. Veeravalli, 1994: Local isotropy in turbulent boundary layers at high Reynolds number. *Journal of Fluid Mechanics*, **268**, 333–372.

Saucier, F. J., F. Roy, D. Gilbert, P. Pellerin, and H. Ritchie, 2003: Modeling the formation and circulation processes of water masses and sea ice in the Gulf of St. Lawrence, Canada. *Journal of Geophysical Research*, **108 (C8)**, 1–20, doi: 10.1029/2000jc000686.

Scannell, B. D., T. P. Rippeth, J. H. Simpson, J. A. Polton, and J. E. Hopkins, 2017: Correcting surface wave bias in structure function estimates of turbulent kinetic energy dissipation rate. *Journal of Atmospheric and Oceanic Technology*, **34 (10)**, 2257–2273, doi: 10.1175/JTECH-D-17-0059.1.

Sévellec, F., A. V. Fedorov, and W. Liu, 2017: Arctic sea-ice decline weakens the Atlantic Meridional Overturning Circulation. *Nature Climate Change*, **7 (8)**, 604–610, doi: 10.1038/NCLIMATE3353.

Skene, D. M., L. G. Bennetts, M. H. Meylan, and A. Toffoli, 2015: Modelling water wave overwash of a thin floating plate. *Journal of Fluid Mechanics*, **777**, 1–13, doi: 10.1017/jfm.2015.378.

Smith, M. M., and Coauthors, 2018: Episodic reversal of autumn ice advance caused by release of ocean heat in the beaufort sea. *Journal of Geophysical Research: Oceans*, **123 (5)**, 3164–3185, doi: 10.1002/2018JC013764.

Soille, P., 1999: *Morphological Image Analysis*. Springer Berlin, Heidelberg, doi: 10.1007/978-3-662-03939-7.

Soulsby, R., 1997: *Dynamics of Marine Sands: A Manual for Practical Applications*.

Soulsby, R. L., 1983: The bottom boundary layer of shelf seas. *Elsevier Oceanography Series*, **35 (C)**, 189–266, doi: 10.1016/S0422-9894(08)70503-8.

Squire, V. A., 2019: Ocean Wave Interactions with Sea Ice : A 2019 Reappraisal. *Annu. Rev. Fluid Mech.*, 1–25.

Squire, V. A., J. P. Dugan, P. Wadhams, P. J. Rottier, and A. K. Liu, 1995: OF OCEAN WAVES AND SEA ICE. *Annual Review of Fluid Mechanics*, **27**, 115–168, URL www.annualreviews.org.

Sreenivasan, K. R., 1995: On the universality of the Kolmogorov constant. *Physics of Fluids*, **7 (11)**, 2778–2784, doi: https://doi.org/10.1063/1.868656.

Steele, M., J. H. Morison, and N. Untersteiner, 1989: The Partition of Air-Ice-Ocean Momentum Exchange as a Function of Ice Concentration , Floe Size , and Draft. *Journal of Geophysical Research*, **94 (9)**, 12 739–12 750.

Stern, H. L., A. J. Schweiger, J. Zhang, and M. Steele, 2018: On reconciling disparate studies of the sea-ice floe size distribution. *Elementa*, **6**, doi: 10.1525/elementa.304.

Stevens, C. L., N. J. Robinson, M. J. Williams, and T. G. Haskell, 2009: Observations of turbulence beneath sea ice in southern McMurdo Sound, Antarctica. *Ocean Science*, **5 (4)**, 435–445, doi: 10.5194/os-5-435-2009.

Stoney, L., K. J. E. Walsh, S. Thomas, P. Spence, and A. V. Babanin, 2018: Changes in Ocean Heat Content Caused by Wave-Induced Mixing in a High-Resolution Ocean Model. *Journal of Physical Oceanography*, **48 (5)**, 1139–1150, doi: 10.1175/JPO-D-17-0142.1, URL http://journals.ametsoc.org/doi/10.1175/JPO-D-17-0142.1.

Stopa, J. E., F. Ardhuin, and F. Girard-Ardhuin, 2016: Wave climate in the Arctic 1992-2014: Seasonality and trends. *Cryosphere*, **10 (4)**, 1605–1629, doi: 10.5194/tc-10-1605-2016.

Stopa, J. E., P. Sutherland, and F. Ardhuin, 2018: Strong and highly variable push of ocean waves on Southern Ocean sea ice. *Proceedings of the National Academy of Sciences*, **115 (23)**, 5861–5865, doi: 10.1073/pnas.1802011115.

Stroeve, J. C., and D. Notz, 2018: Changing state of Arctic sea ice across all seasons. *Environ. Res. Lett*, **13**, 103 001, doi: 10.1088/1748-9326/aade56, URL https://doi.org/10.1088/1748-9326/aade56.

Stroeve, J. C., M. C. Serreze, M. M. Holland, J. E. Kay, J. Malanik, and A. P. Barrett, 2012: The Arctic's rapidly shrinking sea ice cover: A research synthesis. *Climatic Change*, **110**, 1005–1027, doi: 10.1007/s10584-011-0101-1.

Strong, C., 2012: Atmospheric influence on Arctic marginal ice zone position and width in the Atlantic sector, February-April 1979-2010. *Climate Dynamics*, **39 (12)**, 3091–3102, doi: 10.1007/s00382-012-1356-6.

Strong, C., and I. G. Rigor, 2013: Arctic marginal ice zone trending wider in summer and narrower in winter. *Geophysical Research Letters*, **40 (18)**, 4864–4868, doi: 10.1002/grl.50928.

Sutherland, G., and J. Rabault, 2016: Observations of wave dispersion and attenuation in landfast ice. *Journal of Geophysical Research : Oceans*, **121**, 1–15, doi: 10.1002/2016JC012335.Received.

Sutherland, P., J. Brozena, W. E. Rogers, M. Doble, and P. Wadhams, 2018: Airborne Remote Sensing of Wave Propagation in the Marginal Ice Zone. *Journal of Geophysical Research: Oceans*, **123 (6)**, 4132–4152, doi: 10.1029/2018JC013785.

Sutherland, P., and D. Dumont, 2018: Marginal ice zone thickness and extent due to wave radiation stress. *Journal of Physical Oceanography*, **48 (8)**, 1885–1901, doi: 10.1175/JPO-D-17-0167.1, URL http://journals.ametsoc.org/doi/10.1175/JPO-D-17-0167.1.

Sutherland, P., and J. C. Gascard, 2016: Airborne remote sensing of ocean wave directional wavenumber spectra in the marginal ice zone. *Geophysical Research Letters*, **43**, 5151–5159, doi: 10.1002/2016GL067713.

The WAVEWATCH III® Development Group (WW3DG), 2019: *User manual and system documentation of WAVEWATCH III® version 6.07*. 333, College Park, MD, USA, 465 pp. + Appendices pp., URL https://github.com/NOAA-EMC/WW3/wiki/files/manual.pdf.

Thomson, J., 2012: Wave breaking dissipation observed with "swift" drifters. *Journal of Atmospheric and Oceanic Technology*, **29 (12)**, 1866–1882, doi: 10.1175/JTECH-D-12-00018.1.

Thomson, J., L. Hošeková, M. H. Meylan, A. L. Kohout, and N. Kumar, 2021: Spurious Rollover of Wave Attenuation Rates in Sea Ice Caused by Noise in Field Measurements. *Journal of Geophysical Research: Oceans*, **126 (3)**, 1–16, doi: 10.1029/2020JC016606.

Thomson, J., and Coauthors, 2018: Overview of the Arctic Sea State and Boundary Layer Physics Program. *Journal of Geophysical Research: Oceans*, **123 (12)**, 8674–8687, doi: 10.1002/2018JC013766.

Uzuner, M. S., and J. F. Kennedy, 1976: Theoretical Model of River Ice Jams. *J. Hydraul. Div. Am. Soc. Civ. Eng.*, **102 (9)**, 1365–1383, doi: 10.1061/JYCEAJ.0004618.

Vincent, L., and P. Soille, 1991: Watersheds in Digital Spaces: An Efficient Algorithm Based on Immersion Simulations. *IEEE Transactions on Pattern Analysis and Machine Intelligence*, **13 (6)**, 583–598, doi: 10.1109/34.87344.

Voermans, J. J., A. V. Babanin, J. Thomson, M. M. Smith, and H. H. Shen, 2019: Wave Attenuation by Sea Ice Turbulence. *Geophysical Research Letters*, **46 (12)**, 6796–6803, doi: 10.1029/2019GL082945.

Wadhams, P., 1973: Attenuation of Swell by Sea Ice. *Journal of Geophysical Research*, **78 (18)**, 3552–3563, doi: 10.1029/JC078i018p03552.

Wadhams, P., M. A. Lange, and S. F. Ackley, 1987: The ice thickness distribution across the atlantic sector of the Antarctic ocean in midwinter. *Journal of Geophysical Research: Oceans*, **92 (C13)**, 14 535–14 552, doi: 10.1029/JC092iC13p14535.

Wadhams, P., V. A. Squire, J. A. Ewing, and R. W. Pascal, 1986: The Effect of the Marginal Ice Zone on the Directional Wave Spectrum of the Ocean. *Journal of Physical Oceanography*, **16 (2)**, 358–376, doi: 10.1175/1520-0485(1986)016<0358:TEOTMI>2.0.CO;2, URL http://journals.ametsoc.org/doi/abs/10.1175/1520-0485(1986)016%3C0358:TEOTMI%3E2.0.CO;2.

Wadhams, P., V. A. Squire, J. Goodman, and C. Moore, 1988: The Attenuation Rates of Ocean Waves in the Marginal Ice Zone. *Journal of Geophysical Research*, **93 (C6)**, 6799–6818, doi: 10.1029/JC093iC06p06799.

Weber, J. E., 1987: Wave Attenuation and Wave Drift in the Marginal Ice Zone. *Journal of Physical Oceanography*, **17 (12)**, 2351–2361, doi: 10.1175/1520-0485(1987)017<2351:WAAWDI>2.0.CO;2.

Welch, P. D., 1967: The Use of Fast Fourier Transform for the Estimation of Power Spectra: A Method Based on Time Averaging Over Short, Modified Periodograms. *IEEE transactions on audio and electroacoustics*, **15 (2)**, 70–73.

Wiles, P. J., T. P. Rippeth, J. H. Simpson, and P. J. Hendricks, 2006: A novel technique for measuring the rate of turbulent dissipation in the marine environment. *Geophysical Research Letters*, **33 (21)**, 1–5, doi: 10.1029/2006GL027050.

Williams, T. D., L. G. Bennetts, V. A. Squire, D. Dumont, and L. Bertino, 2013: Wave-ice interactions in the marginal ice zone. Part 1: Theoretical foundations. *Ocean Modelling*, **71**, 81–91, doi: 10.1016/j.ocemod.2013.05.010.

Williams, T. D., P. Rampal, and S. Bouillon, 2017: Wave-ice interactions in the neXtSIM sea-ice model. *Cryosphere*, **11 (5)**, 2117–2135, doi: 10.5194/tc-11-2117-2017.

Zhang, Q., and R. Skjetne, 2015: Image processing for identification of sea-ice floes and the floe size distributions. *IEEE Transactions on Geoscience and Remote Sensing*, **53 (5)**, 2913–2924, doi: 10.1109/TGRS.2014.2366640.

Zhang, Q., and R. Skjetne, 2018: *Sea Ice Image Processing with MATLAB®*. CRC Press, doi: 10.1201/9781351069205, URL https://www.ntnu.edu/imt/books/sea_ice_image_processing_with_matlab.

COLLEGE SCIENCES DOCTORAL DE LA MER BRETAGNE ET DU LITTORAL

Université de Bretagne Occidentale

Titre : Interactions entre turbulence et vagues à l'interface air-mer en présence de glace de mer

Mot clés : Vagues, Zone Marginale de Glace, Turbulence, Interactions Glace-glace

Résumé : La couverture de glace estivale en Arctique a fortement diminué ces dernières décennies, laissant la place au développement de systèmes de vagues de plus en plus énergétiques. Ce constat rend d'autant plus importante la compréhension des interactions entre les vagues et la glace dans la zone marginale de glace (MIZ), pour améliorer notre modélisation du climat terrestre et préparer les futures activités humaine en Arctique. La turbulence générée par les interactions vague-glace est souvent considérée comme la source principale d'atténuation des vagues, et modélisé en utilisant l'hypothèse de viscosité turbulente faute de mesure in-situ.

Ce travail de thèse consiste à analyser des mesures colocalisées de vagues et de turbulence prise dans des MIZs très concentrées en glace de laboratoires naturels de l'estuaire du bas Saint-Laurent. La comparaison entre l'atténuation de l'énergie des vagues, en fonction de leur propagation sous la glace, et la dissipation d'énergie cinétique turbulente montre que dans les conditions rencontrées, la turbulence ne permet pas d'expliquer une fraction significative de l'atténuation des vagues dans la glace. Les interactions entre plaques de glace sont alors quantifiées, et permettent d'expliquer une large partie de l'atténuation des vagues dans la majorité des cas.

Title: Interactions between near-surface turbulence and surface waves in the presence of sea ice

Keywords: Waves, Marginal Ice Zone, Turbulence, Floe-floe Interactions

Abstract: The Arctic summer ice cover has strongly decreased over the past decades, leaving room for more and more energetic wave systems. This makes it all the more important to understand the interactions between waves and ice in the marginal ice zone (MIZ), to improve our modeling of the Earth climate and prepare for future human activity in Arctic. Turbulence generated through wave-ice interactions is often considered to be the main driver for wave attenuation, and is modeled using the eddy viscosity hypothesis due to the lack of in-situ measurements.

This thesis work consists in analysing collocated wave and turbulence measurements taken in the MIZs highly concentrated in ice of natural laboratories of the lower St. Lawrence estuary. Comparing wave energy attenuation and turbulent kinetic energy dissipation shows that, in the conditions encountered, turbulence does not allow to significantly explain wave attenuation in sea ice. Interactions between ice floes are hence quantified, and allow to explain a large part of wave attenuation in most of the cases.